Democratic and Popular Republic of Algeria

Ministry of Higher Education and Scientific Research

University Mohamed Khider of Biskra

Faculty of Exact Sciences and Science of Nature and Life

Department of Material Sciences

Thesis

Presented To Obtain The Degree Of

Doctorate

Option: Renewable Energy And Materials Science.

Presented by:

LATIF Aya

Entitled:

Elaboration of pure and doped ZnO powders with the sol gel method

Publicly defended on: 19/09/2024

In front of the Jury committee composed of:

M^{r} ATTAF Abdallah	Professor	University of Biskra	President
M^{rs} ARABLouiza	MCA	University of Biskra	Supervisor
M^{r} CHALA Abdelouahad	Professor	University of Khenchela	Examiner
M^{rs} HAMZAOUI Majda	MCA	University of Biskra	Examiner

Academic year: 2024-2025

بسم الله الرحمن الرحيم

Dedication

Alhamdulillah, all praise is due to Allah for his blessing given to me during my journey of study.

I have dedicated most of my life to the pursuit of education, and that led to some of my greatest experiences and hardest challenges therefore, I dedicate this achievement to the girl who never gave up and faced all challenges with courage and determination. I believed in myself and my abilities and worked hard to achieve my dreams.

*To the one who have been my source of support and inspiration when my steps faltered, the one who believed in me when I doubted myself, my dear father «**Mahmoud**» and the one who illuminated my path with her light and carried me with her prayers to become what I am today, my dear mother « **Benini Saliha**»*

*To my brothers who have always supported me throughout my years of studies «**Dr. Khaoula, Aicha, and Mohamed El-Baker**»*

*To my soulmates, my supportive friends «**Benini Rayan**, and **Ghodbane Selsabil**»*

*To the angels that adorn my family, my children, and the joy of my heart, «**Brahimi Maria, Brahimi Mira**, **Dendeh Iyad**, **Abdessemed Sirine**, **Benbouta Tasnim**, **Alae Rahmane Hadroug, Harzallah Youcef**»*

*To my second mother « **Professor. Benini Zahira** » and my dear aunt « **Benini Meriem** ».*

*To those who left us early, I dedicate this joy of mine to your pure spirit that accompanied me during this journey, whom i shared with tears and memories. I am proud of what I have become after you. I dedicate, with all love my work, and my joy to you wherever you are… « **Youcef BenBrika** » may Allah bless his soul.*

*To all my family members who supported me and whose prayers were the reason for my success, I would like to especially thank « **Dr. Brahimi Sif Eddin, Latif Ammar, and Benini Hacen**».*

I would like to acknowledge my companions who shared the steps of this journey with me, my colleagues, and PhD students in chemical physics.

Acknowledgments

In the name of Allah, the Most Gracious, the Most Merciful

First and foremost, I would like to express my deepest gratitude to Allah for granting me the strength and guidance to pursue this journey of knowledge.

The success of this work wouldn't have been possible without the combined efforts of many individuals. I take this opportunity to extend my sincere appreciation to everyone who played a role in helping me complete this project.

My heartfelt gratitude goes out to my esteemed supervisor, **Dr. Louiza ARAB**. Her unwavering support and encouragement throughout my research journey were invaluable. Her insightful guidance, constant support, and constructive criticism were instrumental in the completion of this thesis.

I am deeply grateful to the members of my reading committee: Professor **Abdelouahed CHALA** from Khenchela university, Professor **Abdallah ATTAF** from Biskra University, and **Dr. Majda HAMZAOUI** from Biskra University. I deeply appreciate their willingness to dedicate their valuable time to reviewing and evaluating my thesis.

Special thanks go out to Professor **Noureddine SENGOUGA** and Professor **Toufik TIBERMACINE** for their invaluable assistance, particularly during the research phase. I would also like to express my appreciation to everyone working in the Semiconducting and Metallic Materials laboratory at our university.

Finally, I extend my sincere thanks to my family, friends, colleagues, and everyone who supported me in any way during this research endeavor.

Abstract

Undoped, doped, and co-doped zinc oxide powders with different concentrations of bismuth and gallium were prepared by the chemical sol-gel method using zinc acetate, citric acid, bismuth nitrate, and gallium nitrate as precursors and ethylene glycol as a solvent. The effect of doping on zinc oxide powders' structural, morphological, and optical properties was studied. The powders were characterized using various techniques such as X-ray diffraction, scanning electron microscopy, UV-Vis spectroscopy, and Fourier Transform Infrared spectroscopy. the results obtained using the X-ray diffraction technique showed that all the prepared powders have a hexagonal crystalline structure with good crystallinity and nanocrystalline size. A blue shift was observed in the UV-visible spectra of gallium-doped zinc oxide powders compared to those doped with bismuth and co-doped with bismuth and gallium. In addition, the results of UV-visible spectroscopy showed that doping zinc oxide powders with gallium led to a significant increase in the band gap energy while doping with bismuth and co-doping with bismuth and gallium showed a decrease in the band gap energy. Infrared spectral analysis showed a specific association with zinc oxide in all samples. The antibacterial activity of the prepared powders was tested against different types of bacteria. The results showed that pure, doped, and co-doped zinc oxide nanoparticles exhibited strong antibacterial activity against a wide range of bacteria, including Gram-negative Escherichia coli, Klebsiella pneumoniae, and Enterobacter aerogenes, as well as Gram-positive Listeria monocytogenes. These findings demonstrate the remarkable effectiveness of zinc oxide in inhibiting bacterial growth. The prepared samples were subjected to voltage-current testing, and the results showed that the type of doping has a significant impact on the electrical behavior of variable zinc oxide resistance. Doping zinc oxide with bismuth led to a remarkable increase in breakdown voltage, indicating an improvement in resistor lifetime. While doping with gallium led to an increase in current leakage. Dual doping of zinc oxide with bismuth and gallium showed promising results, providing a balance between high breakdown voltage and severe current leakage.

Keywords: ZnO, Sol-Gel, Nanopowder, Bi: ZnO, Ga: ZnO, Antibacterial activity, I-V characteristics.

الملخص

تم تحضير مساحيق اكسيد الزنك الغير مطعم، المطعم، و ذو التطعيم المشترك بتراكيز مختلفة من البيسميث و الغاليوم بواسطة تقنية سائل-هالم الكيميائية باستخدام اسيتات الزنك، حمض السيتريك، نيترات البيسميث و نيترات الغاليوم كمصدر، واالايثيلين غليكول كمذيب، و قد تم دراسة تأثير التطعيم على الخصائص البنيوية، المورفولوجية و الضوئية لمساحيق اكسيد الزنك، تم توصيف المساحيق باستعمال عدة طرق مثل انعراج الاشعة السينية، المجهر االلكتروني الماسح، مطيافية الاشعة الفوق بنفسجية المرئية و الاشعة تحت الحمراء . أظهرت النتائج التي تم الحصول عليها باستعمال تقنية انعراج الاشعة السينية ان كل المساحيق المحضرة ذات بنية بلورية سداسية متراصة ذات تبلور جيد وحجم البلورات نانوي ، سجلنا اصغر بعد بلوري لمساحيق اكسيد الزنك المطعمة بالغاليوم مقارنة بتلك المطعمة بالبيسميث و ثنائية التطعيم، كما أظهرت نتائج مطيافية الاشعة الفوق بنفسجية والمرئية أن تطعيم مساحيق اكسيد الزنك بالغاليوم ساهم بزيادة معتبرة في طاقة عصابة النطاق الممنوع بينما التطعيم بالبيسميث و التطعيم المشترك بكل من البيسميث و الغاليوم أظهرا نقصانا في طاقة عصابة التكافؤ. أظهر التحليل الطيفي لألشعة تحت الحمراء وجود رابطة خاصة بأكسيد الزنك في كل العينات، تم اختبار النشاط المضاد للبكتيريا للمساحيق المحضرة على انواع مختلفة من البكتيريا حيث اظهرت الجسيمات النانوية لاكسيد الزنك الغير مطعمة، المطعمة و مشتركة التطعيم نشاطا مضادا للبكتيريا قويا ضد مجموعة واسعة من البكتيريا بما في ذلك الايشيريكية القولونية ، الكلبسيال الرئوية و امعائية مرياحة ذات الجرام السالب و بكتيريا الليستيريا ذات الجرام الموجب مما يدل على فعالية اكسيد الزنك الملحوظة في تثبيط نمو البكتيريا . تم تعريض العينات المحضرة الختبار جهد-تيار حيث أظهرت النتائج أن نوع التطعيم له تأثير كبير على السلوك الكهربائي لمقاومات أكسيد الزنك المتغيرة. أدى تطعيم أكسيد الزنك بالبيسميث إلى زيادة جهد االنهيار بشكل ملحوظ، مما يشير إلى تحسين في عمر المقاومة. بينما أدى التطعيم بالغاليوم إلى زيادة في التسرب في التيار. أظهر التطعيم الثنائي ألكسيد الزنك بالبيسميث والغاليوم نتائج واعدة، حيث وفر توازنًا بين جهد االنهيار العالي وشدة التيارالمتسرب

الكلمات المفتاحية :أكسيد الزنك (ZnO)، سول -جل مسحو ق نانوي ، ZnO :Bi ،ZnO :Ga ، مضا د للبكتيريا، خاصية I-V

Résumé

Des poudres d'oxyde de zinc non-dopées, dopées, et co-dopées avec différentes concentrations de bismuth et de gallium ont été préparées par la technique sol-gel chimique en utilisant de l'acétate de zinc, de l'acide citrique, du nitrate de bismuth et du nitrate de gallium comme précurseurs et de l'éthylène glycol comme solvant. L'effet du dopage sur les propriétés structurales, morphologiques et optiques des poudres d'oxyde de zinc a été étudié. Les poudres ont été caractérisées par différentes techniques telles que la diffraction des rayons X, la microscopie électronique à balayage, la spectroscopie UV-Vis et la spectroscopie infrarouge à transformée de Fourier. Les résultats obtenus par la technique de diffraction des rayons X ont montré que toutes les poudres préparées ont une structure cristalline hexagonale avec une bonne cristallinité et une taille nanocristalline. Un décalage vers le bleu a été observé dans les spectres UV-visible des poudres d'oxyde de zinc dopées au gallium par rapport à celles dopées au bismuth et co-dopées au bismuth et au gallium. De plus, les résultats de la spectroscopie UV-visible ont montré que le dopage des poudres d'oxyde de zinc au gallium entraînait une augmentation significative de l'énergie de la bande interdite, tandis que le dopage au bismuth et le co-dopage au bismuth et au gallium entraînaient une diminution de l'énergie de la bande interdite. L'analyse spectrale infrarouge a montré une association spécifique avec l'oxyde de zinc dans tous les échantillons. L'activité antibactérienne des poudres préparées a été testée contre différents types de bactéries. Les résultats ont montré que les nanoparticules d'oxyde de zinc non-dopées, dopées et doublement dopées présentaient une forte activité antibactérienne contre un large éventail de bactéries, y compris Escherichia coli, Klebsiella pneumoniae et Enterobacter aerogenes à Gram négatif, ainsi que Listeria monocytogenes à Gram positif. Ces résultats démontrent l'efficacité remarquable de l'oxyde de zinc dans l'inhibition de la croissance bactérienne. Les échantillons préparés ont été soumis à des tests de tension-courant, et les résultats ont montré que le type de dopage a un impact significatif sur le comportement électrique des résistances variables en oxyde de zinc. Le dopage de l'oxyde de zinc avec du bismuth a entraîné une augmentation remarquable de la tension de claquage, indiquant une amélioration de la durée de vie de la résistance. Alors que le dopage avec du gallium a entraîné une augmentation des fuites de courant. Le double dopage de l'oxyde de zinc avec du bismuth et du gallium a montré des résultats prometteurs, Trouver un équilibre entre une tension de claquage élevée et une fuite de courant importante.

Mots-clés : ZnO, Sol-Gel, Nanopoudre, Bi: ZnO, Ga: ZnO, , Activité Antibactérien, I-V caractéristique.

CONTENT TABLE

Chapter I: overview of zinc oxide

Chapter II : Materials and experimental methods

Chapter III: Undoped, doped, and co-doped zinc oxide properties

Part I: Preparation and Analytical Study of Zinc Oxide Powder

Part II: Zinc oxide doped with Bismuth

Part III: Zinc oxide doped with Gallium

Part IV: Bi and Ga co-doping ZnO nanopowders

Chapter IV: Applications of the Zinc oxide elaborated

Part A: Antibacterial activity

Part B: Electrical behaviour

LIST OF FIGURES

LIST Of TABLES

General Introduction

Introduction

Research background

Nanoscience and nanotechnology have garnered a significant attention since its inception in the early of 1990s. During this period, innovative advancements have revolutionized the characterization of materials at the nanoscale and provided a novel understanding of their properties. Subsequent decades witnessed intensive research focused on the physical and chemical properties of nanomaterials, alongside the development of innovative preparation methods. This culminated in the transformation of nanoscience and nanotechnology into the preeminent interdisciplinary frontier.

Research in this field encompasses a broad spectrum of disciplines, including physics, chemistry, materials science, mechanics, microelectronics, biology, and medicine... The recent rapid growth of nanoscience and nanotechnology has significantly impacted socioeconomic development, scientific and technological progress, and even our daily lives [1].

Nanomaterials hold immense promise for a wide range of applications. Among various nanomaterials, zinc oxide (ZnO) stands out as a unique intrinsic semiconductor with a large direct bandgap (3.37 eV) and a high exciton binding energy (60 meV) at room temperature, along with excellent chemical stability [2]. Due to these remarkable properties, ZnO finds applications in ultraviolet (UV) light emission, piezoelectric devices, chemical and gas sensors, transistors, solar cells, catalysts, varistor, and antibacterial...

Doping zinc oxide with suitable elements can improve its structural, optical, and electrical properties, and thus expand its range of applications. Among these elements, Bismuth and gallium are the focus of much new research due to the significant modification they cause in their physical and chemical properties [3, 4].

Scientists have developed numerous methods to create nanoparticles with precise control over their shape, size, and structure. This fine-tuning enhances the properties of these nanomaterials. It's no wonder there are so many techniques for ZnO nanoparticle synthesis. These techniques include ball milling [5], co-precipitation [6], the sol-gel process [7], and hydrothermal synthesis [8]. The chosen method depends on the desired application.

However, each method has its advantages and disadvantages. Notably, some methods require specialized equipment and conditions.

Research aims

The first goal of this research is to attain an optimization of structural, morphological, and optical properties of undoped ZnO, Ga-doped ZnO, Bi-doped ZnO, and co-doped ZnO: Ga, Bi nanopowders, which are elaborated by chemical sol-gel method.

The second goal is to study the effect of the elaborated samples in the biological field as antibacterial behavior, and in the electronic field as varistor devices.

Structure of thesis

This thesis is divided into four chapters organized as follows: In the first chapter, we will provide a bibliographic study of zinc oxide. The second chapter contains different steps of the chemical sol-gel method and states for the synthesis of undoped and (Bi, Ga) doped ZnO nanopowders. It illustrates experimental setups, the characterization method, computational details, and materials used in the experiment.

In Chapter 3, we discuss the different results obtained, which is divided into 4 subchapters: the first subchapter presents the thermal study of the formation of pure zinc oxide and an overview of its structural properties, The second one displays the results and discussions on bismuth-doped zinc oxide. The third subchapter discusses the results of the gallium-doped ZnO, and the last one interprets the results of co-doped zinc oxide: Ga, Bi.

Chapter 4 focuses on translating the scientific results obtained in the previous chapter into practical applications, which enhances the potential for utilizing the improved properties of zinc oxide in various fields. This chapter investigated the antibacterial activity of all previously prepared samples against different types of bacteria. In addition, we evaluate the potential of using these samples in the field of electronics, particularly in the manufacturing of varistors. This was achieved by studying the electrical behavior (current-voltage) of the prepared zinc oxide samples.

The manuscript ends with a general conclusion retracing all the significant results obtained.

References

References

[1] Zhang, Yue. ZnO Nanostructures: Fabrication and Applications. Vol. 43. Royal Society of Chemistry, 2017, doi: 10.1039/9781788010238-fp001

[2] Z.L. Wang, “Nanostructures of zinc oxide,” *Mater. Today 7*, pp. 26–33, 2004.

[3] M. A. Kamran, W. Ali, S. Ullah, T. Alharbi, and Q. Gul, “Facile preparation of Ga-doped ZnO nanostructures by composite-hydroxide-mediated synthesis route for high-performance pseudocapacitors,” *J Energy Storage*, vol. 62, Jun. 2023, doi: 10.1016/j.est.2023.106871.

[4] S. Lavanya, T. R. Kumar, B. Prakash, R. R. Isaac, I. M. Ashraf, M., Shkir, & S. S.Sehgal “Effect of Bi doping on the opto-electronic properties of ZnO nanoparticles for photodetector applications,” *J Photochem Photobiol A Chem*, vol. 446, no. September 2023, p. 115119, 2024, doi: 10.1016/j.jphotochem.2023.115119.

[5] S. Balamurugan, J. Joy, M. A. Godwin, S. Selvamani, and T. S. G. Raja, “ZnO nanoparticles obtained by ball milling technique: Structural, micro-structure, optical and photo-catalytic properties,” in *AIP Conference Proceedings*, American Institute of Physics Inc., May 2016. doi: 10.1063/1.4947775.

[6] S. Mondal, S. A. Ayon, M. S. Islam, M. S. Rana, and M. M. Billah, “Morphological evaluation and boosted photocatalytic activity of N-doped ZnO nanoparticles prepared via Co-precipitation method,” *Heliyon*, vol. 9, no. 10, Oct. 2023, doi: 10.1016/j.heliyon.2023.e20948.

[7] A. Khorsand Zak, J. Esmaeilzadeh, and A. M. Hashim, “X-ray peak broadening and strain-driven preferred orientations of pure and Al-doped ZnO nanoparticles prepared by a green gelatin-based sol-gel method,” *J Mol Struct*, vol. 1303, May 2024, doi: 10.1016/j.molstruc.2024.137537.

[8] S. Alshehri, S. Al-Shehri, H. Ali, A. A. D. Hassaneen, and M. S. Aida, “Properties of calcium doped ZnO nanoparticles prepared by hydrothermal technique,” *Inorg Chem Commun*, vol. 156, Oct. 2023, doi: 10.1016/j.inoche.2023.111201.

Chapter I

overview of zinc oxide

I .1. Introduction

The first chapter provides a comprehensive overview of zinc oxide, specifically emphasizing its current advancements in terms of fundamental aspects such as crystal structure, electronic band structure, electrical, and optical properties. We will also examine the several manifestations of ZnO, followed by an investigation into doping, categorized by type and methods employed. At the end, this chapter examines the various applications of zinc oxide.

Zinc oxide (ZnO) is a long-standing semiconductor that has garnered significant interest since 1935. Recently, the scientific community has regarded ZnO as a 'future material' due to its several intriguing and innovative features that need additional research and development. The material possesses various unique characteristics, such as its ability to function as a semiconductor, piezoelectric substance, luminescent material, and UV absorber. Additionally, zinc oxide exhibits catalytic, ferrite, photoconductive, and photochemical properties. Moreover, as an oxide, it offers several advantages, including non-flammability and non-explosiveness in the event of a fire, as well as being generally inert to the human body.

Figure I. 1: A natural form of Zinc oxide “Zincite”.

The material ZnO is commonly called "Zincite" in its natural state (Figure I.1). However, it may also be artificially produced in a solid form. This broad direct bandgap II-VI semiconductor exhibits color variations based on its impurities and its adherence to stoichiometry.

ZnO has very interesting electromechanical properties, allowing it to be used on a large scale as a transparent semiconductor in acoustic devices and microwave delay lines. Due to its low cost, extensive research has been conducted on ZnO [1].

I.2. General properties of ZnO

I.2.1. Crystallographic properties

Zinc oxide is a semiconductor that belongs to the II-VI group. It crystallizes in a hexagonal wurtzite structure at normal pressure and temperature, as it shown in figure (I.2) and belongs to the space group P63mc. The ZnO molecule has a hexagonal structure resulting from the formation of ionic bonds, and each zinc ion (Zn^{+2}) is surrounded by a tetrahedra composed of oxygen ions (O^{-2}). The tetrahedral coordination represents a covalent bond with sp3 hybridization. The ionic radius of both the anion and the cation influences the stability of the wurtzite structure. This structure is formed when the anions come into contact with the central cation. If the radius of the anion surpasses a certain threshold or if the cation is exceedingly small, the potential energy of the system increases, and it becomes unstable. This occurs because the anions repel each other and are no longer in contact with the central cation [2]. The genesis of this condition arises from the subsequent deliberations over the hexagonal compact (H.C) structure weave:

$$\boldsymbol{R^+ + R^- = \frac{3}{8}c, \qquad c = 2a\sqrt{\frac{2}{3}}}\ , \qquad \textbf{(I.1)}$$

$$\boldsymbol{2R^- \leq a} \qquad \textbf{(I.2)}$$

With.

$$\boldsymbol{\sqrt{\frac{3}{2}} - 1 \leq \frac{R^+}{R^-} \Rightarrow 0.224 \leq \frac{R^+}{R^-}} \qquad \textbf{(I.3)}$$

As the H.C structure derives from the C.F.C structure, we have;

$$\boldsymbol{\sqrt{2} - 1 \geq \frac{R^+}{R^-} \Rightarrow 0.414 \geq \frac{R^+}{R^-}} \qquad \textbf{(I.4)}$$

So the tetrahedral site's stability domain is provided by;

$$\boldsymbol{0.224 \leq \frac{R^+}{R^-} \leq 0.414.} \qquad \textbf{(I.5)}$$

Where R^+ and R^- are the radius of the cation and the anion respectively. According to the bibliography [2], the ionic radius of Zn^{2+} in a tetrahedral site is about 0.60Å, and that of O^{2-} is about 1.38 Å, so the ratio $R_{Zn}/R_o \approx 0.4$ is located in the stability range, hence the stability of the würtzite structure of ZnO. The lattice parameters of Zinc oxide under standard temperature and pressure conditions are (a=b= 0.325 nm; c= 0.521 nm; and the ratio c/a= 1.633) [3].

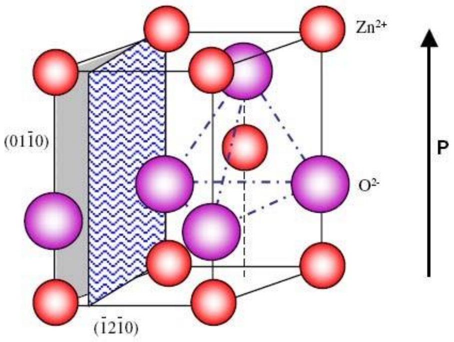

Figure I.2: ZnO's wurtzite crystal structure. One unit cell is outlined (dashed line) for clarity [4].

Table I.1: **Summary of the characteristics of the crystal structure of ZnO [5].**

Lattice		Hexagonal wurtzite
Distance between Zn^{+2} and O^{-2} (The nearest neighbors)		**Along the C axis: d=1.96 Å** **For the other three axes: d=1.98 Å**
Ionic radius for tetrahedral coordination	**Covalent bond**	**Zn neuter=1.31 Å; O neuter = 0.66Å**
	Ionic bond	**Zn^{+2}=0.60 Å; O^{-2}=1.38 Å** **Zn^{+2}=0.70 Å; O^{-2}=1.32 Å (Pauling 1)**
crystal radius for tetrahedral coordination		**Zn^{2+} = 0.074 Å** **O^{2-}=1.24 Å**

Since ZnO's unit cell is completely neutral, the distribution of cations and anions may adopt configurations as identified by crystallography. This allows for the complete termination of some surfaces with cations or anions, producing either positively or negatively charged surfaces. We refer to it as polar surfaces. There are four frequent surfaces in wurtzite ZnO: the non-polar (1120) and (1010) faces, and the polar Zn (0001) and O (0001) terminated faces (Figure I.3).

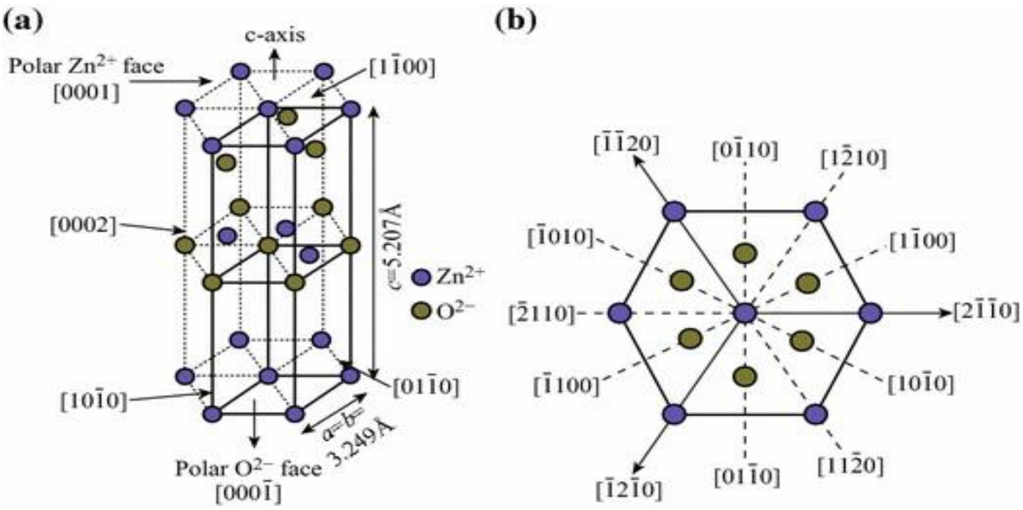

Figure I.3 : Unit cell (a) and crystal atomic plane (b) of ZnO hexagonal wurtzite structure [6].

Zinc oxide can also crystallize in two structures;

- **Rocksalt phase B1**

The Rocksalt or Rochelle salt (NaCl) structure obtained at relatively high pressures metastable phase forming at ~10 GPa and cannot be epitaxially stabilized, the group of space Fm3m [7] (Figure I.4).

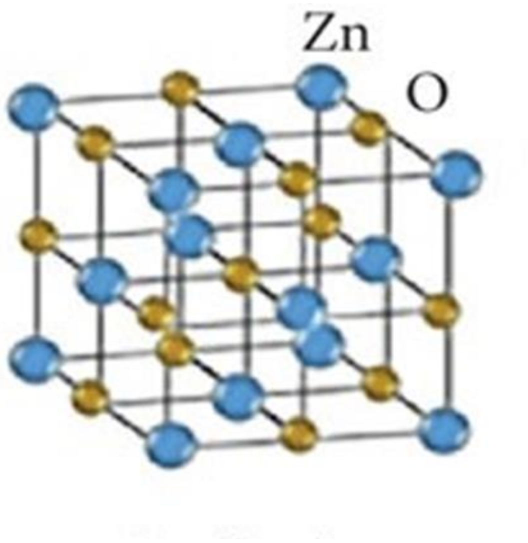

Figure 1.4: The Rocksalt structure of Zinc Oxide [8]

The Bravis lattice is cubic with centered faces, the base comprises a zinc atom and an oxygen atom separated by half a cube diagonal, the atoms having the following position;

$$\textit{Zn:}\ (0, 0, 0);\ (\tfrac{1}{2}, \tfrac{1}{2}, 0);\ (\tfrac{1}{2}, 0, \tfrac{1}{2});\ (0, \tfrac{1}{2}, \tfrac{1}{2})$$

$$\textit{O:}\ (\tfrac{1}{2}, \tfrac{1}{2}, \tfrac{1}{2});\ (0, 0, \tfrac{1}{2});\ (0, \tfrac{1}{2}, 0);\ (\tfrac{1}{2}, 0, 0)$$

- **<u>Zinc blende phase B3</u>**

In thid phase, ZnO has a cubic structure and can be seen as two CFC structures offset from each other by a quarter of the cube diagonal. This structure is obtained by placing the Zn atoms on one of the CFC and O atoms on the other one [9]. The coordination of the atoms are:

$$\textbf{Zn:}\ (0, 0, 0);\ (\tfrac{1}{2}, \tfrac{1}{2}, 0);\ (\tfrac{1}{2}, 0, \tfrac{1}{2});\ (0, \tfrac{1}{2}, \tfrac{1}{2})$$

$$\textbf{O:}\ (\tfrac{1}{4}, \tfrac{1}{4}, \tfrac{1}{4});\ (\tfrac{1}{4}, \tfrac{3}{4}, \tfrac{3}{4});\ (\tfrac{3}{4}, \tfrac{1}{4}, \tfrac{3}{4});\ (\tfrac{3}{4}, \tfrac{3}{4}, \tfrac{1}{4})$$

The bravais lattice is face-centred cubic (cfc) with four ZnO molecules per conventional lattice [10]. As shown in figure I.5.

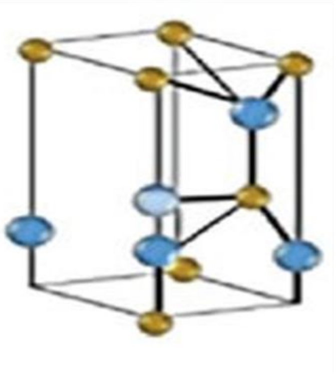

Figure I.5 : The zincblende structure of Zinc oxide, the shaded orange and blue spheres denote Zn and O atoms, respectively [8].

I.1.2 Electrical properties

- **Electrical band**

Semiconductor science gives wide attention to the band structures, which are important elements in characterizing the potential use of the material, such as defining the width band gap and deciding the proper type of dopant. Zinc oxide is a semiconductor with a direct band gap (Eg= 3.37eV at room temperature), i.e. its conduction band maximum and its valance band minimum at the Γ point at the Brillouin zone as shown in figure 1.6.a. The minimum of the conduction band is formed by the empty 4 s states of the Zn^{2+} or the antibonding sp3 hybrid states. The maximum of the valence band is originated from the occupied 2p orbitals of the O^{2-} or from the bonding sp3 orbitals [11, 12].

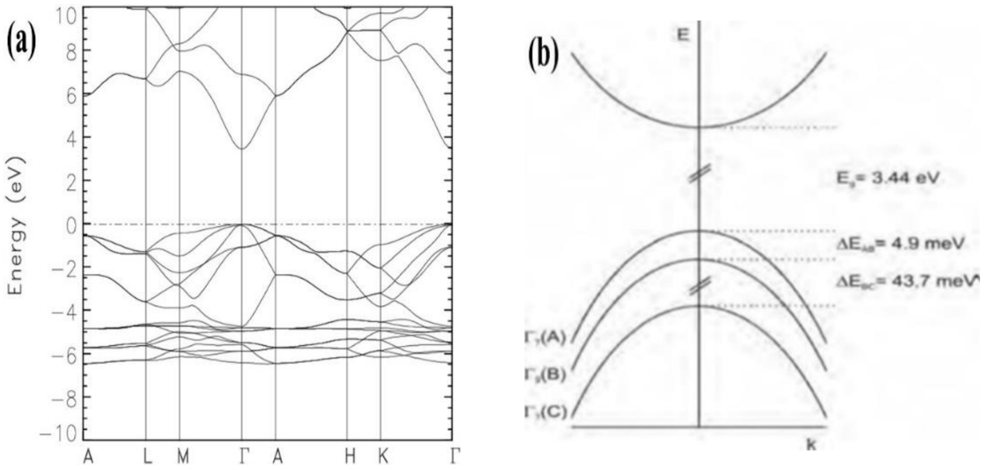

Figure I.6 : (a); Band structure of Zinc oxide[13], (b); Schematic band gap of ZnO at the point considering the crystal-field and spin-orbit splitting of the valence band [14].

The ZnO valance band has been experimentally divided into three band states A, B, and C by spin-orbit and crystal-field splitting. This splitting is schematically represented in (Figure I.6. b). The A and C sub-bands are known to possess Γ7 symmetry, whilst the middle band, B, has Γ9 symmetry [15].

Electrically, Zinc oxide is a group $A^{II}B^{VI}$ semiconductor with a band gap of about 3.3 eV, which allows it to be classified as a wide band gap semiconductor [16]. This band gap value can vary depending on the preparation method and the doping level, between 3.30 eV and 3.39 eV [17, 18].

A high conductivity (> 5.103 Ω^{-1}.cm^{-1}) is possible in n-type ZnO, due to intrinsic defects, dopants (Al, In, Ga, B, F), or in combination [19]. It is reported that the electrons mobility, in ZnO thin films, is typically in the range of 20 to 30 cm^2/V.s. Additionally, the greatest mobility found in ZnO single crystals is in the order of 200 cm^2/V.s. [20].

Table I. 2: Summary of the electrical characteristics of the of ZnO semiconductor [21].

Properties	**Characteristic**
Electron concentration	**10^{20} electron.cm^{-3}**
Holes concentration	**10^{19} cm^{-3}**
Exciton binding	**60 meV**
Electron effective masse	**0.24 m_0, m_0=9.11×10^{-31} kg**
Hole effective masse	**0.59 m_0, m0=9.11×10^{-31} kg**
The molibility of n type	**200 cm^2 v^{-1} s^{-1}.**
The molibility of p type	**5-50cm^2 v^{-1} s^{-1}.**
Static dielectric constant (εs)	**7.9**
Point of zero charge (Pzc)	**8–9 Ph**

I.2.3. Piezoelectric properties

Among the semiconductors crystallizing in a tetrahedral lattice, ZnO exhibits the strongest piezoelectric coefficients, with greater electromechanical coupling than that of other semiconductors [23].

This makes it technically an interesting material, for example for the production of piezo transducers. In a piezoelectric crystal, the electrical polarization is generated by the presence of stresses. Due to the symmetry of ZnO in the wurtzite phase, the stress torsor has only three independent components (e_{31}, e_{33}, and e_{15}), which allows the piezoelectric torsor to be described in terms of the stress tors as follows:

$$\begin{pmatrix} \mathbf{P_{xx}} \\ \mathbf{P_{yy}} \\ \mathbf{P_{zz}} \end{pmatrix} = \begin{pmatrix} \mathbf{0} & \mathbf{0} & \mathbf{0} & \mathbf{0} & \mathbf{e_{15}} & \mathbf{0} \\ \mathbf{0} & \mathbf{0} & \mathbf{0} & \mathbf{e_{15}} & \mathbf{0} & \mathbf{0} \\ \mathbf{e_{31}} & \mathbf{e_{31}} & \mathbf{e_{33}} & \mathbf{0} & \mathbf{0} & \mathbf{0} \end{pmatrix} \begin{pmatrix} \boldsymbol{\varepsilon_{xx}} \\ \boldsymbol{\varepsilon_{yy}} \\ \boldsymbol{\varepsilon_{zz}} \\ \boldsymbol{\varepsilon_{xy}} \\ \boldsymbol{\varepsilon_{yz}} \\ \boldsymbol{\varepsilon_{zx}} \end{pmatrix} \quad \textbf{(I.6)}$$

with Pii being the piezoelectric torsor and εij the stress torsor. Stress along the c-axis or perpendicular to this axis results in a resulting piezoelectric field oriented along the c-axis as well [24] :

$$\mathbf{P_z = e_{33}}\boldsymbol{\varepsilon}_\mathbf{z} + \mathbf{e_{31}}\boldsymbol{\varepsilon}_\perp \quad \textbf{(I.7)}$$

The term in e15 corresponds to torsional stresses which are generally neglected. It is therefore expected that a non-polar (i.e. not c-axis oriented) ZnO sample does not exhibit piezoelectricity (which is an advantage for the realization of heterostructures). Due to the low symmetry of the wurtzite structure of ZnO, a spontaneous polarisation field is also expected to be c-axis oriented, although it has never been directly measured [25].

I.2.4. Optical properties

The optical properties of ZnO have been studied by different experimental techniques such as optical absorption, reflection, transmission, photoluminescence, etc.

I.2.4.a. Optical absorption

The absorption coefficient and refractive index of ZnO depend on the quality of the material. Due to its large gap, this material can pass up to 80% of visible light when it is of good crystal quality. This makes it a transparent material in the visible range with a refractive index of 2 for a bulk sample [26]. Its absorption coefficient is quite large (2.5×10^5 cm^{-1}) from 3.3 eV (near the gap) and it is almost zero ($< 10^3$ cm^{-1}) for low energies [27]. Thus, doped ZnO belongs to the family of transparent conductive oxides (TCO).

I.2.4.b. Photoluminescence

The photoluminescence (PL) bands can be observed for ZnO between the near UV and Visible range, figure I. 7 shows the typical PL spectrum of a single crystal ZnO obtained at 4.2 K [16]. The high energy (UV) part, also called 'band edge', concerns the excitons, while the low energy (visible) region, called the 'green band', corresponds to defects linked to deep level emissions from deep levels such as zinc interstitials, oxygen vacancies, etc [28, 29]. The visible region can also include bands emitting in the blue [30], yellow [31], and red [32].

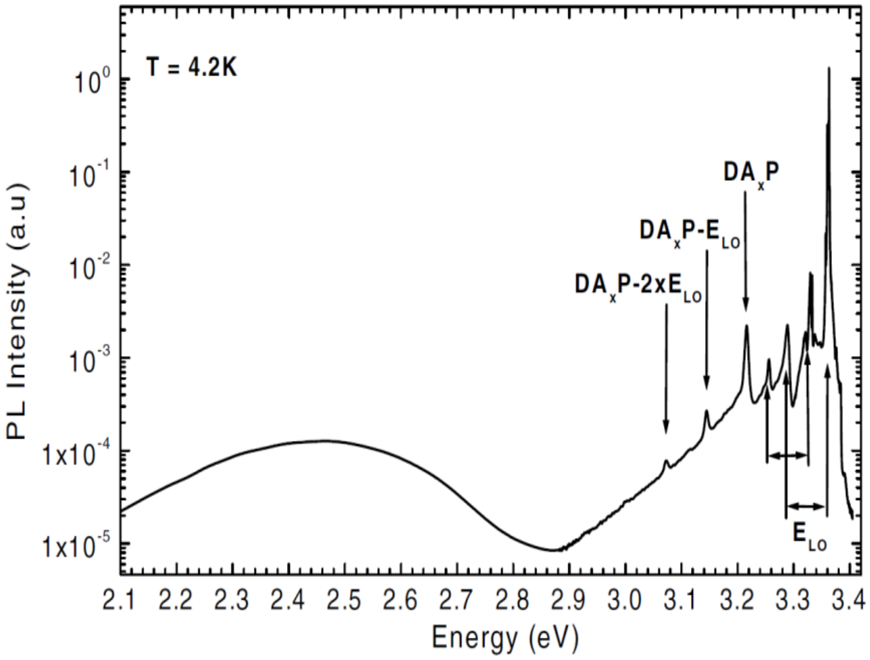

Figure I. 7 : Photoluminescence spectrum of a ZnO layer [15].

The region of the PL spectra between 2.9 and 3.45 eV corresponds to the band edge luminescence is found. It is primarily split into two sections: a high energy initial section and a low energy second section The first part is related to the intrinsic emission of the material. It is associated with the recombination of electrons from the conduction band with the holes of the valence band and includes most of the excitonic transitions, free and bound. The second part of the band edge, with lower energy, represents the emission of extrinsic recombination. This emission is associated with defects or impurities in the material and also contains the phonon replicas of excitonic transitions [33].

I.2.5. Chemical and catalytic properties

The pure Zinc oxide is white powder, it has crystalline thermochromic property which causes it to transition from white to yellow when heated in air and returing to white when cooles. This shift in color is brought on by oxygen loss at high temperatures [34].

In terms of chemistry, Zinc is a very reducing element that reacts with oxygen and other non-metals to form new materials. When it interacts with acid, hydrogen is liberated. Zinc can react with environmental elements such as moisture, oxygen, carbon dioxide, etc. For instance, when exposed to air, it develops a thin layer of impermeable oxide known as white rust on the surface. On the other hand, ZnO is an amphoteric oxide, meaning it is soluble in both acidic (in the form of Zn^{2+} anions) and basic (in the form of Zincate $Zn\ (OH)^{2-}$ anions) solutions. As a result, it dissolves just minimally in clean water, not at all in alcohol, but extremely well in the majority of acids and alkalis [35].

The chemical creation and surface characteristics of a materials determine its capasity to be as a catalyst in particular system, the effectiveness of Zinc oxide depends on the way it is prepared. It is caused mainly by the crystal lattice's degree of profection and the semiconducting qualities of Zinc oxide. As well as semiconducting properties (vacancies, atom in interstitial positions, ect.) [36].

Zinc oxide has extremely promising catalytic characteristics since the redox process is effective. The powders floating in water play an important function as photochemical catalysts for the oxidation of phenols, the degradation of organic pollutants (pesticides, dyes, etc.), the oxidation of ammonia to nitrate, and the oxidation of oxygen to ozone [37].

There are various uses for zinc oxide in the fields of photonics and optoelectronics due to its physical characteristics.We also reference the work of N. Boulares, who demonstrated that ZnO was more efficient than TiO_2 at removing the pollutant from water: $C_9H_{11}N_2O_2Cl$, monolinuron N [37].

I.2.6. The antibacterial properties

Given thier unique physical and chemical properties, Zinc oxide nanoparticles (ZnO NPs) have been studied for their antibacterial effect, its nanoparticles have a high surface area to volume ratio and demonstrate a variety of processes that might nigatively impact bacterial servival.

The nanoparticles of zinc oxide rely on an important method of concentration and particle length in interacting with the bacterial cell membrane, leading to structural damage that results in leakage of cellular contents [38].

Furthermore, ZnO nanoparticles have been shown to be efficient bactericidal agents by inhibiting the growth of methicillin-sensitive strains of S. aureus (MSSA), methicillin-resistant strains of S. aureus (MRSA), and methicillin-resistant strains of S. epidermidis (MRSE) [39, 40]. Zinc oxide (ZnO) NPs are highly inexpensive[41] and effective against a variety of bacteria because of their size dependence [42]. These include pathogens that exhibit modest toxicity to human cells, such as Klebsiella (a pneumonia agent) [43], Salmonella enteritidis[44], Listeria monocytogenes [45], Streptococcus mutans, Lactobacillus[46], and E. coli [47]. They are appropriate for use as coating materials for medical devices and other products in the textile [48] and glass [49] sectors due to their white colour, capacity to block UV radiation, and resistance to biofilm development. Furthermore, approval for zinc therapy has been granted by the food and drug administration (FDA). and nowadays, Zn is available as a food additive [50]. The activity of metallic nanoparticles as antibacterial agents is significantly influenced by their generation of reactive oxygen species (ROS) when ZnO NPs are exposed to light or oxygen, they can produce reactive oxygen species (ROS) such as superoxide radicals, hydrogen peroxide, and hydroxyl radicals. Bacterial cell death can result from oxidative stress caused by ROS, which damages proteins, DNA, and cell membranes [51] (Figure I.8). Zinc oxide particles can influence the activity of bacteria by releasing zinc ions (Zn^{+2}), especially when exposed to moisture or in a biological environment. These ions are recognised for their antibacterial efficiency, since they disrupt bacterial cell processes and impede enzymatic activity, preventing bacterial survival and growth [52].

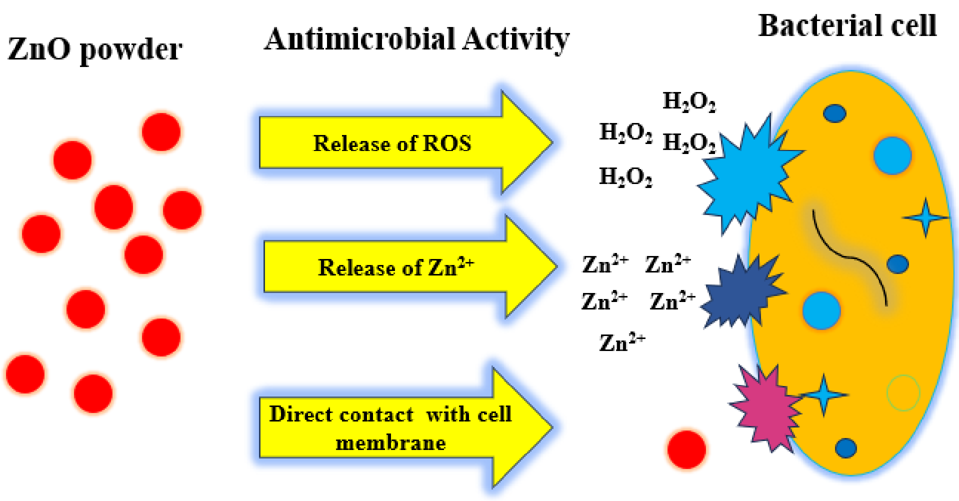

Figure I.8 : Hypothesised mechanisms of action of nanoparticles [53].

I.3. Defects in ZnO

ZnO has a relatively complex structure because of the presence of structural flaws, despite its simple chemical synthesis. These point defects can be observed as deviations in the arrangement of zinc and oxygen atoms (Figure I.9). The most frequently mentioned flaws in the material are zinc vacancies, referred to as V_{Zn} in the Kröger and Vink notation, which are zinc atoms missing from the lattice. Additionally, there are oxygen vacancies (V_O), zinc and oxygen atoms located in interstitial positions, meaning they occupy empty tetrahedral or octahedral sites in the ZnO structure, denoted as Zn_i and O_i respectively. Furthermore, there are cases where oxygen atoms occupy zinc positions (O_{Zn}). Additionally, the inadvertent incorporation of hydrogen atoms into interstitial sites, referred to as Hi in the ZnO structure, is recognized as an unintentional extrinsic dopant [54].

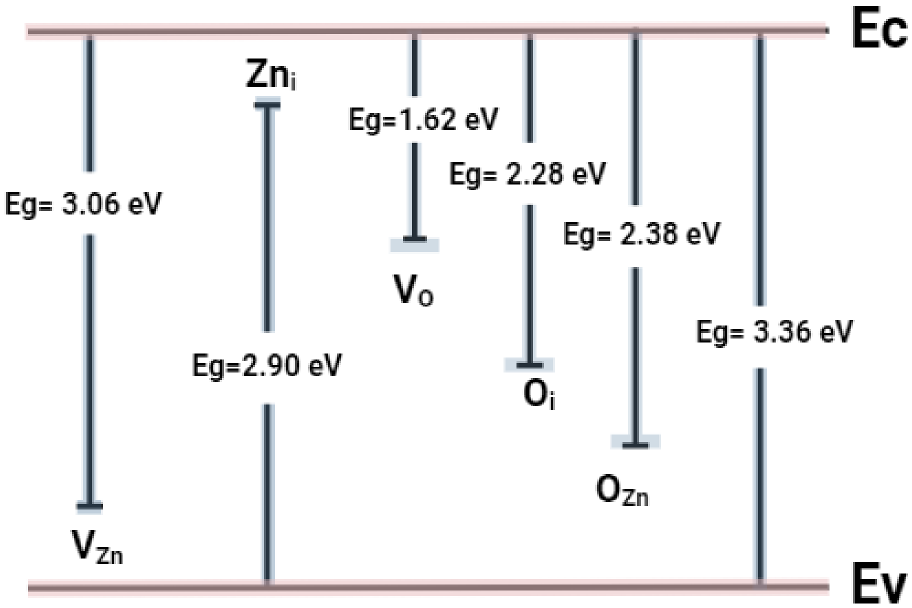

Figure I.9: Location of the main defects intrinsic in the band gap of ZnO [54]**.**

I.4. Doping of ZnO

ZnO doping is required for its use in optoelectronic devices like as displays, gas detectors, and photovoltaic solar cells. Doping can be used to achieve electrical qualities (n-type or p-type), well-defined optical properties (doping with rare earth elements such as Yb, Tm, Nd, and so on), or magnetic properties.

Intentional doping can be obtained using two different techniques: 'in-situ' doping and 'ex-situ' doping. The 'in-situ' method consists of introducing the doping element into the matrix during the growth of the material. In the 'ex-situ' method, the doping impurity is introduced after the material has been made, using either ion implantation or thermal diffusion.

ZnO with a wurtzite structure is usually an n-type semiconductor, due to the obvious presence of intrinsic defects such as O vacancies (V_O) and Zn interstitials (Zn_i). With electron densities as high as 10^{21} cm^{-3}, a value that fortunately has been reduced by molecular beam epitaxy (MBE) to about 10^{17} cm^{-3} and by hydrothermal growth to below 10^{14} cm^{-3} [55, 56].

To underline, intentionally n-type ZnO doping is quite simple at attainment compared to p-type doping. As n-type dopants, group III elements B [57], Al [58- 62], Ga [63], and In [64], rare earth metals (group IIIB) Sc and Y [65], group IV elements Si [66], Ge [67] and Sn [68], and group VII elements F [69], Cl [70].

Zinc oxide is usually doped with group III elements, which have an ionic radius similar to Zn^{2+} ions (0.074 nm) [71, 72].The ionic radius of aluminium (Al^{3+}), indium (In^{3+}) and gallium (Ga^{3+}) ions are 0.054, 0.080 and 0.062 nm respectively. These elements act as shallow donors substituting some part of the zinc side giving carrier concentrations higher than 10^{20} cm^{-3}. Doping ZnO semiconductor with bismuth (Bi) leads to high Seebeck Coefficient of ~500µV/k and a decrease in the electrical conductivity was reported due to the segregation of Bi ions at the grain boundaries; When n-type ZnO grains (ρ=0.1-10 Ω.cm) are separated by a p-type intergranular phase ($\rho=10^{10}-10^{12}$.cm) [73, 74], a double n/p/n Schottky barrier forms [75].

The doping materials, such as (Bi, Ga, Al, ect), exhibit distinct characteristics in the microstructure of Zinc oxide, particularly in the growth of the grains, which in turn alters the sizes of ZnO particles. Additionally, the size of ZnO particles significantly influences the effectiveness of their antibacterial activity, as smaller particle sizes result in greater penetration efficiency into the bacterial membrane.

I.5. Different forms of ZnO

Zinc oxide is the only oxide that possesses a wide range of shapes at the macro, micro, and nanoscales. It comes in a variety of shapes, including bulk, thin films, nanowires, nanocolumns, nanoflowers, tripod nano springs, and nano arcs.

The various structures of zinc oxide at nanometer scales are used in various nanotechnology fields. ZnO is found in structures that are one-dimensional (1D), two-dimensional (2D), and three-dimensional (3D). In this regard, the 1D structures, such as wires and combs, needles, springs, and rings, as well as nanorods, tubes, belts, helixes, and ribbons [76-82]make up the biggest category. In addition, ZnO produced in 2D forms includes nanoplate/nanosheet and nanopellets [83]. On the other side, 3D ZnO structures include dandelion, flower, snowflake, and coniferous urchin-like formations [84] (Figure I. 10).

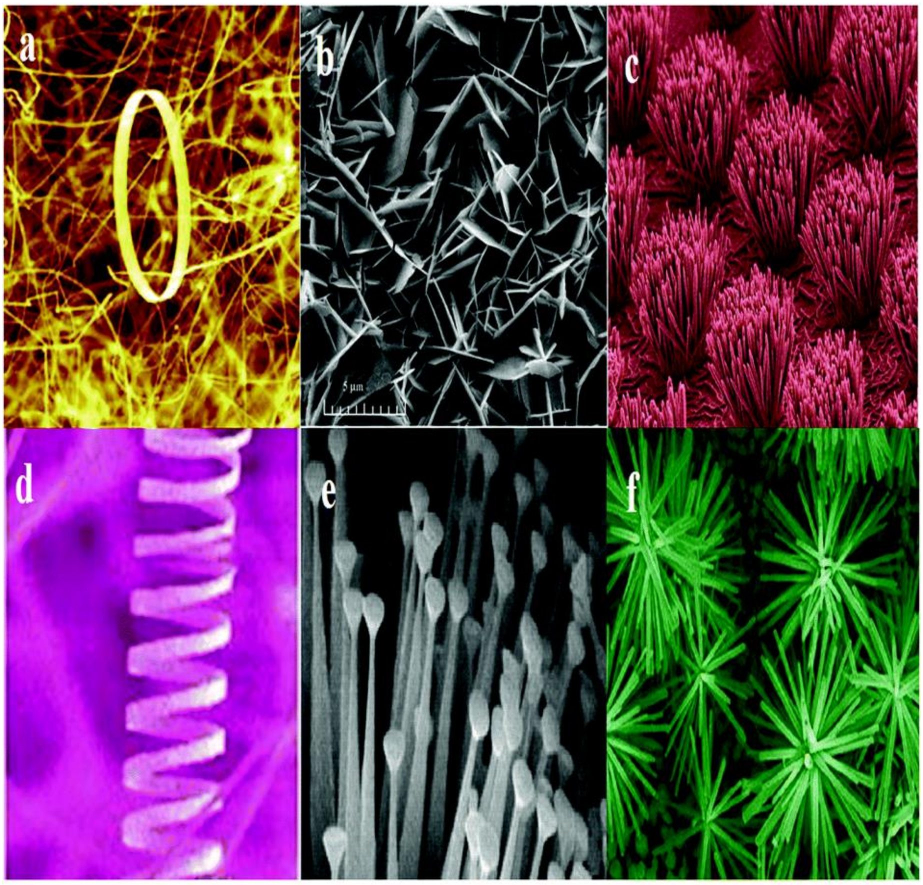

Figure I. 10: Different forms of ZnO nanostructures [85].

I.6. Application of zinc oxide

Zinc oxide's exceptional physical qualities make it suitable for use in a broad range of applications, including electronics, optics, mechanics, cosmetics (sunscreen), and so on.

I.6.1. Thin films

Zinc oxide (ZnO) thin films have a wide range of applications in various fields such as electronics, optics, energy, and biomedicine. We can name some of its most important and recent applications:

Photovoltaic cells: ZnO thin films are used as a window layer in solar cells, providing high transparency and excellent electrical conductivity [86]. The photovoltaic effect describes how some materials may catch photon energy and excite an electron from the valence band to the conduction band, resulting in a hole. To prevent recombination of the "electron-hole" pair, a device made up of two semiconductors is required—one of type n charged with electrons and the other of type p with an excess of positive holes (Figure I.11). The junction between these p-n semiconductors will create an electric field in the depletion zone, with the goal of moving negative charges to n side and positive charges to the p one, therefore minimizing electron-hole pair recombination [87].

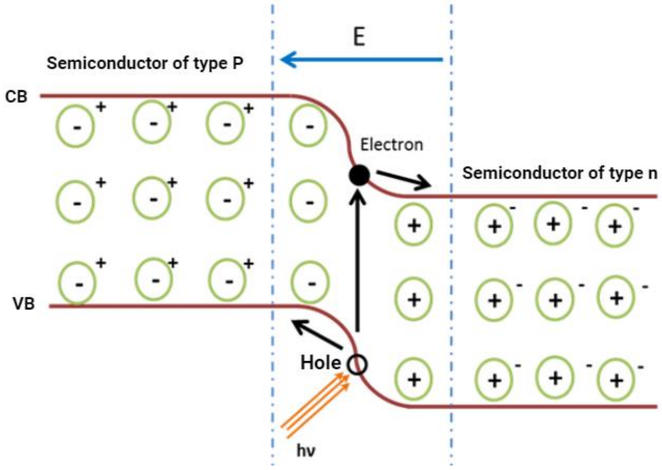

Figure I. 11: Principle of operation of a photovoltaic cell with a pn heterojunction [87].

<u>Gas sensors</u>: ZnO semiconductors exhibit typical n-type properties due to oxygen vacancies or zinc interstitials serving as native donors. Excess zinc causes the creation of non-stoichiometric $Zn_{1+\delta}O$ compounds, resulting in structural disarray. ZnO nanostructures have excellent gas sensing characteristics because to their oxygen-deficient surface, which quickly oxidises in the environment at high temperatures to attain ZnO surface stoichiometry (Figure I. 12). The chemisorption and dissociation of oxygen on defect sites make ZnO very sensitive to metal oxide semiconductor (MOS) gaseous target chemicals. Along with good gas sensing characteristics, the paragraph emphasizes the appeal of ZnO nanostructures due to the variety of possible fabrication procedures [88].

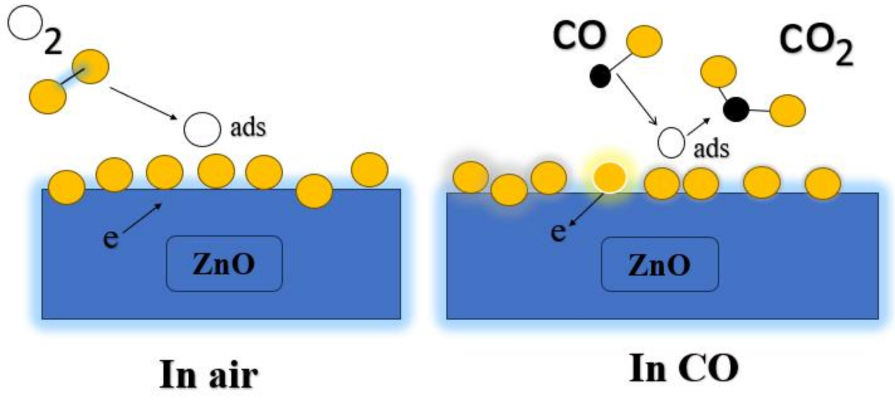

Figure I. 12: CO sensing mechanism of ZnO gas sensor [89].

I.6.2. Zinc oxide powder

Because of its various chemical and physical characteristics, zinc oxide has undergone significant evolution to meet new uses. Zinc oxide has traditionally been employed as a white pigment and a key component in rubber manufacture, but its uses have grown dramatically due to new innovations, particularly in the production of agricultural, medicinal, and ceramic products. In addition, Zinc oxide's antibacterial qualities have also contributed to its selection as the preferred material for the intended uses.

<u>Zinc Oxide varistor</u>: zinc oxide varistor is a type of electrical component that is used to protect electronic devices from transient voltage spikes and surges (Figure I .13). It is a type of metal oxide varistor (MOV) which is made up of a ceramic material that contains zinc oxide and other metal oxides. The varistor works by providing a low resistance path for excess voltage to flow to ground when a voltage surge or spike occurs. When the voltage across the varistor exceeds its breakdown voltage, the varistor conducts current and limits the voltage to a safe level, protecting the electronic device connected to it. Zinc oxide varistors are commonly used in power supplies, surge protectors, and other electronic devices that require protection from voltage surges and transients. They are typically available in a variety of sizes and voltage ratings to suit different applications [90].

Figure I. 13 : Different shapes and sizes of ZnO varistors for the protection of electrical equipment operate at voltages [91].

Varistor are created by forming and sintering ceramic components made of Zinc oxide. Then, either thick film silver arc or metal sprayed into flames is used to electrode these components. According to the following schema (Figure I. 14). ZnO grains with an average grain size make up the majority of the varistor between contacts [91].

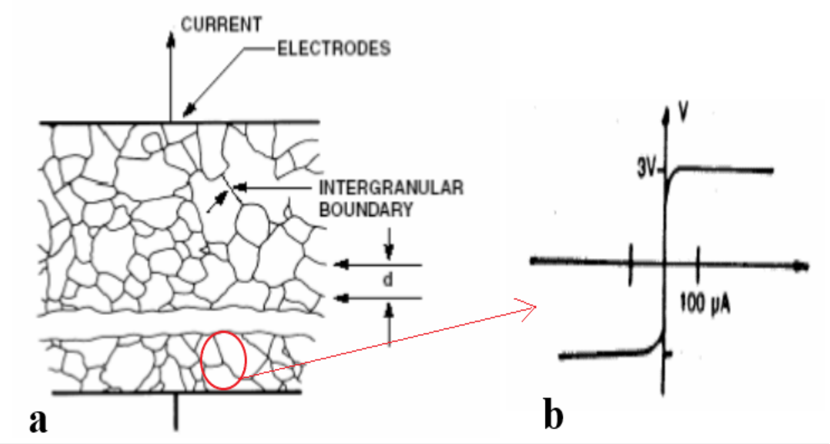

Figure I. 14 : (a) Shematic of a metal oxide varistor's microstructure, , (b) ZnO Grain I-V characteristic [91].

Varistors have three distinct regions of operation. At low voltages, the insulating barriers between the grains result in a very high and almost Ohmic resistivity, which is called the pre-breakdown or Ohmic region. At a certain voltage, called the threshold or breakdown voltage, the system enters the breakdown region in which the empirical relation describes the current increases abruptly, and the dependence of current on voltage:

$$I = KV^{\alpha} \tag{I.8}$$

The use of log-log scales on the graph of figure I.15 allows showing the wide range of voltage-current curve.

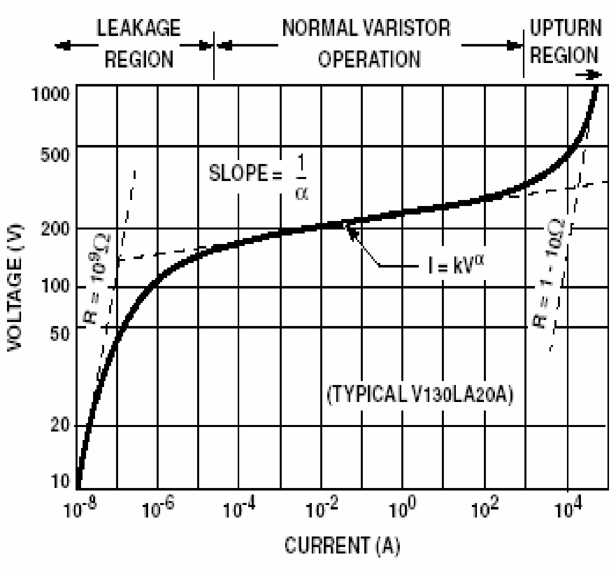

Figure I. 15 : Typical Varistor V-I Curve Plotted on Log-Log Scale [92].

Ebrahimizadeh et al. [93], report that pure ZnO can exhibit non-linear behavior. This phenomenon is explained by the nanometric size of the powder used: more reactive, the ceramic is more oxidized at the grain boundaries and the excess oxygen causes the formation of a potential barrier. The effect of additives on the properties of zinc oxide varistors can be significant. One of the most important additives used in the manufacture of zinc oxide varistors is bismuth oxide (Bi_2O_3). Garino and Rodriguez suggest that the main role of: Bi_2O_3 would thus contribute to the formation of potential barriers. It presents several crystalline phases [94]. as well as metastable phases, among which:

- The α phase, monoclinic, is stable up to 720 °C.

- The δ phase, cubic, is stable between 720 °C and melts at 825 °C.

- The β-phase, quadratic and metastable, results from cooling of the δ-phase or from quenching from the liquid state. The existence of under-oxygenated β phases has also been reported.

- The γ phase, cubic centered and metastable, is formed by quenching of the δ phase.

Carlson and Gupta [95] found that small addition of Ga caused a delay in the onset of the upturn region. However, at higher levels of Ga, the upturn region occurs at lower current density, and only small amount of Ga are required to generate high nonlinear coefficients α.

Substitution of Ga^{3+} ions into zinc lattice sites results in an increase in carrier concentration. This increases the leakage current by decreasing the resistivity of the grain boundary. The donor effect on the high current resistivity in the upturn region has been widely investigated, and it has been shown that the donor ions such as Al^{3+}, Ga^{3+}, and In^{3+} can indeed delay the onset of voltage upturn to higher current density [96].

References

References

[1] C. Jagadish, & S. J. Pearton, (Eds.), “Zinc oxide bulk, thin films and nanostructures: processing, properties, and applications.” Elsevier. (2011).

[2] R. D. Shannon and C. T. Prewitt, “Effective ionic radii in oxides and fluorides,” Acta Crystallogr B, vol. 25, no. 5, pp. 925–946, 1969, doi: 10.1107/s0567740869003220.

[3] W.B. Pearson, “Landolt-Börnstein numerical data and functional relationships in science and technology. Group 3, Crystal and solid state physics. Vol. 17, Semiconductors, New series. Berlin SE ” - 642 pages ; Springer Berlin, 1982.

[4] F. F. Vidor, G. I. Wirth, and U. Hilleringmann, “ZnO thin-film transistors for cost-efficient flexible electronics”. 2017. doi: 10.1007/978-3-319-72556-7.

[5] Z. Sofiani, “Contributions à l'étude des propriétés optiques non linéaires de nanoparticules en couches minces à base de ZnO”. Diss. Université d'Angers, 2007.

[6] Wahl, Ulrich, et al. “Arsenic in ZnO and GaN: Substitutional cation or anion sites.” MRS Online Proceedings Library (OPL) 994 (2007): 0994-F01.

[7] K. Dakhsi, B. Hartiti, S. Elfarrass, H. Tchognia, M. E. Touhami, and P. Thevenin, “Étude des propriétés structurales, optiques et électriques des couches minces de ZnO dopées Al déposées par Spray Pyrolysis,” Afrique Science: Revue Internationale des Sciences et Technologie 10.3, 2014.

[8] R. Kumar, O. Al-Dossary, G. Kumar, and A. Umar, “Zinc oxide nanostructures for no2 gas–sensor applications: A review,” Nanomicro Lett, vol. 7, no. 2, pp. 97–120, 2015, doi: 10.1007/s40820-014-0023-3.

[9] R. Kumar, G. Kumar, O. Al-Dossary, & A. Umar, ZnO nanostructured thin films: Depositions, properties and applications—A review. Materials Express, 5(1), 3-23, 2015. doi:10.1166/mex.2015.1204

[10] M. H. Sosa Lissarrague, S. Alshehri, A. Alsalhi, V. L. Lassalle, and I. López Corral, “Heavy Metal Removal from Aqueous Effluents by TiO_2 and ZnO Nanomaterials,” Adsorption Science and Technology, vol. 2023. Hindawi Limited, 2023. doi: 10.1155/2023/2728305.

[11] J. P. Perdew, J.A. Chevary, S. H. Vosko, K. A. Jackson, M. R. Pederson, D. J. Singh, & C. Fiolhais, "Atoms, molecules, solids, and surfaces: Applications of the generalized gradient approximation for exchange and correlation," Physical review B, 46(11), 6671. (1992).

[12] C. F. Klingshirn, A. Waag, A.Hoffmann, & J. Geurts, "Zinc oxide: from fundamental properties towards novel applications". (2010).

[13] F. F. Vidor, G. I. Wirth, and U. Hilleringmann, "ZnO thin-film transistors for cost-efficient flexible electronics". 2017. doi: 10.1007/978-3-319-72556-7.

[14] C. Ekuma, D. Bagayoko, G. L. Zhao, L. Franklin, & J. T. Wang, "First Principle Study of Electronic Structures of w-CdS, zb-CdS, w-ZnO and Ferro-NaNO2". African J. Phys., 3, 119-130. (2010).

[15] C. F. Klingshirn, "ZnO: Material, physics and applications," ChemPhysChem, vol. 8, no. 6, pp. 782–803, 2007, doi: 10.1002/cphc.200700002.

[16] B. K. Meyer, H. Alves, D. M. Hofmann, W. Kriegseis, D. Forster, F. Bertram, & A. V. Rodina, "Bound exciton and donor-acceptor pair recombinations in ZnO," Phys Status Solidi B Basic Res, vol. 241, no. 2, pp. 231–260, 2004, doi: 10.1002/pssb.200301962.

[17] V. Srikant and D. R. Clarke, "On the optical band gap of zinc oxide," J Appl Phys, vol. 83, no. 10, pp. 5447–5451, 1998, doi: 10.1063/1.367375.

[18] L. S. Alqarni, A. M. Alghamdi, N. Y. Elamin, and A. Rajeh, "Enhancing the optical, electrical, dielectric properties and antimicrobial activity of chitosan/gelatin incorporated with Co-doped ZnO nanoparticles: Nanocomposites for use in energy storage and food packaging," J Mol Struct, vol. 1297, Feb. 2024, doi: 10.1016/j.molstruc.2023.137011.

[19] A. Amri, L. Arab, A. Meftah, and A. Latif, "Effect of aluminum doping on the structural, optical and electrical properties of ZnO thin films processed under thermal shock conditions," Results in Optics, vol. 11, May 2023, doi: 10.1016/j.rio.2023.100426.

[20] K. L. Chopra, S. Major, and D. K. Pandya, “Transparent conductors-A status review,” Thin Solid Films, vol. 102, no. 1, pp. 1–46, 1983, doi: 10.1016/0040-6090(83)90256-0.

[21] T. Aoki, Y. Shimizu, A. Miyake, A. Nakamura, Y. Nakanishi, and Y. Hatanaka, “p-type ZnO layer formation by excimer laser doping,” Phys Status Solidi B Basic Res, vol. 229, no. 2, pp. 911–914, 2002, doi: 10.1002/1521-3951(200201)229:2<911::AID-PSSB911>3.0.CO;2-R.

[22] S. J. Pearton, D. P. Norton, K. Ip, Y. W. Heo, and T. Steiner, “Recent progress in processing and properties of ZnO,” in Superlattices and Microstructures, Academic Press, 2003, pp. 3–32. doi: 10.1016/S0749-6036(03)00093-4.

[23] L. Zhu, Y. Xiang, Y. Liu, K. Geng, R. Yao, and B. Li, “Comparison of piezoelectric responses of flexible tactile sensors based on hydrothermally-grown ZnO nanorods on ZnO seed layers with different thicknesses,” Sens Actuators A Phys, vol. 341, Jul. 2022, doi: 10.1016/j.sna.2022.113552.

[24] F. Bernardini, V. Fiorentini, and D. Vanderbilt, “Spontaneous polarization and piezoelectric constants of III-V nitrides,” Phys Rev B Condens Matter Mater Phys, vol. 56, no. 16, pp. R10024–R10027, 1997, doi: 10.1103/PhysRevB.56.R10024.

[25] H. Morkoç and Ü. Özgür, “Zinc Oxide: Fundamentals, Materials and Device Technology”. 2009. doi: 10.1002/9783527623945.ch1.

[26] A. Maache, “N. Benouattas,A. Chergui, D. Djouadi,A. Chala,A. Souici,A. Chelouche ‘Elaboration et caractérisation optique des couches minces de ZnO dopé ou Co-dopé obtenues par méthode sol-gel’ Soutenue par Ahmed MAACHE,” 2021.

[27] G. Jellison and L. Boatner, “Optical functions of uniaxial ZnO determined by generalized ellipsometry,” Phys Rev B Condens Matter Mater Phys, vol. 58, no. 7, pp. 3586–3589, 1998, doi: 10.1103/PhysRevB.58.3586.

[28] M. Liu, A. H. Kitai, and P. Mascher, “Point defects and luminescence centres in zinc oxide and zinc oxide doped with manganese,” J Lumin, vol. 54, no. 1, pp. 35–42, 1992, doi: 10.1016/0022-2313(92)90047-D.

[29] K. Vanheusden, W. L. Warren, C. H. Seager, D. R. Tallant, J. A. Voigt, and B. E. Gnade, “Mechanisms behind green photoluminescence in ZnO phosphor powders,” J Appl Phys, vol. 79, no. 10, pp. 7983–7990, 1996, doi: 10.1063/1.362349.

[30] Z. Fang, Y. Wang, D. Xu, Y. Tan, and X. Liu, “Blue luminescent center in ZnO films deposited on silicon substrates,” Opt Mater (Amst), vol. 26, no. 3, pp. 239–242, 2004, doi: 10.1016/j.optmat.2003.11.027.

[31] E. Zehani, “Etude du dopage dans les nanofils d'oxyde de zinc.” . Thèse de doctorat. Versailles-St Quentin en Yvelines, 2015.

[32] J. Petersen, C. Brimont, M. Gallart, O. Crégut, G. Schmerber, P. Gilliot, & A. Dinia, “Structural and photoluminescence properties of ZnO thin films prepared by sol-gel process,” J Appl Phys, vol. 104, no. 11, pp. 1–6, 2008, doi: 10.1063/1.3021358.

[33] F. Güell, & P.R. Martínez-Alanis, “Tailoring the Green, Yellow and Red defect emission bands in ZnO nanowires via the growth parameters,” Journal of Luminescence, 210, 128-134. (2019)

[34] T. A. Safeera, N. Johns, P. V. Athma, P. V. Sreenivasan, and E. I. Anila, “Synthesis and characterization of ZnO nanoparticles,” AIP Conf Proc, vol. 1620, no. May 2009, pp. 572–577, 2014, doi: 10.1063/1.4898299.

[35] A. Moustaghfir, “Élaboration et caractérisation de couches minces d'oxyde de zinc. Application à la photoprotection du polycarbonate, ” 2004. Thèse de doctorat. Université Blaise Pascal-Clermont-Ferrand II.

[36] J. A. Dumesic, G. W. Huber, & M. Boudart, “Principles of heterogeneous catalysis.” Handbook of heterogeneous catalysis: Online. (2008).

[37] F. Mahcene, “Synthèse par Sol-gel et caractérisation structurale et optique de nano poudres de ZnO pures et dopées en Aluminium (0.1, 0.5, 0.75, 1, 5, 7, 10, 15 et 20% at). ” 1955. Thèse de doctorat. Université Frères Mentouri-Constantine 1.

[38] L. Palanikumar, S. N. Ramasamy, and C. Balachandran, “Size-dependent antimicrobial response of zinc oxide nanoparticles,” IET Nanobiotechnol, vol. 8, no. 2, pp. 111–117, 2014, doi: 10.1049/iet-nbt.2012.0008.

[39] M. A. Ansari, H. M. Khan, A. A. Khan, A. Sultan, and A. Azam, “Characterization of clinical strains of MSSA, MRSA and MRSE isolated from skin and soft tissue infections and the antibacterial activity of ZnO nanoparticles,” World J Microbiol Biotechnol, vol. 28, no. 4, pp. 1605–1613, Apr. 2012, doi: 10.1007/s11274-011-0966-1.

[40] W. M. Abdelraheem, R. M. M. Khairy, A. I. Zaki, and S. H. Zaki, “Effect of ZnO nanoparticles on methicillin, vancomycin, linezolid resistance and biofilm formation in Staphylococcus aureus isolates,” Ann Clin Microbiol Antimicrob, vol. 20, no. 1, Dec. 2021, doi: 10.1186/s12941-021-00459-2.

[41] A. J. Huh and Y. J. Kwon, “‘Nanoantibiotics’: A new paradigm for treating infectious diseases using nanomaterials in the antibiotics resistant era,” Journal of Controlled Release, vol. 156, no. 2, pp. 128–145, 2011, doi: 10.1016/j.jconrel.2011.07.002.

[42] S. Riahi, N. B. Moussa, M. Lajnef, N. Jebari, A. Dabek, R. Chtourou, and E. Herth, “Bactericidal activity of ZnO nanoparticles against multidrug-resistant bacteria,” J Mol Liq, vol. 387, Oct. 2023, doi: 10.1016/j.molliq.2023.122596.

[43] S. Chakraborti, A. K. Mandal, S. Sarwar, P. Singh, R. Chakraborty, and P. Chakrabarti, “Bactericidal effect of polyethyleneimine capped ZnO nanoparticles on multiple antibiotic resistant bacteria harboring genes of high-pathogenicity island,” Colloids Surf B Biointerfaces, vol. 121, pp. 44–53, 2014, doi: 10.1016/j.colsurfb.2014.03.044.

[44] F. A.G. Soares Silva, M. Carvalho, T. Bento de Carvalho, M. Gama, F. Poças, and P. Teixeira, “Antimicrobial activity of in-situ bacterial nanocellulose-zinc oxide composites for food packaging,” Food Packag Shelf Life, vol. 40, Dec. 2023, doi: 10.1016/j.fpsl.2023.101201.

[45] F. B. Firouzabadi, M. Noori, Y. Edalatpanah, and M. Mirhosseini, “ZnO nanoparticle suspensions containing citric acid as antimicrobial to control Listeria monocytogenes, Escherichia coli, Staphylococcus7 aureus and Bacillus cereus in mango juice,” Food Control, vol. 42, pp. 310–314, 2014, doi: 10.1016/j.foodcont.2014.02.012.

[46] L. S. Reddy, M. M. Nisha, M. Joice, and P. N. Shilpa, “Antimicrobial activity of zinc oxide (ZnO) nanoparticle against Klebsiella pneumoniae,” Pharm Biol, vol. 52, no. 11, pp. 1388–1397, 2014, doi: 10.3109/13880209.2014.893001.

[47] M. Rehan Ansari, P. Agrohi, and K. Rao Peta, “Effect of citric acid on structural, optical, morphological properties of ZnO and the bactericidal applications against human pathogenic bacteria E. coli DH5α,” Mater Today Proc, Jan. 2024, doi: 10.1016/j.matpr.2024.01.009.

[48] Y. Liu, L. He, A. Mustapha, H. Li, Z. Q. Hu, and M. Lin, “Antibacterial activities of zinc oxide nanoparticles against Escherichia coli O157:H7,” J Appl Microbiol, vol. 107, no. 4, pp. 1193–1201, 2009, doi: 10.1111/j.1365-2672.2009.04303.x.

[49] J. R. Giudicessi, & M.J. Ackerman, “Determinants of incomplete penetrance and variable expressivity (in heritable cardiac arrhythmia syndromes, ” Translational Research, 161(1), 1-14. (2013)

[50] R. Dastjerdi and M. Montazer, “A review on the application of inorganic nano-structured materials in the modification of textiles: Focus on anti-microbial properties,” Colloids Surf B Biointerfaces, vol. 79, no. 1, pp. 5–18, 2010, doi: 10.1016/j.colsurfb.2010.03.029.

[51] A. Sirelkhatim, S. Mahmud, A. Seeni, N. H. M. Kaus, I. C. Ann, S. K. M. Bakhori,... & D. Mohamad, “Review on zinc oxide nanoparticles: Antibacterial activity and toxicity mechanism,” Nanomicro Lett, vol. 7, no. 3, pp. 219–242, 2015, doi: 10.1007/s40820-015-0040-x.

[52] A. F. Radovic-Moreno, T. K. Lu, V. A. Puscasu, C. J. Yoon, R. Langer, and O. C. Farokhzad, “Surface charge-switching polymeric nanoparticles for bacterial cell wall-targeted delivery of antibiotics,” ACS Nano, vol. 6, no. 5, pp. 4279–4287, 2012, doi: 10.1021/nn3008383.

[53] M. A. Subhan, N. Neogi, and K. P. Choudhury, “Industrial Manufacturing Applications of Zinc Oxide Nanomaterials: A Comprehensive Study,” Nanomanufacturing, vol. 2, no. 4, pp. 265–291, Dec. 2022, doi: 10.3390/nanomanufacturing2040016.

[54] A.Valour, “Synthèse d'oxyde de zinc dopé azote sous formes de poudre et de couche mince: caractérisation du type de semiconductivité.” 2017. Thèse de doctorat. Université de Rennes.

[55] J. Wang, R. Chen, L. Xiang, and S. Komarneni, “Synthesis, properties and applications of ZnO nanomaterials with oxygen vacancies: A review,” Ceram Int, vol. 44, no. 7, pp. 7357–7377, 2018, doi: 10.1016/j.ceramint.2018.02.013.

[56] Ü., Özgür, Y. L. Alivov, C. Liu, A. Teke, M. A. Reshchikov, S. Doğan, and A. Morkoç., “A comprehensive review of ZnO materials and devices,” J Appl Phys, vol. 98, no. 4, pp. 1–103, 2005, doi: 10.1063/1.1992666.

[57] B. J. Lokhande, P. S. Patil, and M. D. Uplane, “Studies on structural, optical and electrical properties of boron doped zinc oxide films prepared by spray pyrolysis technique,” Physica B Condens Matter, vol. 302–303, pp. 59–63, 2001, doi: 10.1016/S0921-4526(01)00405-7.

[58] M. Salem, H. Ghannam, A. Almohammedi, J. Salem, I. R. Bouazzi, I. Massoudi, & M. Gaidi, “Improved photoelectrochemical sensitivity of Al-doped ZnO nanostructure prepared by co-precipitation and spin-coating techniques,” Mater Lett, vol. 352, Dec. 2023, doi: 10.1016/j.matlet.2023.135085.

[59] A. F. Abdulrahman, A. N. Abdulqodus, and M. A. Almessiere, “Biosynthesis of Al-doped ZnO nanoparticles with different Al doping ratio for methylene orange dye degradation activity,” Ceram Int, vol. 49, no. 22, pp. 34920–34936, Nov. 2023, doi: 10.1016/j.ceramint.2023.08.165.

[60] I. Serhiienko, A. Novitskii, T. Sviridova, E. Kolesnikov, E. Chernyshova, K. Kuskov, & T. Mori, “Microstructure and thermoelectric properties of pristine and Al-doped ZnO ceramics fabricated by cost-effective and eco-friendly wet chemistry methods,” J Alloys Compd, vol. 976, Mar. 2024, doi: 10.1016/j.jallcom.2023.173106.

[61] P. C. Yao, S. T. Hang, and M. J. Wu, “Growth characteristics and properties of Al-doped ZnO thin films by DC magnetron sputtering from AZOY® target,” Transactions of the Canadian Society for Mechanical Engineering, vol. 37, no. 3, pp. 303–312, 2013, doi: 10.1139/tcsme-2013-0020.

[62] M. Gabás, A. Landa-Cánovas, J. Luis Costa-Krämer, F. Agulló-Rueda, A. R. González-Elipe, P. Díaz-Carrasco, & J. Ramón Ramos-Barrado, “Differences in n-type doping

efficiency between Al- and Ga-ZnO films," J Appl Phys, vol. 113, no. 16, 2013, doi: 10.1063/1.4803063.

[63] M. A. Kamran, W. Ali, S. Ullah, T. Alharbi, and Q. Gul, "Facile preparation of Ga-doped ZnO nanostructures by composite-hydroxide-mediated synthesis route for high-performance pseudocapacitors," J Energy Storage, vol. 62, Jun. 2023, doi: 10.1016/j.est.2023.106871.

[64] M. Miki-Yoshida, F. Paraguay-Delgado, W. Estrada-López, and E. Andrade, "Structure and morphology of high quality indium-doped ZnO films obtained by spray pyrolysis," Thin Solid Films, vol. 376, no. 1–2, pp. 99–109, 2000, doi: 10.1016/S0040-6090(00)01408-5.

[65] T. Minami, T. Yamamoto, and T. Miyata, "Highly transparent and conductive rare earth-doped ZnO thin films prepared by magnetron sputtering," Thin Solid Films, vol. 366, no. 1–2, pp. 63–68, 2000, doi: 10.1016/S0040-6090(00)00731-8.

[66] C. Hong, K. M. Kang, M. Kim, Y. Wang, T. Kim, C. Lee, & H. H. Park, "Structural, electrical, and optical properties of Si-doped ZnO thin films prepared via supercycled atomic layer deposition," Materials Science and Engineering: B, vol. 273, Nov. 2021, doi: 10.1016/j.mseb.2021.115401.

[67] Lv, Y. B., Dai, Y., Yang, K., Zhang, Z., Wei, W., Guo, M., & Huang, B, "Density functional investigation of structural, electronic and optical properties of Ge-doped ZnO," Physica B Condens Matter, vol. 406, no. 20, pp. 3926–3930, Oct. 2011, doi: 10.1016/j.physb.2011.07.029.

[68] M. Divya Gnaneswari, M. Karunakaran, L. Bruno Chandrasekar, J. Merciline Leonora, and P. Shunmuga Sundaram, "Chemically prepared p-type Sn doped ZnO nanoparticles: Synthesis, characterization and its antibacterial properties," J Cryst Growth, vol. 627, no. August 2023, p. 127548, 2024, doi: 10.1016/j.jcrysgro.2023.127548.

[69] K. Gueddouch, M. Zidane, R. Temsamani, A. Mrigal, M. Addou, and S. Ettami, "Structural, optical and electrical properties of F doped ZnO films: Experimental and theoretical study," Mater Today Proc, vol. 66, pp. 151–157, Jan. 2022, doi: 10.1016/j.matpr.2022.04.293.

[70] G. M. Fortes, A. L. da Silva, L. B. Caliman, F. C. Fonseca, and D. Gouvêa, “Interfacial segregation in Cl−-doped nano-ZnO polycrystalline semiconductors and its effect on electrical properties,” Ceram Int, vol. 47, no. 17, pp. 24860–24867, 2021, doi: 10.1016/j.ceramint.2021.05.212.

[71] V. Kumar, A. M. Álvarez, Y. M. Kuwabara, Y. Koudriavstev, and M. De, “Materials Science in Semiconductor Processing Effect of co-doping concentration on structural , morphological , optical and electrical properties of aluminium and indium co-doped ZnO thin fi lms deposited by ultrasonic spray pyrolysis,” Mater Sci Semicond Process, vol. 47, pp. 32–36, 2016, doi: 10.1016/j.mssp.2016.02.011.

[72] D. C. Look, “Progress in ZnO materials and devices,” J Electron Mater, vol. 35, no. 6, pp. 1299–1305, 2006, doi: 10.1007/s11664-006-0258-y.

[73] T. K. Gupta and R. L. COBLE, “Sintering of ZnO: I, Densification and Grain Growth,” Journal of the American Ceramic Society, vol. 51, no. 9, pp. 521–525, 1968, doi: 10.1111/j.1151-2916.1968.tb15679.x.

[74] A. Sedky, M. Abu-Abdeen, and A. A. Almulhem, “Nonlinear I-V characteristics in doped ZnO based-ceramic varistor,” Physica B Condens Matter, vol. 388, no. 1–2, pp. 266–273, 2007, doi: 10.1016/j.physb.2006.06.149.

[75] L. Arab. “Elaboration par différentes méthodes et étude optique de poudres nanocristallines de ZnO pur et dopé par différents oxydes.” Doctoral dissertation, Thèse de Doctorat, Université de Constantine. 2012.

[76] D. Banerjee, J. Y. Lao, D. Z. Wang, J. Y. Huang, Z. F. Ren, D. Steeves, & M. Sennett, “Large-quantity free-standing ZnO nanowires,” Appl Phys Lett, vol. 83, no. 10, pp. 2061–2063, 2003, doi: 10.1063/1.1609036.

[77] R. Wahab, S. G. Ansari, Y. S. Kim, H. K. Seo, and H. S. Shin, “Room temperature synthesis of needle-shaped ZnO nanorods via sonochemical method,” Appl Surf Sci, vol. 253, no. 18, pp. 7622–7626, 2007, doi: 10.1016/j.apsusc.2007.03.060.

[78] X. Y. Kong, Y. Ding, R. Yang, and Z. L. Wang, “Single-Crystal Nanorings Formed by Epitaxial Self-Coiling of Polar Nanobelts,” Science (1979), vol. 303, no. 5662, pp. 1348–1351, 2004, doi: 10.1126/science.1092356.

[79] W. P. Zhen, R. D. Zu, and L. W. Zhong, “Nanobelts of semiconducting oxides,” Science (1979), vol. 291, no. 5510, pp. 1947–1949, 2001, doi: 10.1126/science.1058120.

[80] J. J. Wu, S. C. Liu, C. T. Wu, K. H. Chen, and L. C. Chen, “Heterostructures of ZnO-Zn coaxial nanocables and ZnO nanotubes,” Appl Phys Lett, vol. 81, no. 7, pp. 1312–1314, 2002, doi: 10.1063/1.1499512.

[81] A. J. Haider, F. I. Sultan, and A. Al-Nafiey, “Controlled growth of different shapes for ZnO by hydrothermal technique,” AIP Conf Proc, vol. 1968, 2018, doi: 10.1063/1.5039272.

[82] M. José-Yacamán, C. Gutierrez-Wing, M. Miki, D. Q. Yang, K. N. Piyakis, and E. Sacher, “Surface diffusion and coalescence of mobile metal nanoparticles,” Journal of Physical Chemistry B, vol. 109, no. 19, pp. 9703–9711, 2005, doi: 10.1021/jp0509459.

[83] A. Kolodziejczak-Radzimska and T. Jesionowski, “Zinc oxide-from synthesis to application: A review,” Materials, vol. 7, no. 4, pp. 2833–2881, 2014, doi: 10.3390/ma7042833.

[84] R. S. Ganesh et al., “ZnO hierarchical 3D-flower like architectures and their gas sensing properties at room temperature,” Appl Surf Sci, vol. 449, pp. 314–321, 2018, doi: 10.1016/j.apsusc.2018.01.199.

[85] W. Gao and Z. Li, “Nanostructures of zinc oxide,” Int J Nanotechnol, vol. 6, no. 3–4, pp. 245–257, 2009, doi: 10.1504/IJNT.2009.022917.

[86] Y. Liu, Y. Li, and H. Zeng, : “doping ZnO-based transparent conductive thin films films : doping ,” Hindawi Publishing Corporation, vol. 2013, no. Cvd, 2013.

[87] A. Laghouage , H. Bencheikhe , “Etude et simulation d’une cellule solaire à

base des éléments chalcogènes,” 2018.

[88] V. Dobrokhotov, L. Oakes, D. Sowell, A. Larin, J. Hall, A. Kengne, & D. N. McIlroy, “ZnO coated nanospring-based chemiresistors,” J Appl Phys, vol. 111, no. 4, 2012, doi: 10.1063/1.3686212.

[89] M. Hjiri, F. Bahanan, M. S. Aida, L. El Mir, and G. Neri, “High Performance CO Gas Sensor Based on ZnO Nanoparticles,” J Inorg Organomet Polym Mater, vol. 30, no. 10, pp. 4063–4071, 2020, doi: 10.1007/s10904-020-01553-2.

[90] D. Choron, “Élaboration et caractérisation de varistances à fort champ de seuil à base d’oxyde de zinc” Doctoral dissertation, Université de Caen Basse Normandie.(2015)

[91] L. M. Levinson, & H. R. Philipp, “Zinc oxide varistors—a review,” American Ceramic Society Bulletin, 65(4), 639-646. (1986).

[92] W. Is, a L. Varistor, and P. Properties, “Terminology and Theory,” pp. 89–101, 1999.

[93] M. Ebrahimizadeh Abrishami, A. Kompany, and S. M. Hosseini, “Varistor behavior of Mn doped ZnO ceramics prepared from nanosized precursors,” J Electroceram, vol. 29, no. 2, pp. 125–132, 2012, doi: 10.1007/s10832-012-9753-0.

[94] J. W. MEDERNACH and R. L. SNYDER, “Powder Diffraction Patterns and Structures of the Bismuth Oxides,” Journal of the American Ceramic Society, vol. 61, no. 11–12, pp. 494–497, 1978, doi: 10.1111/j.1151-2916.1978.tb16125.x.

[95] W. G. Carlson and T. K. Gupta, “Improved varistor nonlinearity via donor impurity doping,” J Appl Phys, vol. 53, no. 8, pp. 5746–5753, 1982, doi: 10.1063/1.331463.

[96] R. Einzinger, Metal oxide varistors. Annual Review of Materials Science, 17(1), 299-321. (1987).

Chapter II

Materials and experimental methods

II. 1. Introduction

The second chapter describes the elaboration method of zinc oxide powder, the experimental techniques employed in this research, their fundamentals, and the sample preparation. Finally, the initial characterization of the elaborated powder is presented:

- Experimental methods;
- Samples preparation;
- Techniques for characterization of ZnO Nanopowders.

II. 2. Experimental methods

As indicated in the first chapter, zinc oxide nanopowder comprises zinc oxide particles that have been reduced to nanoscale dimensions using different processes such as chemical vapour deposition, precipitation, mechanical milling, and sol-gel synthesis. Such methods allow for controlling particle size, shape, and surface qualities, resulting in the material's performance in different applications.

Every technique has its advantages and can produce various ZnO nanostructures. This later can appear as simple nanoparticles, nanorods, nanobelts, branched nanorods, nanowires, ultranarrow nanobelts, hierarchical nanostructures, nanocombs, nanosprings, nanospirals, nanorings, core–shell nanostructures, nanocages, nanoflowers, and nanotubes, among other structures [1,2].

- ***Synthesis of ZnO nanostructures***

The synthesizes zinc oxide nanostructure has been generally recently reviewed using various technique as shown in figure (II.1).

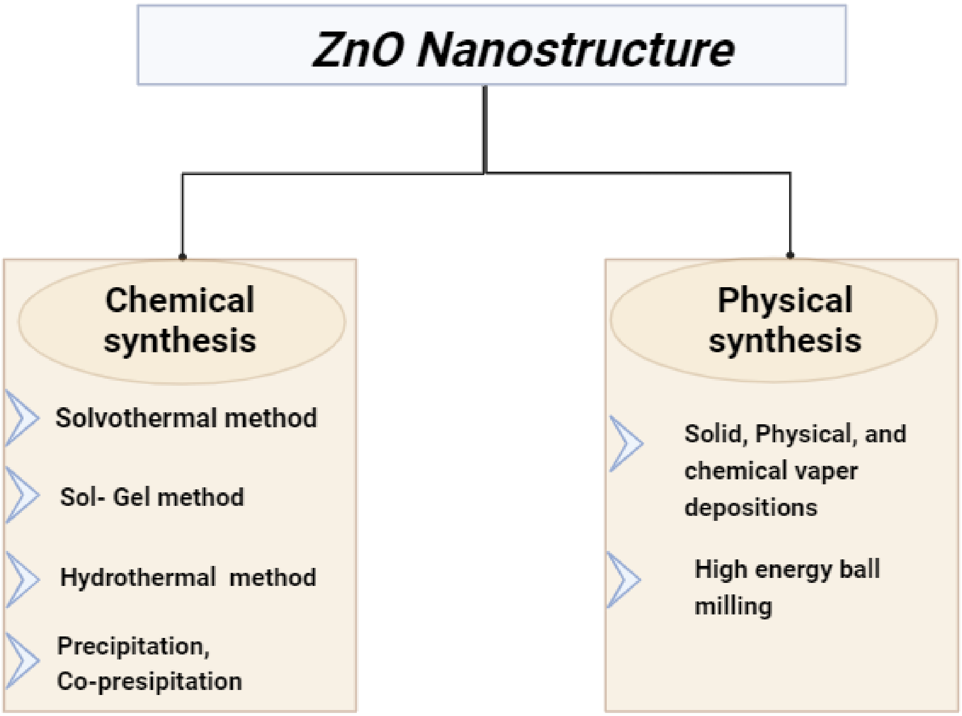

Figure II. 1: Various techniques for the production of ZnO nanoparticles.

II. 2.1. Sol-Gel

The sol-gel method is one of the most extensively used techniques for producing ZnO nanoparticles because of its good homogeneity [3, 4], simplicity of composition control, low processing temperature, large-area coating, cheap equipment cost, and excellent optical qualities [5]. Using precursor solutions, this method yields materials used for the synthesis of glasses, ceramics, and organic-inorganic hybrid compounds. Under mild chemical conditions, it allows the formation of thin layers made of stacked nanoparticles of metal oxides. The temperatures at which this procedure is conducted are substantially lower than those of traditional synthesis techniques. This method has several uses, including encapsulation and creating very porous materials, but its primary use is in making thin film deposits.

The methodology of the sol-gel technique, which was once referred to as "soft chemistry," is to create oxide networks that a sequence can thermally treat hydrolysis-condensation processes carried out at a moderately warm temperature. Metal alkoxides are being transformed into a solution by this procedure. Furthermore, the soluble metal species can include organic components that may be changed based on the applications of soluble metal species.

The term "sol-gel" is a combination of "solution" and "gelation." Before reaching the gel state, the system is a liquid form, consisting of a mixture of colloidal oligomers and very small macromolecules, as well as different partly hydrolyzed monomers, depending on the intensity of the polymerization reaction. The steady dispersion of colloidal particles inside a liquid is called a "sol." The size of the solid particles, which are denser than the liquid, must be small enough that gravity does not overpower the forces responsible for dispersion.

The gel is composed of an oxide network swollen by the solvent, with chemical bonds maintaining mechanical cohesion and giving the material a rigid and non-deformable nature (a gel can have elastic behaviour but no macroscopic viscosity). The gel is equivalent to a three-dimensional network of Vander-Waals bonds. The time it takes for a "sol" to convert into a "gel" is referred to as the gelation time (or gelation point).

- *Inorganic or colloidal route*: produced in aqueous solution from metallic salts (chlorides, nitrates, oxychlorides). Since this method is economical, however difficult to regulate, it is rarely employed. Nonetheless, it is the primary way of obtaining ceramic materials.
- *Metal-organic or polymeric route*: metal alkoxides in organic solutions are used. This technology is quite expensive but provides simple particle size control. The reaction is begun in both cases by hydrolysis (adding water for the alkoxide pathway and changing the pH to generate hydroxides for the inorganic route), permitting the creation of M-OH groups. Condensation follows, resulting in the production of M-O-M bonds. Figure II.2 depicts both synthesis methods.

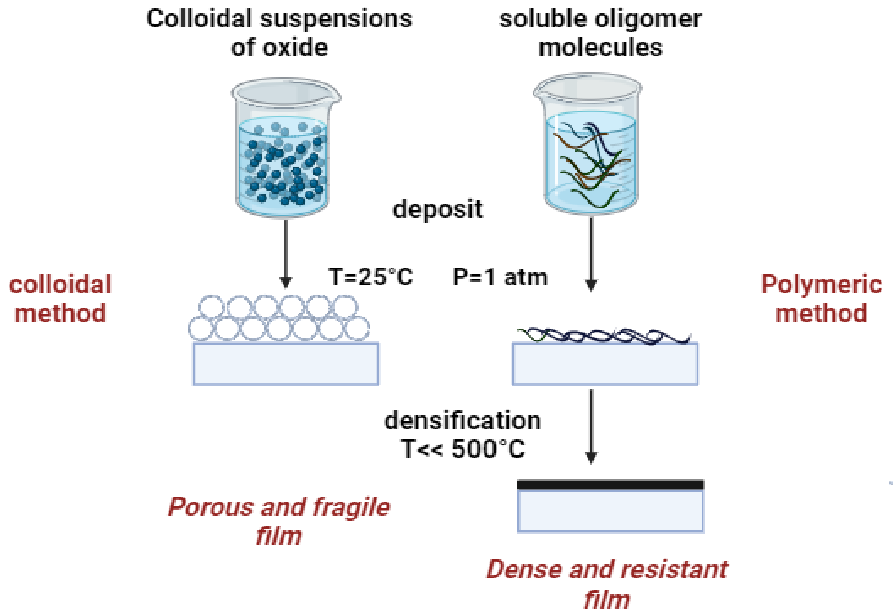

Figure II.2 : Sol-gel process.

II. 2.2 Predominant Chemical Reactions

This procedure uses molecular precursors in the solution that, via polymerization processes, progressively change into a network of oxides. A precursor, usually a metal alkoxide with the formula M(OR)n, where M is a metal with a valence of n and R is an alkyl chain of the type ($-C_nH_{2n+1}$), is added to the first solution along with a solvent, and sometimes water and a catalyst. It's important to remember that the right solvent and catalyst are chosen based on the chemical composition of the precursor [6]. The predominant reactions can be categorized into two groups [7]:

II. 2.2.a. Hydrolysis reaction

The hydrolysis of a substance is its decomposition by water through the H^+ and OH^- ions originating from the dissolution of water (Figure II.3). Thus, it is the nucleophilic substitution of an -OH ligand with an -OR ligand. This reaction involves the consumption of water and the release of alcohol, specifically hydroxyl groups (R-OH) [8] as shown in the following chemical reaction:

$$M-(OR)_n + H_2O \rightarrow HO-M-(OR)_{n-1} + R-OH$$

The resulting solution is referred to as a sol.

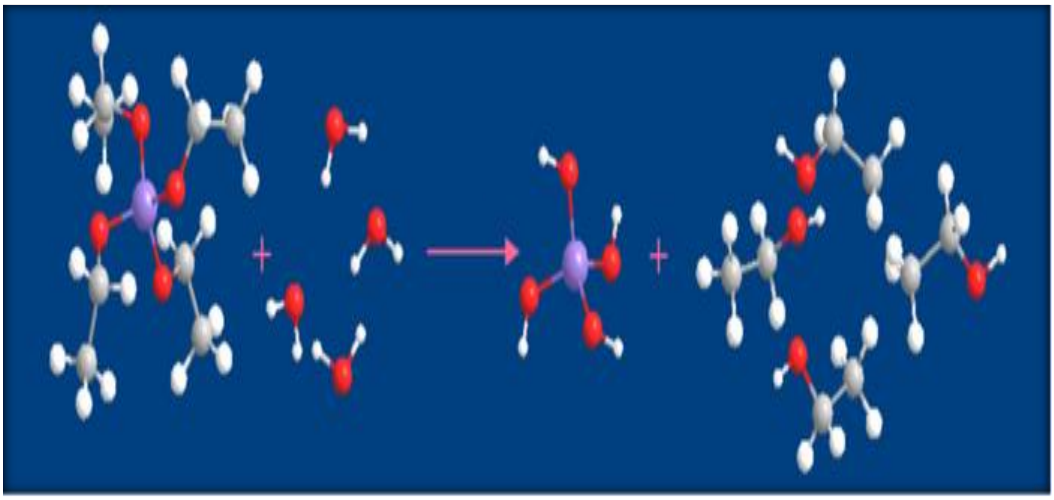

● : Matériau M, ● : oxygène , ● : carbone, ○ : hydrogène

Figure II.3: Schematization of the hydrolysis process

II. 2.2.b. *Condensation Reaction*

The (HO-M (-OR) n-1) groups, generated during hydrolysis, react either with each other, resulting in the elimination of a water molecule (reaction 2), or with a molecule of the alkoxide M(-OR), leading to the production of an alcohol molecule (reaction 1). This consequently leads to the creation of M-O-M bridges where each oxygen atom acts as a bridge connecting two atoms of the metal M. This process leads to gel formation with increasing viscosity over time. This gel contains solvents and precursors that have not yet reacted (Figure II.4) [9].

These reactions occur at room temperature, governed by the following processes:

$$(OR)_{n-1}-M-OH + RO-M-(OR)_{n-1} \rightarrow (OR)_{n-1}-M-O-M-(OR)_{n-1} + R-OH \qquad (1)$$

$$(OR)_{n-1}-M-OH + HO-M-(OR)_{n-1} \rightarrow (OR)_{n-1}-M-O-M-(OR)_{n-1} + H_2O \qquad (2)$$

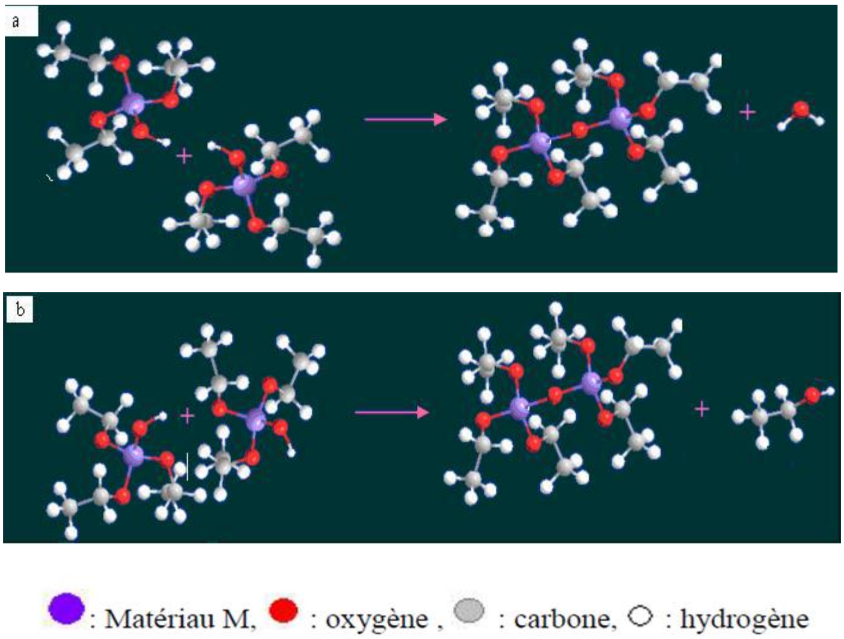

Figure II.4: condensation process; a: water production, b: alcohol production

II. 2.3. The Sol-Gel Transition

Polymeric clusters whose size increases over time are formed during the polymerization process. When one of these clusters reaches an infinite dimension, essentially the container's size, the viscosity becomes infinite. This is known as the sol-gel transition point. This point is illustrated in figure II.5.

From then on, the cluster continues evolving by incorporating smaller polymeric groups. Once all the bonds have been utilized, the gel is formed.

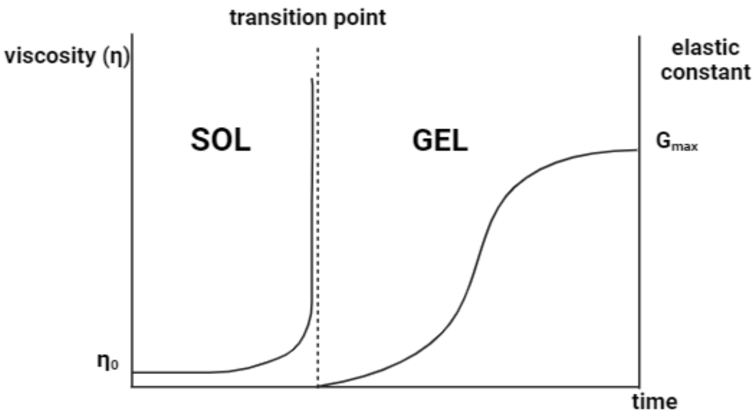

Figure II.5: Evolution of the solution viscosity and the elastic constant of the gel.

The tg point corresponds to the time the sol-gel transition is achieved [10]. Figure II.4 illustrates the mechanical behaviour of the solution as it shows the evolution of the viscosity of the sol and its Coulomb modulus G (elastic constant) as a function of time. The viscosity becomes infinite once the gel is fully formed, and the constant G tends to its minimum value.

II. 2.4. Gelation and Gel Structure

The reactions mentioned above lead to gelation and the formation of a gel composed of M-O-M (or M-OH-M) chains, with its viscosity increasing over time. This gel still contains unreacted solvents and precursors. The 'gel' phase in the sol-gel process is defined and characterized by a 3D solid 'skeleton' embedded in a liquid phase. The solid phase is typically a condensed polymeric sol where particles are interlocked to form a three-dimensional network (Figure II.6).

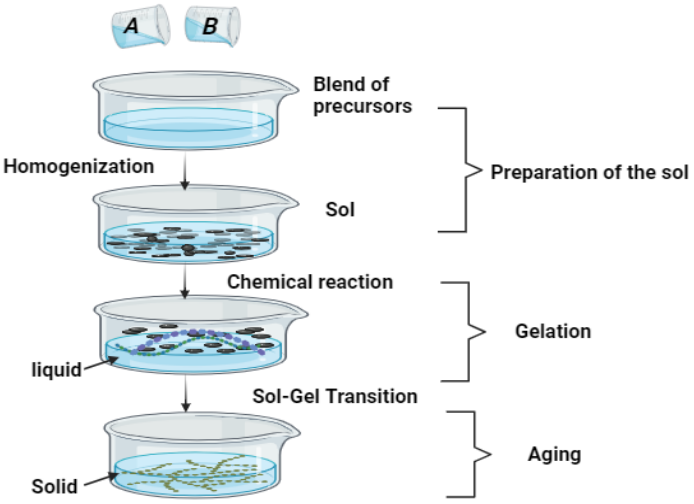

Figure II.6: The different stages of sol-gel formation.

The reactions leading to the formation of this material are conducted at room temperature. The parameters influencing these reactions include temperature, pH, precursor, and solvent.

II. 2.5. Heat Treatment

Once the formulation of the solution is complete, it is possible to prepare the desired material in various forms, whether they are bulk, thin films, or powder. Gels must be dried for many applications, i.e., undergo a solvent removal operation.

II. 2.5.a Gel Drying

Once gelled, the material undergoes drying due to capillary forces within the pores, resulting in volume shrinkage. The drying process to obtain the sol-gel material requires that alcohol or water can escape as the gel solidifies. The evaporation occurs through holes and channels in the porous sol-gel material.

Several drying methods yield different types of materials:

- **Xerogel:** classical drying (normal evaporation) reduces the volume from 5 to 10%.

The evaporation of the solvent allows the formation of a xerogel, which can undergo a moderate-temperature thermal treatment to densify the material. The densification temperatures strongly depend on the type of material and the desired properties. The drying of the gel constitutes a delicate step. The solvent needs to evaporate very slowly to avoid the fragmentation of the xerogel. Thus, achieving a solid material is challenging due to internal tensions that arise during drying and can lead to material cracking.

- **Aerogel:** Drying under critical conditions (in an autoclave under elevated pressure) results in little to no volume shrinkage. Evacuating the solvent under supercritical conditions leads to the formation of an aerogel that has not undergone densification. This results in a highly porous material with exceptional insulation properties. The transition from a solution to a gel, whose viscosity can be controlled, also allows for the production of fibres and various film supports through immersion or vaporization.

Xerogels are generally denser than aerogels. From the same solution and depending on the gel drying method, the final material takes on very different forms: dense or massive materials (glass or ceramic monoliths), powders, aerogels (supercritical drying), fibres, composites, porous gels or membranes, and, of course, films or thin layers (Figure II.7).

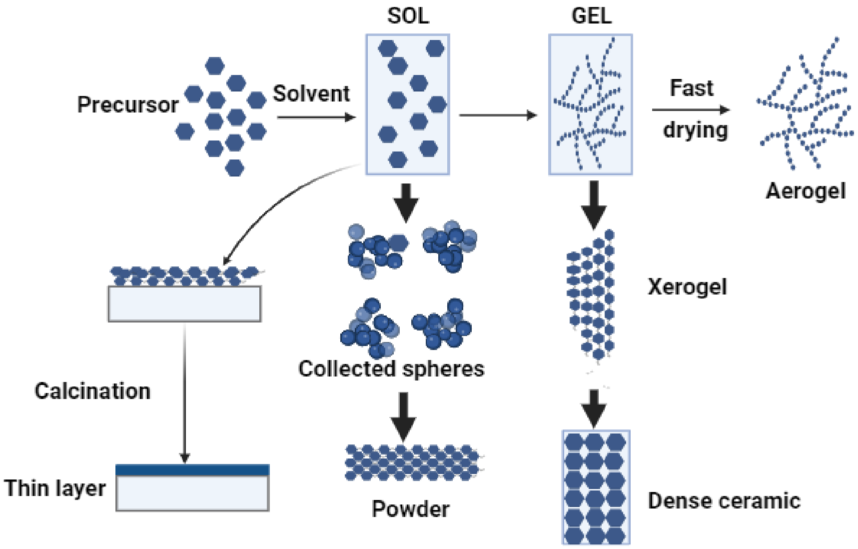

Figure II.7: Diversity of sol-gel materials and their shaping [11].

II. 2.5.b Annealing

The thermal treatment, or annealing, is distinct from the drying phase; this phase is crucial in the material formation process. Annealing serves two main purposes: the elimination of organic species present in the initial solution and the densification of the material.

Annealing is generally carried out at temperatures ranging from 300°C to 700°C; conventional annealing will be referred to in the subsequent text and within this temperature range. These annealing processes will be referred to as high-temperature annealing for higher temperatures. Gaseous oxygen is often injected into the furnace during annealing to expedite the removal of carbonaceous species at a given temperature.

If drying occurs at a fixed (limited) temperature for a given solvent, annealing processes are carried out over a wide range of temperatures and variable holding durations. The second characteristic of annealing is material contraction. Like drying, this phenomenon is responsible for the emergence of mechanical stresses in the deposited thin film. Pore closure accelerates during annealing; a reduction in volume accompanies this contraction. This reduction takes place within the plane of the thin layer as well as in its thickness. Another source of stress resulting from annealing is the potential difference in thermal expansion coefficients between the material deposited as a thin layer and the substrate. The substrate, much thicker than the layer, imposes its deformation on the thin layer, which, being fixed to the substrate, may develop fissures or destructive cracks to release the film's stress. Such defects can render samples unusable for study or application.

II. 2.6. Advantages of the sol-gel method

- Versatile: better control of the structure, including porosity and particle size; the possibility of incorporating nanoparticles and organic materials into sol-gel-derived oxides.
- Extended composition ranges: it allows the fabrication of any oxide composition, but also some non-oxides, as well as the production of new hybrid organic-inorganic materials, which do not exist naturally.
- Better homogeneity: high purity due to mixing at the molecular level.
- Less energy consumption: there is no need to reach the melting temperature since the network structure can be achieved at relatively low temperatures near Tg.
- Coatings, thin films, monoliths, composites, porous membranes, powders, and fibres.
- No need for special or expensive equipment.

II. 2.7. Drawbacks of the sol-gel method

- Cost of precursors.
- Shrinkage of a wet gel upon drying often leads to fracture due to the generation of significant capillary stresses, making the attainment of large monolithic pieces difficult.
- Preferential precipitation of a particular oxide during sol formation (in multicomponent glasses) due to the different reactivity of the alkoxide precursors.
- Difficult to avoid residual porosity and OH groups.

II. 3. Preparation of ZnO powder

II. 3.1. Used Chemical Precursors

The precursor products are grouped in the following table:

Table II. 1: The physical and chemical parameters of the chemical precursors used.

Properties / Chemical Product	Molar Mass (g)	melting point (°C)	Boiling Point (°C)	Chemical Formula	Nature	Density (g/cm^3)
Hydrated zinc acetate	219.48	-	-	$Zn(CH_3COO)_2$, $2H_2O$	Crystal granules	1.735
Monohydrated citric acid	210	110	135	$C_6H_8O_7$, H_2O	Crystal granules	1.5
Ethylene glycol	62.07	-12	198	$C_2H_6O_2$	Colorless and liquid	1.11
Bismuth nitrate	485.07	33	80	$Bi(NO_3)_3,5H_2O$	Crystal granules	2.83
Gallium nitrate	255.73	110	-	Ga(NO3)3 • xH2O	Crystal granules	1.29

II. 3.2. The different stages of the synthesised powder

To synthesize nanopowders of ZnO pure using the Sol-Gel method, the following procedure was employed: Starting with zinc acetate dissolved in ethylene glycol with a concentration of C_1 and citric acid also dissolved in ethylene glycol with a concentration of C_2, both solutions were heated to a temperature of 130°C. The two solutions were mixed once the temperature of 130°C was reached. Homogeneity and temperature control of the bath, ensured by thermal contact and magnetic agitation.

Finally, the gel was placed in a crucible and subjected to calcination in an open-air furnace to remove any organic components that might be present (such as acetic acid and water). Ultimately, an excellent powder of zinc oxide was obtained (Figure II.8).

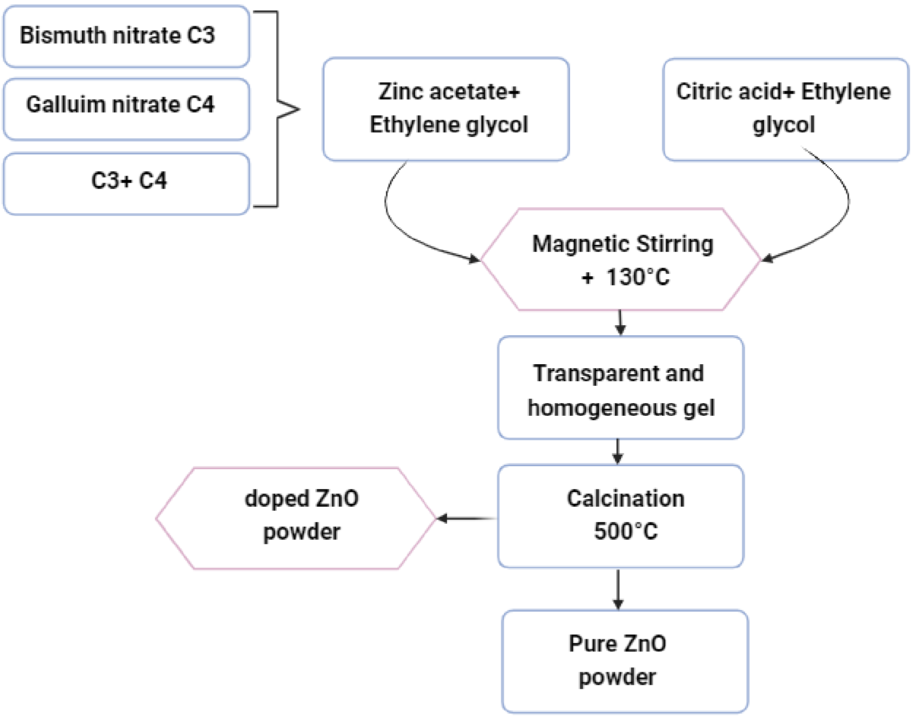

Figure II.8: Organogram of the Sol-Gel presents the Various Steps of Elaborating Pure, Doped, and co-Doped ZnO powder.

- **Calcination Treatment**

Calcination is an operation that involves transforming the gel into a powder by removing all traces of organic functions (acetic acid) and water vapours.

The thermal treatment was carried out in a Nobertherm furnace at a maximum temperature of 500°C, using containers that can withstand high temperatures.

The thermal cycle followed consists of a single stage of 4 hours at 500°C with a ramp-up and ramp-down speed of 6°C/min (Figure II.9)

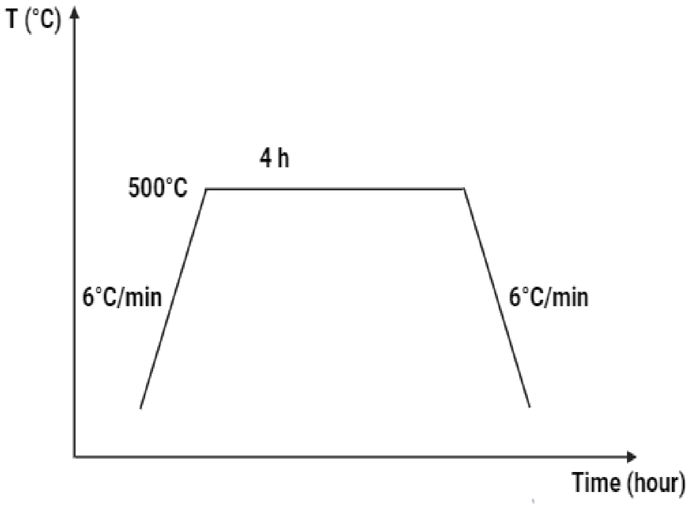

Figure II.9: Calcination treatment.

II. 3.3. Elaboration of doped zinc oxide nanopowder

The preparation of doped zinc oxide nanopowder is divided into three series. The first series involves zinc oxide doped with Bi, the second involves ZnO doped with Ga, and the last involves zinc oxide co-doped with both Bi and Ga.

The doped and co-doped zinc oxide is prepared by adding precursors of the dopant element to the AZ solution under the same conditions mentioned earlier in preparation of pure Zinc oxide, which are as follows:

- The concentration ratio C_1/C_2 is 0.06.
- The gelation temperature Tg = 130°C.
- The gelation time = 4 hours.
- Bismuth nitrate and Gallium nitrate were added as the Bi and Ga sources.

The assembly used to prepare pure and doped ZnO nanopowders by sol-gel, as shown in (Figure II.10).

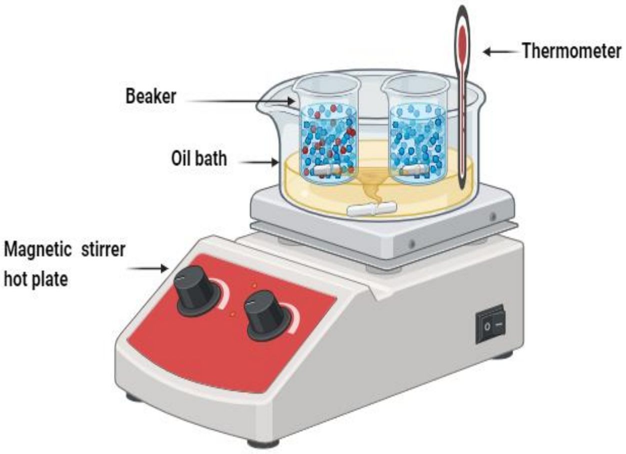

Figure II.10: Experimental setup used for preparing ZnO nanopowders through the Sol-Gel method.

II.4 . Characterization Method for Nanopowders

We characterized the obtained Zinc oxide powders using various methods: thermogravimetric analysis (TGA) and Differential Scanning Calorimetry (DSC) To study the thermal effects on the chemical and physical properties. X-ray diffraction (XRD) for structural study and stress evaluation, scanning electron microscopy (SEM) to observe the morphological structure, UV-visible spectroscopy for studying optical properties, and infrared analysis for compositional analysis.

II.4 .1. Thermal Analysis ATG/ DSC

Thermal analysis measures the changes in a sample's physical or chemical properties about temperature, time, or environment. This thesis covers thermal analysis techniques such as thermogravimetric analysis (TGA) and Differential Scanning Calorimetry (DSC).

II.4 .1.a Thermogravimetric analysis (TGA)

TGA determines the mass reductions in a sample when exposed to heating. This method measures the changes in the mass of a substance sample in relation to temperature or time. Thermogravimetry uses a precise balance in an oven where the temperature increases steadily over time. The data can be displayed as a thermogravimetric curve (TG curve) showing mass changes in relation to temperature or time or as a derivative thermogravimetric curve.

The basic thermogravimetry instrument is a precision balance put in an oven with a temperature set to rise linearly over time. The data might be presented as a thermogravimetric curve (TG curve), which depicts mass fluctuations as a function of temperature or time, or as a derivative thermogravimetric curve.

II.4 .1.b. Differential Scanning Calorimetry (DSC)

Differential Scanning Calorimetry (DSC) is a standard characterization technique that measures the variations in heat exchange between a sample and a reference. During heating or cooling, the changes that occur in a material are accompanied by a heat exchange: DSC allows the temperature of this transition to be determined and therefore the heat quantified.

Calorimetric measurements, often known as DSC, give qualitative and quantitative information regarding physical and chemical changes caused by endothermic or exothermic processes, as well as heat capacity changes. Any phase transition in the material causes heat exchange, which corresponds to an anomaly in the DSC signal. It would show a peak in the presence of latent heat during a first-order phase transition.

- **Apparatus**

The ATG and DSC measurements were performed on a SETRAMA LABSYSevo differential scanning calorimeter (Figure II.11). The sample was heated from room temperature to 800°C under a flow of argon with a heating rate of 30°C min^{-1}. With a mass of 30 mg, it is placed in a small crucible made of alumina.

Figure II.11: Thermal analysis apparatus (SETRAMA LABSYSevo).

- **Identifying the development of activation energy**

Activation energy Ea is the energy needed for the creation of one mole of the activated phase. Researchers have suggested many approximation techniques for determining. which differ depending on the experimental conditions and their nature. Among the most important of these conditions are temperature and the techniques used

Ozawa method

This method is defined by the following relationship [12].

$$\boldsymbol{\ln(\varphi) = -1.0516.\frac{Ea}{R}.\frac{1}{Tm} + c} \tag{II.1}$$

Where (φ) is the constant heating rate, (Ea) is the activation energy, (R) is the universal gas constant, and (Tm) is the peak temperature. The variation of ln (φ) as a function of 1/Tm is linear with a slope of $(-1.0516\ Ea/R)$. where Tm is the peak temperature of the mass change rate curve (DTG) or the longitudinal change rate curve (DSC).

Boswell method

This approach can be explained via the following relationship [13].

$$\boldsymbol{\ln\left(\frac{\varphi}{Tm}\right) = -\frac{Ea}{R}.\frac{1}{Tm} + c} \tag{II.2}$$

The variation of ln $(\frac{\varphi}{Tm})$ as a function of $\frac{1}{Tm}$ is linear with slope of $(-\frac{Ea}{R})$.

Kissenger method

This method allows obtaining the activation energy value from the plot of the function ln $(\frac{\varphi}{Tm^2})$ versus $\frac{1}{Tm}$ for a series of experiments with different heating rates (φ) [14]. The equation is written as follows:

$$\boldsymbol{\ln\left(\frac{\varphi}{Tm^2}\right) = \ln\left(\frac{RK_0}{E_a}\right) - \frac{E_a}{RTm}} \tag{II.3}$$

The value of $\ln\left(\frac{RK_0}{E_a}\right)$ approaches zero, so it can be considered negligible.

II. 4.2. X-ray Diffraction

X-ray diffraction (XRD) is a technique used in materials science to determine a material's atomic and molecular structure. To achieve this, a material sample is irradiated with incident X-rays. Then the intensities and angles of X-ray scattering are measured as the material disperses them. The intensity of the scattered X-rays is plotted as a function of the scattering angle, and the material's structure is determined by analyzing the positions and intensities of the scattered intensity peaks. Beyond measuring the average positions of atoms in the crystal, information about how the actual structure deviates from the ideal structure, resulting, for example, from internal stress or defects, can be determined.

This study aims to elucidate the structure of the ZnO samples and measure the crystallite size, lattice parameter and dislocation density.

II. 4.2. a. Apparatus

The acquisitions use a goniometer θ-2θ (BRUKER-AXS type D8) in steps of 2.5×10^{-3} degrees. The X-ray radiation used is the Kα line from a copper anticathode (λCu Kα =1.541838 Å). The apparatus setup is shown in figure II.12.

Figure II.12 : Diffractomètre de type (BRUKER-AXS type D8)

II. 4.2. b. Principle of X-ray Diffraction Measurements

The X-ray diffraction is performed on a crystal using the Bragg-Brentano goniometer method. In that case, a diffraction pattern is obtained representing the intensity of lines as a function of the detection angle 2θ. Measuring the diffraction angles allows easy access to interplanar distances and highlights preferred crystal orientations (Figure II.13) [15].

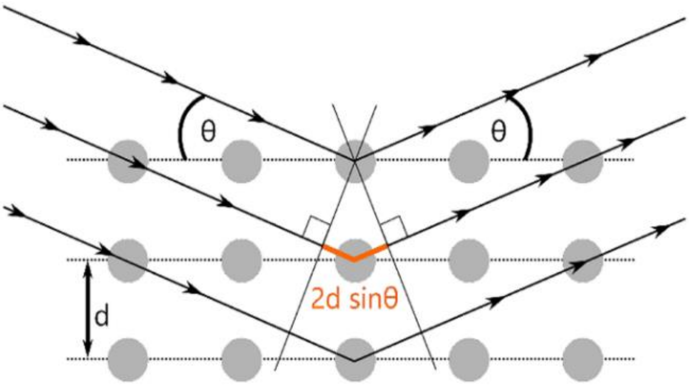

Figure II.13: Schematic of X-ray diffraction.

II. 4.2. c. Determination of interatomic distances and lattice parameters

The interplanar distances of different (hkl) planes are calculated using Bragg's law:

$$2d_{hkl}\sin\theta_{hkl} = n\lambda \tag{II.4}$$

Where λ is the wavelength of the diffracted radiation, n is the diffraction order, d_{hkl} is the interplanar spacing of the corresponding crystallographic plane, and θ_{hkl} is the diffraction angle. Comparing a diffractogram with JCPDS reference cards allows for determining lattice parameters. In the case of ZnO (hexagonal lattice), the relationship between interplanar spacings of the (hkl) planes and crystallographic parameters is as follows:

$$d_{hkl} = \frac{a}{\sqrt{\frac{4}{3}(h^2+k^2+hk)+l^2\frac{a^2}{c^2}}} \tag{II.5}$$

Comparing the obtained values for the parameters a and c with the theoretical values (a_0 = 3.249 Å and c_0 = 5.206 Å in JCPDS No. 5-664 datasheet) provides information about the state of stress in the considered powder.

The unit cell volume is estimated using the following relation

$$v = \frac{\sqrt{3}}{2}a^2c \tag{II.6}$$

II. 4.2. d. Determination of crystallite size

Infinite extension characterizes a perfect crystal, stretching limitlessly in all dimensions. However, the inherent finite dimensions of any crystal preclude it from achieving perfection. This departure from flawless crystalline structure leads to the broadening of diffraction peaks in materials. Analyzing the peak width yields two key insights: crystallite size and lattice strain. Lattice strain emanates from the distribution of lattice constants, resulting from imperfections like lattice dislocations [16]. Figure (II.14) illustrates an example of the XRD result of a Commercial ZnO sample prepared under the condition of a hexagonal wurtzite structure.

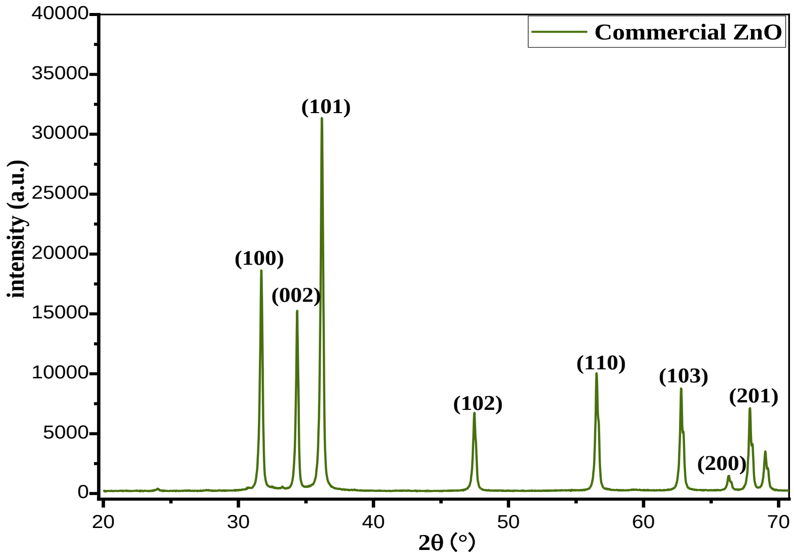

Figure II.14: X-ray Diffraction Spectrum (XRD) of commercial ZnO powder.

The analysis of X-ray profiles provides a simple and efficient approach for assessing both crystallite sizes and lattice strain. However, it was in 1918 that the pioneering researcher Paul Scherrer introduced the Scherrer equation. This equation aimed to determine the sizes of nanocrystallites (D) through the utilization of X-ray diffraction (XRD) wavelengths (A) measured in nanometers. This was achieved by calculating the peaks' full width at half maximum (FWHM) and the angular value (B) in radians corresponding to all 2θ peaks within the XRD pattern. Typically, the shape factor 'K' is considered around 0.89 [17]. The average nanocrystalline size was calculated using Debye-Scherrer's formula:

$$\boldsymbol{D = \frac{k\lambda}{\beta_{hkl}\cos\theta}} \qquad \textbf{(II.7)}$$

where

D = crystalline size.

K = shape factor (≈0.9).

λ =wavelength of $Cu_{k\alpha}$ radiation.

The strain induced in powders due to crystal imperfection and distortion was calculated using the formula:

$$\boldsymbol{\varepsilon = \frac{\beta_{hkl}}{4\tan\theta}} \qquad \textbf{(II.8)}$$

While the original Scherrer equation encounters limitations due to uncertainties in the crystallite shape factor (K), researchers have developed a modified version to estimate the sizes of nanocrystallites more accurately [18].

The standard method was developed in 1953. which is the Williamson-Hall method, through the past five decades. W-H plots emphasized the plots caused by strain. The peak's width derived from crystallite size differs from (1/cosθ) while the strain differs from (tanθ). This behavioural difference as a function of 2θ helps us differentiate between the strain's effects and the size of the peak expansion. Williamson-Hall's research simplified integral breadth approaches by deconvoluted sizes and strain-induced development when the width of peaks is the function of 2θ [19-21].

The significance of the broadening of peaks evidences grain refinement and the large strain associated with the powder. The instrumental broadening (β_{hkl}) was corrected, corresponding to each diffraction peak of ZnO material using the relation:

$$\boldsymbol{\beta_{hkl} = [((\beta_{hkl})^2)_{Measured} - ((\beta_{hkl})^2)_{Instrumental}]^{1/2}} \qquad \textbf{(II.9)}$$

From Equations 7 and 8, it was confirmed that the peak width from crystallite size varies as $\frac{1}{\cos\theta}$ strain varies as $tan\theta$. Assuming that the particle size and strain contributions to line broadening are independent of each other and both have a Cauchy-like profile, the observed line breadth is simply the sum of Equations 7 and 8.

$$\beta_{hkl} = \frac{k\lambda}{D\ \cos\theta} + 4\varepsilon \tan\theta \qquad \textbf{(II.10)}$$

By rearranging the above equation, we get

$$\beta_{hkl} \cos\theta = \frac{k\lambda}{D} + 4\varepsilon \sin\theta \qquad \textbf{(II.11)}$$

The above equations are W-H equations. A plot is drawn with 4sinθ along the x-axis and β_{hkl} cosθ along the y-axis for as-prepared ZnO nanoparticles.

From the linear fit to the data, the crystalline size was estimated from the y-intercept, and the strain ε, from the slope of the fit, where the strain was assumed to be uniform in all crystallographic directions, thus considering the isotropic nature of the crystal, where the material properties are independent of the direction along which they are measured. The Williamson-Hall plot for commercial ZnO nanoparticles is shown in figure II.15.

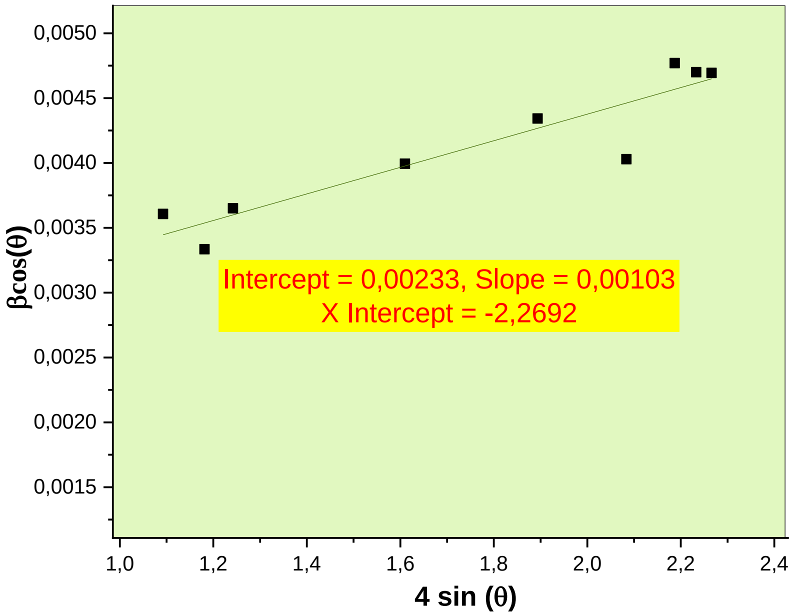

Figure II.15 : Williamson-Hall plot for commercial ZnO nanopowders.

II. 4.3. Scanning Electron Microscope (SEM)

Scanning electron microscopy (SEM) is a microscopy technique based on the principle of electron-matter interactions. A beam of electrons scans the sample's surface for analysis, emitting electrons and X-rays in response. Various detectors enable the analysis of electrons and reconstruction of a surface image. Scanning electron microscopes are powerful tools for characterizing materials, providing images of topography, revealing chemical composition, and more. They offer a very high depth of field.

II. 4.3.a Apparatus

A scanning electron microscope provides information in the form of images resulting from the interaction of an electron beam with a microscopic volume of the sample being studied. The main characteristics compared to those of an optical microscope are:

- SEM enables achieving a resolution on the order of 20 nm.
- Magnification can reach up to 300,000 times.

We used scanning electron microscopy (SEM) with an Energy-Dispersive X-ray Spectroscopy (EDS) made by ‘‘Thermo Fisher Scientific Quattro ESEM’’ (Figure (II.16)).

Figure II. 16 : Thermo fisher Scientific Quattro ESEM.

II. 4.3.b. Principle of SEM

Scanning Electron Microscopy is based on the irradiation of the sample by a focused beam of electrons, with an energy ranging from a few keV (5 to 20 keV), and the detection of electrons re-emitted by the sample. The interactions that occur during the irradiation of a sample by an electron beam are of several kinds (Figure II.17).

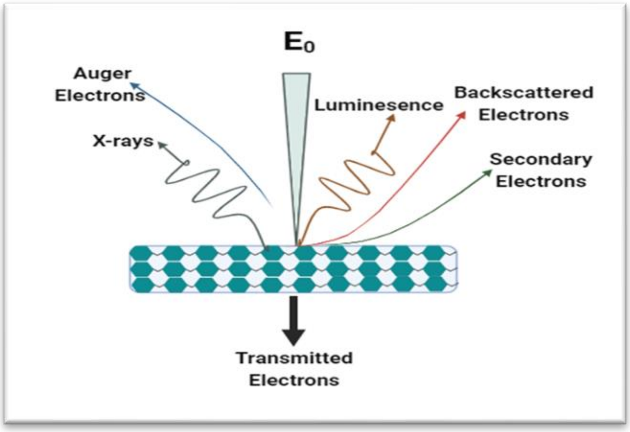

Figure II.17: Diagram of the products of interactions between the electron beam and material.

The emission of secondary electrons (SE) results from the ionisation of atoms in the sample by the electron beam and constitutes the primary source of electron contrast. These electrons, ejected from the atoms by the beam, have low energy (< 50 eV) and, therefore, have a very short mean free path in the material (10 nm). The image formed by this signal will provide information of a topographic nature with high spatial resolution; in our case, it is used to observe the samples, particularly the morphology of ZnO powder as shown in figure II.18.

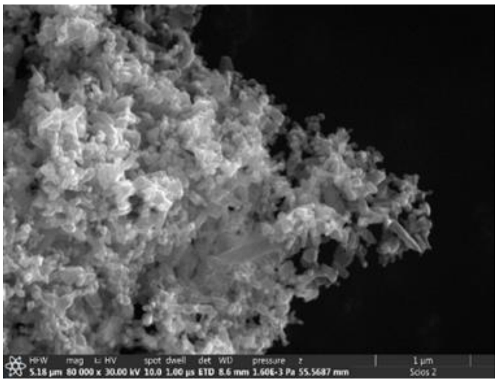

Figure II. 18 : SEM image of commercial ZnO powder.

The backscattered electrons constitute the second major source of contrast in electron imaging (B.S.E.: Back Scattering Electrons) resulting from interactions between the incident electron and the Coulomb fields of the electron clouds surrounding atoms within the target. These electrons originate from a larger volume around the point of impact (with a characteristic size of 100 nm) due to their higher energy. The contrast in the image obtained through the detection of these electrons is somewhat topographical but primarily atomic or compositional, as it depends on the number of charges of the atoms present in the irradiated pixel. Indeed, the backscattering efficiency increases monotonically with the atomic number of the target atoms.

Finally, the irradiated sample also emits photons (across a range from visible light to X-rays), originating from rearrangements in the electron cloud of atoms after ionization. Additional information about the analyzed material is obtained by combining the scanning electron microscope with a specific detector known as the Energy Dispersive Spectrometer (EDS)

We are interested in our study of secondary electron emission because it primarily provides information about the morphological structure of zinc oxide samples. We have utilised image J histogram in analysing the results of scanning electron microscopy, which assists in illustrating the surface shape and particle size, along with contrast, brightness, and threshold, thereby revealing high-resolution structural details.

II. 4.4. Ultraviolet-visible spectroscopy

A massive semiconductor has an electronic band configuration. Electrons are distributed according to the valence band and the conduction band. However, semiconductor nanocrystals exhibit discretization of energy levels [22-25], resulting in the widening of the bandgap. Consequently, an optical absorption spectrum consists of a set of peaks and absorption bands specific to the material under study. A qualitative analysis of this spectrum allows the identification, in our case study, of the presence of semiconductor nanocrystals ZnO [23].

II. 4.4.a. Apparatus

Ultraviolet-visible spectroscopy or UV-visible spectrometry involves photons with wavelengths in the ultraviolet range (200 nm – 400 nm), visible range (400 nm – 750 nm), or near-infrared range (750 nm -900 nm). The powders were pressed to a dimension of 17 mm diameter and a height of 4 mm under 1 MPa pressure for 2 min. The reflective spectra were measured in a V-750 spectrophotometer with a scanned rate of 5 nm/s (Figure II.19).

Figure II.19: V-750 UV-Visible Spectrophotometer.

II. 4.4.b. Principle of UV-visible spectrophotometer

Characterisation using the UV-Vis Spectrophotometer technique is crucial as it reveals the effect of nanoscale grain size on the optical properties of the material, thereby reinforcing the results obtained from X-ray diffraction (Figure II.20).

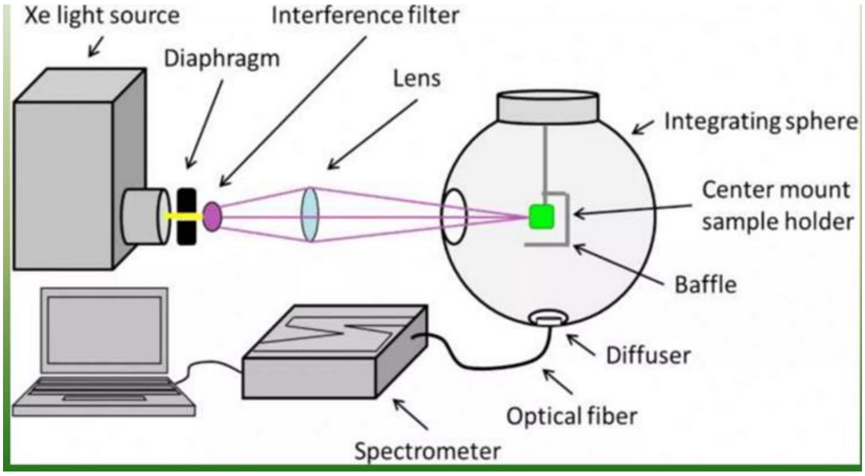

Figure II.20: The principle of UV-visible spectrometry [26]

For our samples, which is in the form of powders we dissolved the latter in HCl, as has been reported in a previous study [27, 28], and resulting solution was placed in 10 mm thick quartz cuvette. Absorption spectra allow the deduction of the absorption coefficient ε by the Beer-Lambert law [29].

$$\boldsymbol{A = \alpha \times l \times c} \qquad \textbf{(II.12)}$$

With: A: absorbance (A=Ln (I_0/I)) where I_0: initial intensity and I: intensity after passing through the cuvette (unitless).

α: absorption coefficient in $L.mol^{-1}.cm^{-1}$.

l: length of the optical path in the liquid = width of the cell = 1cm.

C: concentration of the compound under study in mol. L^{-1}.

Absorption spectra also allow deducing the energy of the band gap Eg using tauc's plot [30].

$$\boldsymbol{(\alpha h\nu) = A(h\nu - Eg)^{m}} \qquad \textbf{(II.13)}$$

The absorption coefficient of the samples is represented by α, photon energy by hν, and the absorbance by A, energy band gap by Eg, and a constant depending upon the band gap nature by m, where m = 2 or 1/2 for allowed direct and indirect band gap semiconductors respectively.

II. 4.5. Fourier transform infrared spectroscopy (ATR).

Fourier transform infrared spectroscopy (FTIR) using attenuated total reflection (ATR) is a powerful instrumental technique used to identify the functional groups of organic and inorganic materials by measuring the absorption and emission spectrum. The infrared absorption bands identify molecular components and structures. FTIR spectrometers (Fourier Transform Infrared Spectrometer) are widely used in organic synthesis, polymer science, petrochemical engineering, pharmaceutical industry, and food analysis. The FTIR method collects an interferogram of a sample signal. Then, it performs a Fourier transform (a mathematical algorithm) on the interferogram to obtain the infrared spectrum and convert the raw data into the actual spectrum. The infrared spectrum is a molecular vibrational spectrum.

The infrared beam is directed towards the Michelson interferometer, which modulates each beam wavelength at a different frequency. In the latter, a separator separates the incident light beam in half. These two parts will reflect on mirrors, one fixed and the other mobile. When the two beams recombine, destructive or constructive interference appears depending on the position of the moving mirror, as shown in (Figure II.21). The modulated beam is then reflected from the two mirrors to the sample, where absorptions occur. The beam then arrives on the detector to be transformed into an electrical signal.

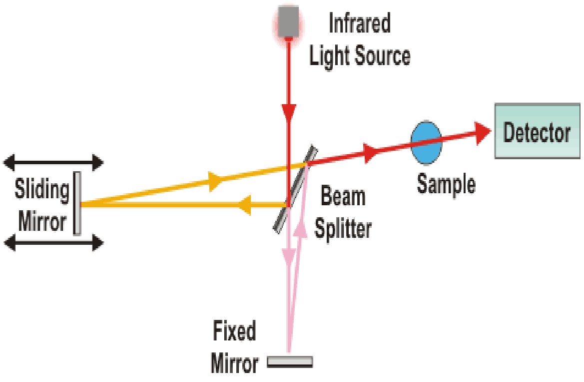

Figure II.21: Principles of infrared spectroscopy.

We use Fourier transform infrared spectrophotometry (FTIR Spectrometer, PerkinElmer. Spectrum 2000 Spectrometer) to identify surface materials groups (Figure II.22), with spectra ranging between 400 and 4000 cm^{-1}.

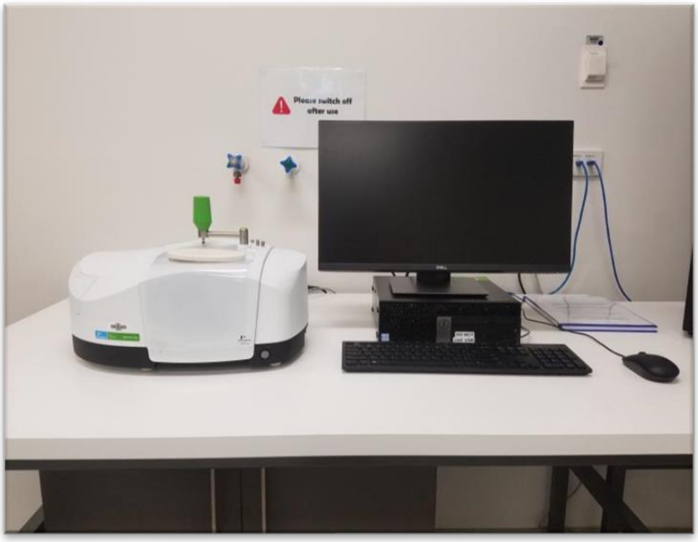

Figure II.22: Fourier transform infrared spectrophotometry (PerkinElmer Spectrum.

References

References

[1] L. Schmidt-Mende and J. L. MacManus-Driscoll, “ZnO - nanostructures, defects, and devices,” Materials Today, vol. 10, no. 5, pp. 40–48, 2007, doi: 10.1016/S1369-7021(07)70078-0.

[2] W. Gao and Z. Li, “Nanostructures of zinc oxide,” Int J Nanotechnol, vol. 6, no. 3–4, pp. 245–257, 2009, doi: 10.1504/IJNT.2009.022917.

[3] E. A. Meulenkamp, “Size dependence of the dissolution of ZnO nanoparticles,” Journal of Physical Chemistry B, vol. 102, no. 40, pp. 7764–7769, 1998, doi: 10.1021/jp982305u.

[4] Z. Hu, G. Oskam, R. L. Penn, N. Pesika, and P. C. Searson, “The influence of anion on the coarsening kinetics of ZnO nanoparticles,” Journal of Physical Chemistry B, vol. 107, no. 14, pp. 3124–3130, 2003, doi: 10.1021/jp020580h.

[5] S. S. Alias and A. A. Mohamad, “Synthesis of Zinc Oxide by Sol– Gel Method for Photoelectro- chemical Cells”. 2014.

[6] A. C. Pierre, “Introduction Sol-Gel Processing,” 1998. https://doi.org/10.1007/978-3-030-38144-8

[7] J. G. Mahy et al., “Eco-friendly colloidal aqueous sol-gel process for tio2 synthesis: The peptization method to obtain crystalline and photoactive materials at low temperature,” Catalysts, vol. 11, no. 7. MDPI, Jul. 01, 2021. doi: 10.3390/catal11070768.

[8] C. J. Brinker and G. W. Scherer, “Hydrolysis and Condensation I,” in Sol-Gel Science, Elsevier, 1990, pp. 20–95. doi: 10.1016/b978-0-08-057103-4.50007-6.

[9] H. Guendouz Hassan. “Elaboration par sol gel et caractérisation de nanoparticules de ZnO pur et dopé cuivre pour une application en photocatalyse, ” 2022. Thèse de doctorat. université de jijel.

[10] R, Sebastien. “Microcavités optiques élaborées par voie sol-gel: applications aux ions terre rare d'Eu3+ et aux nanocristaux semiconducteurs de CdSe, ” 2003. Thèse de doctorat. Université Claude Bernard-Lyon I.

[11] A. Chládová, J. Wiener, J. M. Luthuli, and V. Zajícová, “DYEING OF GLASS FIBRES BY THE SOL GEL METHOD,” AUTEX Research Journal, vol. 11, no. 1, pp. 18–23, Mar. 2011, doi: 10.1515/aut-2011-110104.

[12] T. Ozawa, “KINETIC ANALYSIS OF DERIVATIVE CURVES IN THERMAL ANALYSIS,” 1970.

[13] P. G. Boswell, “ON THE CALCULATION OF ACTIVATION ENERGIES USING A MODIFIED KISSINGER METHOD,” 1980.

[14] H. E. Kissinger, “Reaction Kinetics in Differential Thermal Analysis,” 1956.

[15] A. Moustaghfir, “Élaboration et caractérisation de couches minces d’oxyde de zinc.Application à la photoprotection du polycarbonate.” [Online]. Available: https://tel.archives-ouvertes.fr/tel-00012168

[16] M. Ahmadipour, M. J. Abu, M. F. Ab Rahman, M. F. Ain, and Z. A. Ahmad, “Assessment of crystallite size and strain of CaCu3Ti4O12 prepared via conventional solid-state reaction,” Micro Nano Lett, vol. 11, no. 3, pp. 147–150, 2016, doi: 10.1049/mnl.2015.0562.

[17] S. Kurapati and P. K. Srivastava, “Application of Debye-Scherrer Formula in The Determination of Silver Nano Particles Shape,” International Journal of Management, Technology And Engineering, vol. 8, no. XII, pp. 81–84, 2018.

[18] T. Sakae, O. Hiroyuki, H. Nakada, H. Ogawa, T. Tsukioka, T. Kaneda“X-ray micro-diffraction analysis revealed the crystallite size variation in the neighboring regions of a small bone mass,” J Hard Tissue Biol, vol. 26, no. 1, pp. 103–107, 2017, doi: 10.2485/jhtb.26.103.

[19] J. Gubicza, G. Ribárik, A. Borbély, and T. Ungár, “Crystallite size distribution and dislocation structure determined by diffraction profile analysis : principles and practical application to cubic and hexagonal crystals research papers Crystallite size distribution and dislocation structure determined by,” J Appl Crystallogr, pp. 298–310, 2001.

[20] J. I. Anusha Mony, “Fabrication and Analysis of Nanocrystalline Superconductor YSrBiCuO at Different Calcination Temperatures,” International Journal of Science and Research (IJSR), vol. 3, no. 12, pp. 2055–2063, 2014.

[21] V. Mote, Y. Purushotham, and B. Dole, “Williamson-Hall analysis in estimation of lattice strain in nanometer-sized ZnO particles,” Journal of Theoretical and Applied Physics, vol. 6, no. 1, pp. 2–9, 2012, doi: 10.1186/2251-7235-6-6.

[22] A. L. Efros and al. L. Efros, “Interband light absorption in semiconductor spheres,” Sov. Phys. Semicond., vol. 16, no. 7, pp. 772–775, 1982.

[23] Y. Kayanuma, “Quantum-size effects of interacting electrons and holes in semiconductor microcrystals with spherical shape,” Phys Rev B, vol. 38, no. 14, pp. 9797–9805, 1988, doi: 10.1103/PhysRevB.38.9797.

[24] S. Schmitt-Rink, D. A. B. Miller, and D. S. Chemla, “Theory of the linear and nonlinear optical properties of semiconductor microcrystallites,” Phys Rev B, vol. 35, no. 15, pp. 8113–8125, 1987, doi: 10.1103/PhysRevB.35.8113.

[25] M. Of and I. T. S. Excitations, “Excited Intrinsic,” Physical Review, vol. 42, no. 3, 1990.

[26] D. Mohamed, “Preparation and characterization of Titanium dioxide and Zinc oxide thin films via Sol-Gel (spin coating) technique for optoelectronic applications Speciality: Physics of thin films,” 2019.

[27] H. A. Thabit and N. A. Kabir, “The study of X-ray effect on structural, morphology and optical properties of ZnO nanopowder,” Nucl Instrum Methods Phys Res B, vol. 436, pp. 278–284, Dec. 2018, doi: 10.1016/j.nimb.2018.10.012.

[28] H. A. Thabit, N. A. Kabir, N. M. Ahmed, S. Alraddadi, and M. S. Al-Buriahi, “Synthesis, structural, optical, and thermoluminescence properties of ZnO/Ag/Y nanopowders for electronic and dosimetry applications,” Ceram Int, vol. 47, no. 3, pp. 4249–4256, Feb. 2021, doi: 10.1016/j.ceramint.2020.10.002.

[29] Beer. “Bestimmung der Absorption des rothen Lichts in farbigen Flüssigkeiten,” Annalen Der Physik Und Chemie, 162(5), 78–88. (1852). doi:10.1002/andp.18521620505

[30] J. Tauc, Optical Properties of Amorphous Semiconductors. In: Tauc, J. (eds) Amorphous and Liquid Semiconductors. Springer, Boston, MA. https://doi.org/10.1007/978-1-4615-8705-7_4

Chapter III

Undoped, doped, and co-doped zinc oxide properties

Introduction

This chapter aims to clarify the fundamental characteristics of zinc oxide (ZnO) powders. The chapter is organized into four parts, each focusing on a specific component of ZnO modification. In the first part, undoped zinc oxide powder samples were produced and analyzed thermally utilizing thermal analysis. We monitored the phase changes using several equipment (DSC, ATG). In order to improve our comprehension, the impact of doping on the different characteristics of zinc oxide powder has been investigated following an in-depth examination of zinc oxide production. The second part investigates the effects of Bismuth (Bi) doping on the characteristics of ZnO, specifically examining how this change alters the material. The third one examines the distinct properties of Gallium (Ga) doped ZnO and how Ga doping affects them. And the fourth part of the study examines the synergistic effects of gallium and bismuth dopants on ZnO. This part aims to thoroughly investigate and compare the properties arising from both dopants' presence in the material.

The tripartite approach enables a comprehensive analysis of the various alterations made to undoped ZnO, providing insight into the complex interaction between these dopants and their impact on the characteristics of the material.

Different characterizations obtain the results of this study: X-ray diffraction to determine the structural properties of these ZnO powders, Fourier Transform Infrared (FTIR-ATR) to determine the nature of the different bonds present in the nanopowders, Scanning electron microscopy (SEM) to examine the morphology and microstructure, and UV-Visible to study the optical properties.

Part I:

Preparation and Analytical Study of Zinc Oxide Powder

Introduction

This section focused on investigating the thermal behavior of zinc oxide formation using advanced techniques, including differential scanning calorimetry (DSC) and thermogravimetric analysis (ATG)**.** The study involved tracking the structural transformations of the powder before and after the formation process, as well as determining the energy required to form 1 mole of zinc oxide. The activation energy for the formation process was calculated using different computational methods.

III. 1.1. Preparation and analytical study of prepared undoped zinc oxide powder

III. 1.1.1. Preparation of Zinc Oxide Mixture.

To achieve a uniform solution, we have separately solved citric acid powder and zinc acetate in ethylene glycol, thoroughly mixing them using a magnetic stirrer. Subsequently, we have combined the two solutions, persistently agitating the combination, and maintain it at a constant temperature of 130 °C for a duration of 6 hours (elaborated instructions for this procedure can be found in Chapter 2). For the second step, we subjected the solution to a drying process in an oven set at 150 °C for 48 hours. Ultimately, we acquired a brown powder, which was meticulously pulverized for utilization in our study.

III.1.1.2. Thermal stability analysis of as-synthesized ZnO

To monitor the thermal characteristics and phase changes of zinc oxide powder made using the sol-gel method, we acquired the required dry mixture for zinc oxide powder creation. Afterward, it underwent heat treatment using a differential scanning calorimeter, starting from ambient temperature and reaching a maximum of 700 °C with a rapid heating rate of 30 °C/min in the presence of argon gas. This was conducted to check the phase changes that occur during zinc oxide production. Furthermore, an infrared spectroscopy apparatus was employed before and after to subject the dry mixture to various temperature gradients. The acquired results are illustrated in figure (III.1), where the DSC indicates that the powder experiences a sequence of endothermic and exothermic heat-absorbing transformations.

The thermal event recorded by TGA and DSC revealed three distinguishable zones when the sample heated from room temperature up to 700 °C (Figure III.1). The process started with slight weight loss (2.5 mg) beginning from 30 °C to offset 200 °C associated with a large endothermic curve (Tmax = 93°C), this is due to the evaporation of moisture and the release of acetate water [1]. Larger weight loss (21 mg) later occurred in zone B (280–410 °C) accompanied by the asymmetric of two shoulders exothermic effect observed at this temperature range (Tmax(1) = 345 °C, Tmax (2)= 410° C.), this may be attributed to the removal of leftover organic (acetate, CO_2)[2]. During the decomposition of zinc acetate, the zinc oxide phase is formed in the thermal field [410- 580 °C].

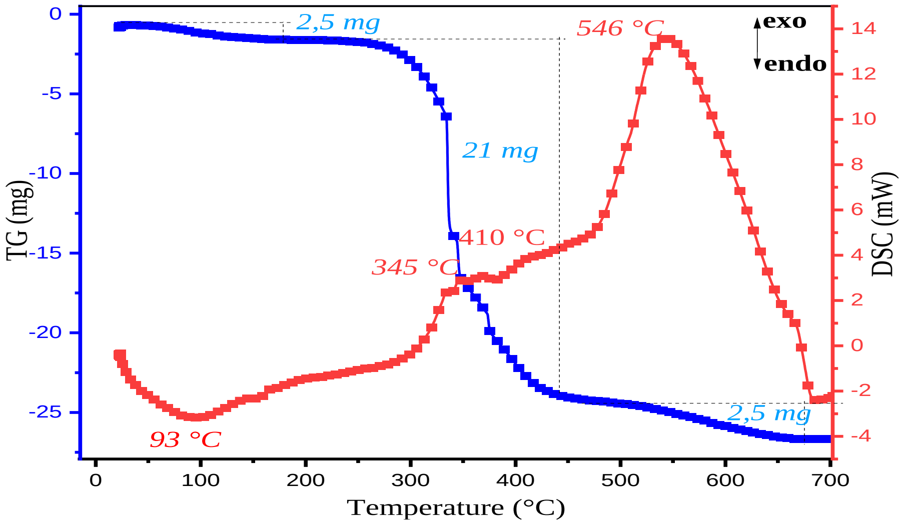

Figure III.1: TG-DSC pattern of sol–gel synthesized ZnO.

To confirm the DSC results, which showed the production of a crystalline phase at 500 degrees, we hypothesized that this is due to the creation of zinc oxide. Using X-ray diffraction research, we examined a sample of the dry mixture at a temperature of 25 °C and compared it to another sample that underwent heat treatment (DSC) up to 500 °C. We observed from figure III.2 that there is no distinct peak science on the first sample. The materials are amorphous. However, the second sample showed a well-defined pattern of ZnO with intense peaks at 31.820, 34.4560, 36.2507, 47.5469, and 56.7316 2θ degrees; all the diffraction peaks are well matched with hexagonal wurtzite structure, as indicated by the standard JCPDS data No. 00-036-1451 [3]. These peaks confirmed the composed of pure zinc oxide on the prominent exothermic peak of 500 °C.

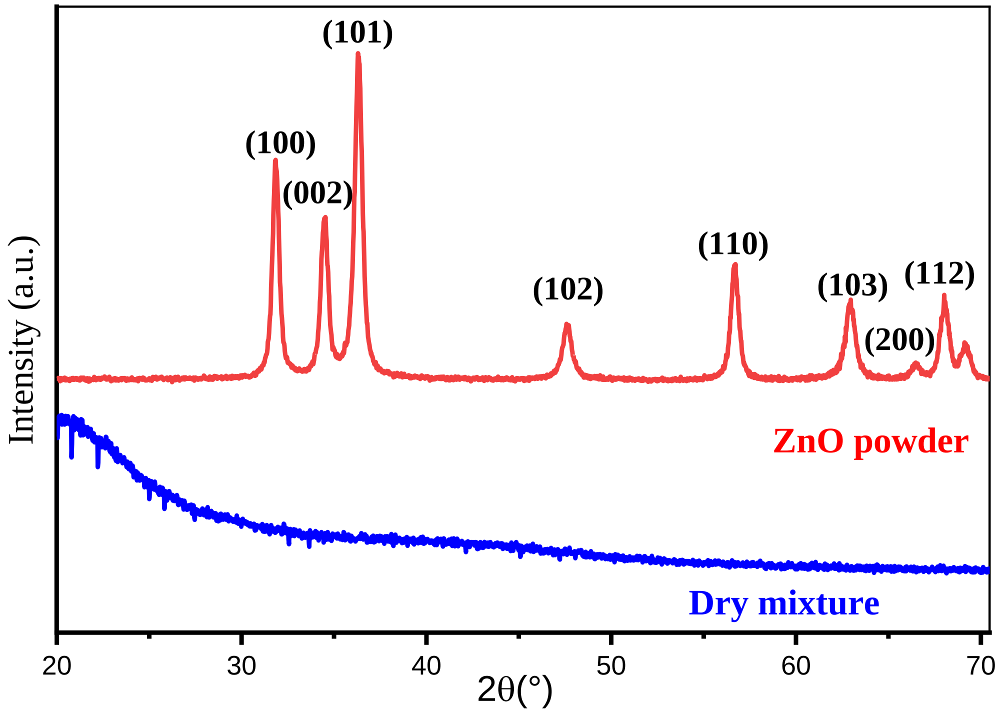

Figure III. 2: X-ray diffraction patterns of ZnO before and after DSC heat treatment.

On the other hand, to validate the findings of ATG, which showed a significant weight reduction that we interpreted as the volatilization of some molecules, we performed a prompt infrared spectroscopic examination before and following thermal treatment. The test findings are depicted in figure III.3, before the ATG heat treatment, the absorption peak is around 3452.62, 2949.2569, 2331.4824, 1725.14874,1164.5761, 1038.73327, 855.6891, 501.04 cm^{-1} which are due to the vibrations of O-H, C-H, O=C=O, (X-COOH) carboxylic acid, C-O, CH_3, C-C, and Zn-O respectively [4- 6]. However, these characteristic peaks of our first raw sample disappeared after the heat treatment (500 °C), indicating that the organic molecules had been removed completely.

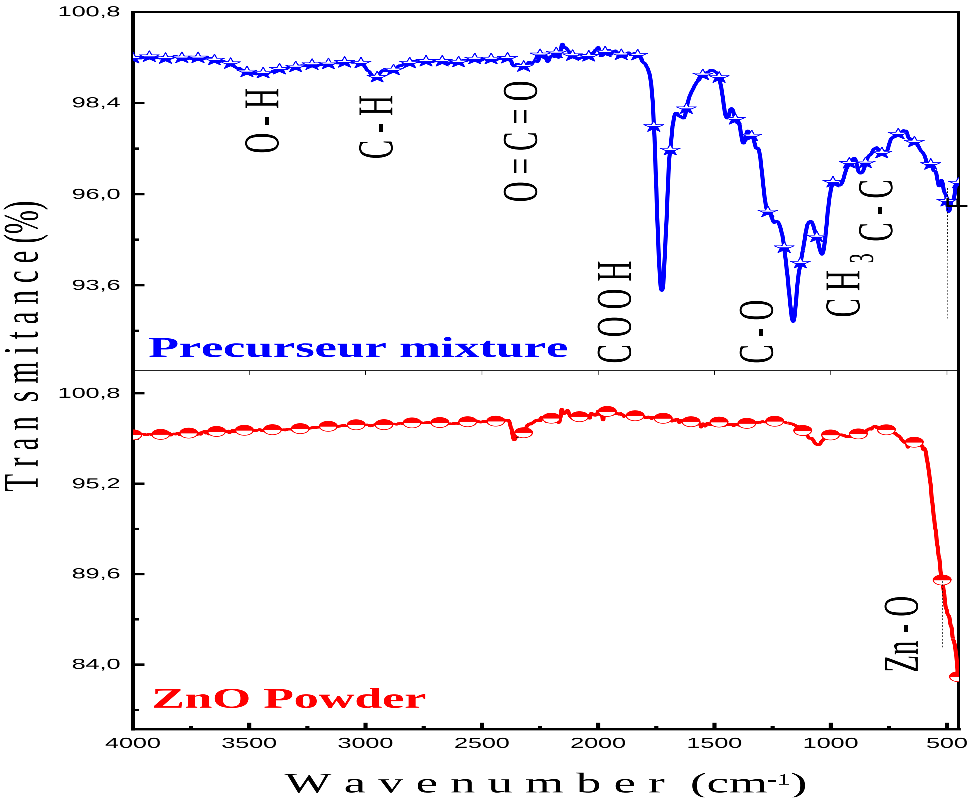

Figure III. 3: FTIR-ATR spectra of ZnO before and after ATG heat treatment.

III.1.1.3. Activation energy

Figure III.4 was constructed based on the differential scanning calorimetry (DSC) curve of the ZnO mixture obtained at three different heating rates (5, 10, and 20°C/min). We designated Tm as the highest recorded temperature, which signifies the occurrence of the Zinc oxide phase. Subsequently, we graphed the function Y as a function of the reciprocal of the temperature inverse (1/Tm) for the resulting phase. They function relates to the equations of Kissengre, Ozawa, and Boswell (II.1, 2, and 3), respectively. The values of these calculation methods are gathered in the table (III.1).

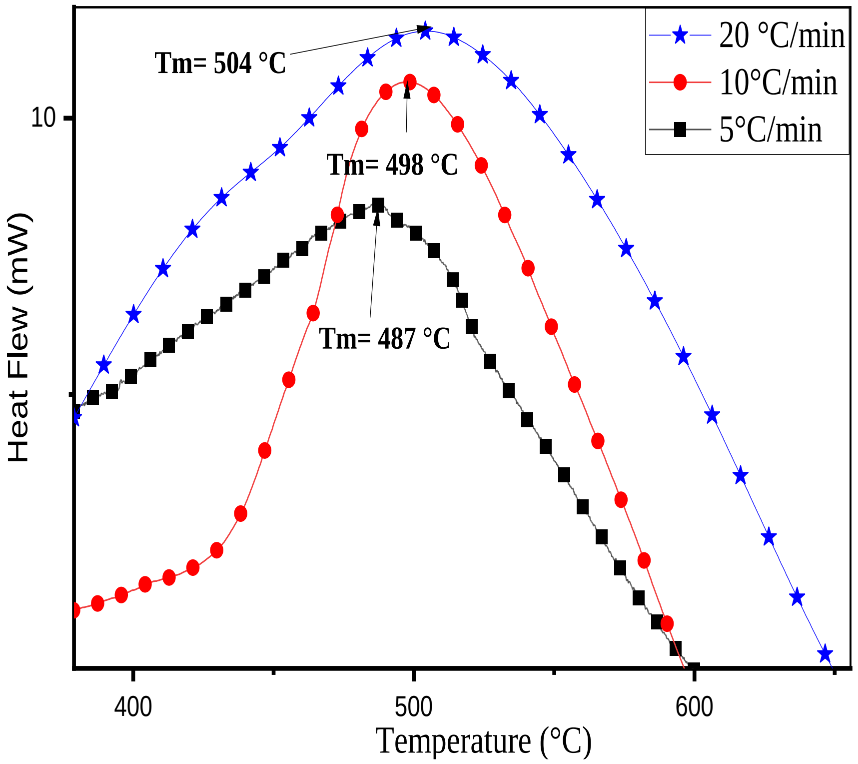

Figure III. 4: Curve of temperature changes in the form Curve of temperature changes in the formation of zinc oxide phase as a function of three different heating rates (Φ= 5, 10, and 20 °C/min).

The observe graph indicated that the temperature at which zinc oxide forms increases with the increasing heating rate.

Table III.1. values calculated by the three methods (Ozawa, Boswell, and Kissenger).

Ozawa				
Φ (°C/min)	Tm (°C)	Tm (K)	1/Tm	Ln (Φ)
5	487	760.15	1.3x10^{-3}	-2.48
10	498	771.15	1.29x10^{-3}	-1.79
20	504	777.15	1.28x10^{-3}	-1.09
Boswell				
Φ (°C/min)	Tm (°k)	1/Tm (K^{-1})	Φ/Tm	Ln (Φ/Tm)
5	760.15	1.3x10^{-3}	6.577X10^{-3}	-9.11
10	771.15	1.29x10^{-3}	12.96 X10^{-3}	-8.43
20	777.15	1.28x10^{-3}	25.74 X10^{-3}	-7.75
Kissenger				
Φ (°C/min)	Tm (°k)	1/Tm (K^{-1})	Φ /Tm^{2}	Ln (Φ/Tm^{2})
5	760.15	1.3x10^{-3}	8.65x10^{-6}	-15.75
10	771.15	1.29x10^{-3}	1.68x10^{-5}	-15.08
20	777.15	1.28x10^{-3}	3.31x10^{-5}	-14.41

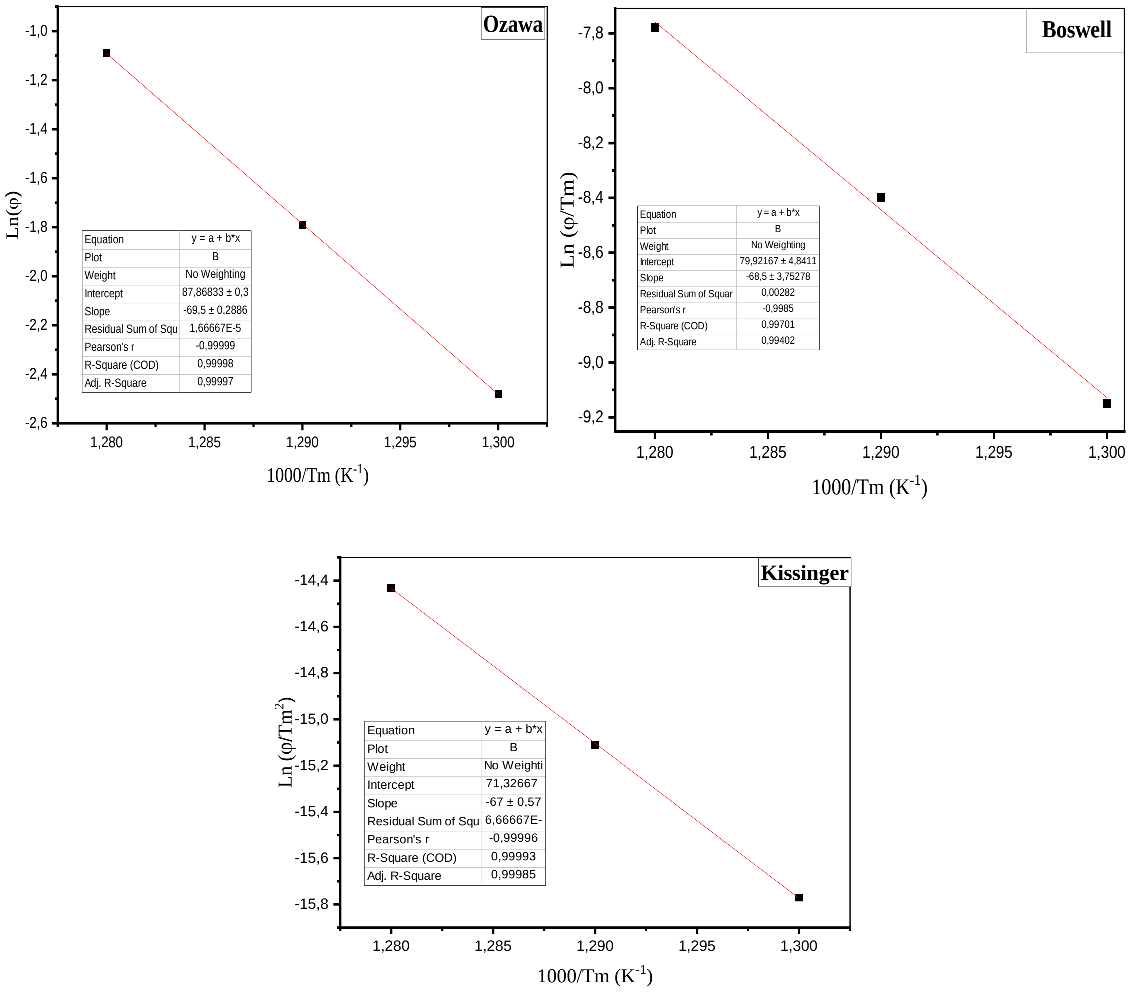

Figure III. 5: Variations in linear functions Ln(Φ), Ln(Φ/Tm), and Ln(Φ/Tm^2) are dependent on the slope of the temperature affecting the formation of zinc oxide phase.

After drawing a chart illustrating the changes in the previous linear function ln(Φ), ln(Φ/Tm), and ln(Φ/Tm^2) by reversing the temperature dependence for the hexagonal zinc oxide phase as illustrated in figure III.5, we then calculated the activation energy from the slopes of these functions and compared it with the activation energy equations. The activation energy values for this phase are summarized in table (III.2).

Table III. 2. Activation energy values for the formation of zinc oxide.

Method	R^2	Ea (KJ/mol)
Ozawa	0.9998	549.470
Boswell	0.9970	565.352
Kissenger	0.9999	557.038

Part II:

Zinc oxide doped with Bismuth

Introduction

In this part, we discussed the effect of dopant with bismuth atoms on Zinc oxide powder prepared with sol-gel method and calcined at 500°C. The doping concentration of Bismuth (Bi) systematically altered from 0 to 8% to investigation its impact on the structural, morphological, and optical characteristics. employing various analytical techniques such as X-ray diffraction (XRD), scanning electron microscopy (SEM), UV-Visible spectroscopy (UV-Vis), and Fourier-transform infrared (FTIR) spectroscopy.

III.2.1. Structural characterization

III.2.1.1. X-ray diffraction

The x-ray diffraction data presented in figure III. 6 provides a detailed understanding of the structural characteristics of both undoped (as reference) and Bi-doped ZnO nanopowder after being sintered at a temperature of 500 °C. The XRD patterns display diffraction peaks that closely align with the hexagonal wurtzite structure of ZnO, as indicated by the standard JCPDS data No. 00-036-1451 [7]. The diffraction peaks seen at ZnO: 6% Bi and ZnO: 8% Bi samples are denoted by an asterisk, indicating their extra presence. The authors concur with the primary diffraction patterns seen in the α-Bi_2O_3 monoclinic structure, as documented in the JSPDS data No. 00-001-0709 [8]

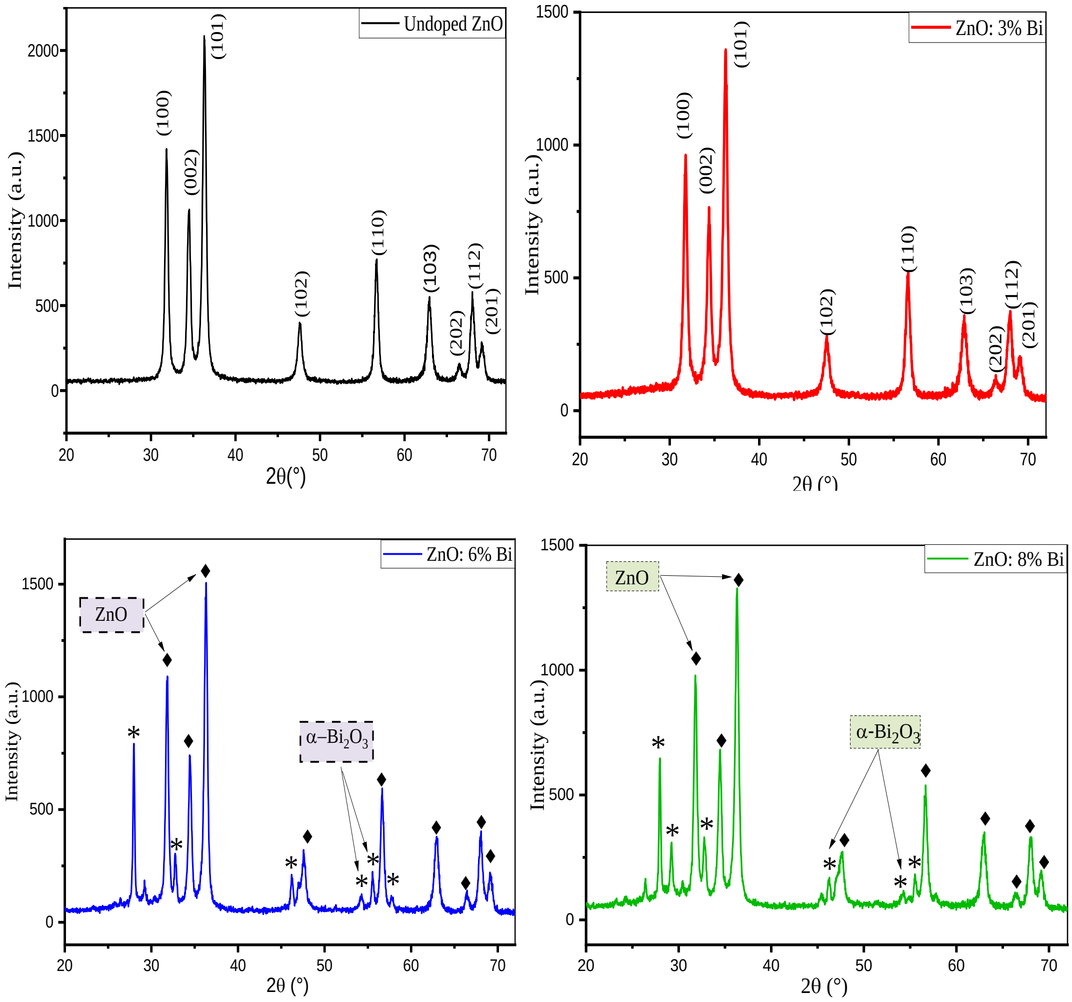

Figure III. 6: X-ray Diffraction patterns of undoped ZnO and Bismuth-doped ZnO nanopowders.

It is important to note that the presence of a secondary phase may be due to the solubility limit of bismuth in zinc oxide, as the ZnO structure can only accommodate a finite amount of this dopant. An excess of bismuth causes the production of α-Bi_2O_3 as a secondary phase [9].

The intensity of the diffraction peaks decreases as the concentration of bismuth inside the zinc oxide matrix increases, as seen in figure III. 7. The observed occurrence could be related to the replacement of bismuth (Bi) atoms, possibly caused by the migration of zinc (Zn) atoms into the interstitial regions of traditional zinc sites.

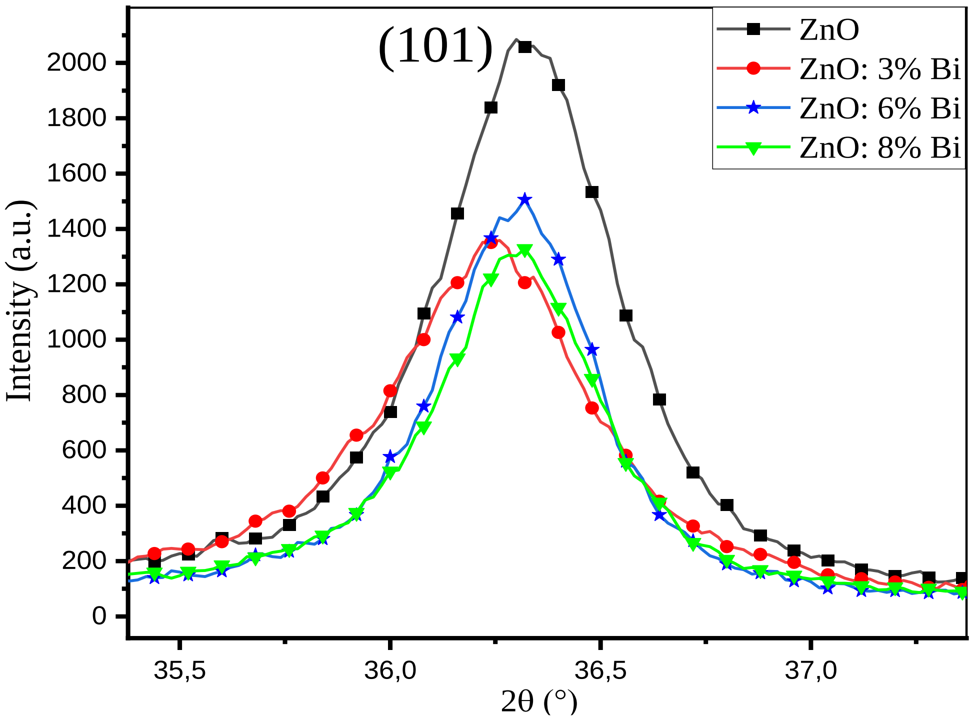

Figure III. 7: **Enlarged patterns view of pure and Bi-doped ZnO nanopowders for a variation of the (101) peak intensity.**

In the previous chapter, we discussed the procedure for determining the entire lattice strains (a, c) and the volume of the unit cell (v) for the hexagonal wurtzite structure (chapter II, equations 5 and 6). Table (III.3) displays the lattice parameters, demonstrating a direct relationship between the doping concentration and the lattice parameters 'a' and 'c' values. Specifically, an increase in doping concentration results in an elevation of these parameters. The positioning of bismuth atoms inside the ZnO matrix is a well-recognized phenomenon attributed to the dissimilar dimensions of the two atomic species. This arrangement is consistent with the larger ionic radius of bismuth (0.103 nm) compared to zinc (0.072 nm).

However, the crystallite size is crucial in establishing the scales of dimensions. The Williamson-Hall model is used to determine the average crystallite size (D) and micro strain (ε) of both pure and Bi-doped ZnO (equation 11, chapter II).

Table III.3. Characteristics of structural parameters for undoped, and Bismuth-doped ZnO nanopowders.

Sample	a(Å)	c (Å)	c/a	v(Å^3)	W-H plot		
					$D_{W\text{-}H}$ (nm)	ε (10^{-4} %)	$\delta_{w\text{-}h}$(nm^{-2})
ZnO	3,2465	5.2052	1.6033	47.5101	24.8	8.1983	0.0016141
ZnO: 3% Bi	3,2495	5.2101	1.6034	47.6427	11.65	4.8200	0.0074
ZnO: 6% Bi	3.2512	5.2098	1.6024	47.6898	18.69	2.3832	0.00286
ZnO: 8% Bi	3,2504	5.2096	1.6027	47.6645	17.793	-0.303	0.00315

The experimental samples exhibit a range of mean crystallite diameters, varying from 11.65 to 24.8 nm. All the collected samples exhibit grain and particle sizes within the nanometric dimension range. Table (III.3) shows that the pure ZnO nanopowder has a noticeably greater crystallite size of 24.8 nm. The ZnO treated with Bi exhibits a reduced average crystallite size compared to the ZnO without any doping. The addition of bismuth ions may cause a disturbance in the crystal lattice, leading to this alteration. The phenomenon can be attributed to the Zener pinning mechanism, which limits the movement of grain boundaries [10]. Figure III.8 (a) shows the W-H plot, and (b) shows the variation of average crystallite size (D), micro-strain (ε), and dislocation density (δ) as a function of dopant Ga and Bi concentration.

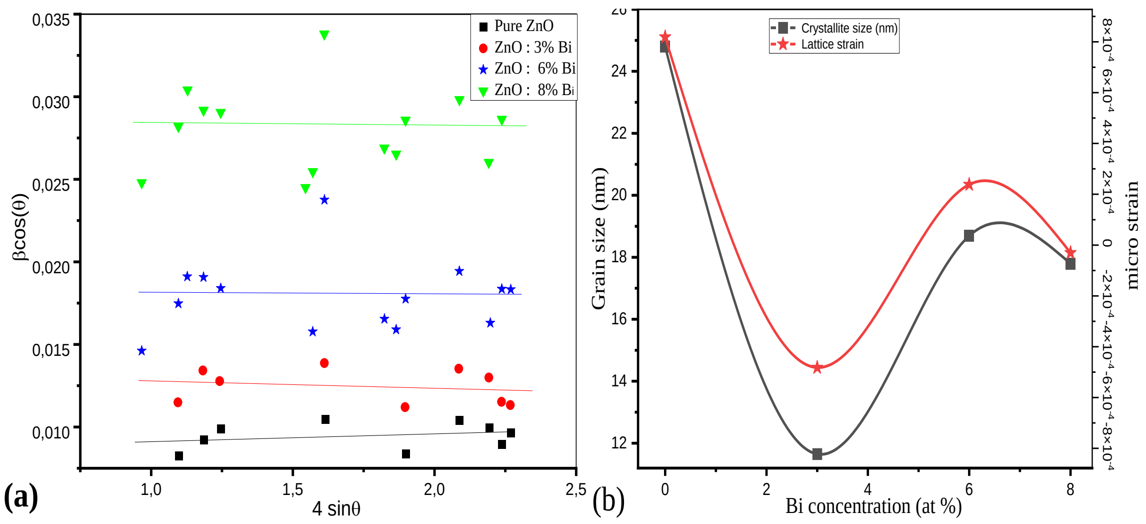

Figure III. 8: (a) Graphs of (β×cosθ) against (4×sinθ) for ZnO samples, (b) Changes in average crystallite size (D) and micro-strain (ε) across ZnO samples.

III.2.1.2. Fourier transformation infrared (FTIR-ATR) analysis

Figure III.9 shows the FTIR-ATR spectra of undoped and doped Zinc oxide nanopowder prepared by sol-gel method across the 500–4000 cm^{-1} range with varying Bi concentrations (0, 3, 6, and 8%). The infrared analysis confirms the presence of ZnO nanopowders, as previously indicated by the X-ray diffraction (DRX) results; the ZnO bond is evident in all samples, falling within the 464–500 cm^{-1} range. Notably, the ZnO bonds exhibit a shift towards higher wave numbers in all nanopowders. This observation can be attributed to the incorporation of Bi ions into the ZnO host lattice, potentially perturbing the Zn-O bonding, leading to variations in bond lengths and vibrational frequencies [11-14]. Additionally, the peaks at 3719 cm^{-1} are attributed to O-H bending vibrations. Furthermore, the peaks around 2347 cm^{-1} are associated with CO_2, which may have been absorbed from the surrounding environment [15]. A small pic associated to $(Bi)_2CO_3$ is indicated at 1353.27 cm^{-1} [16,17].

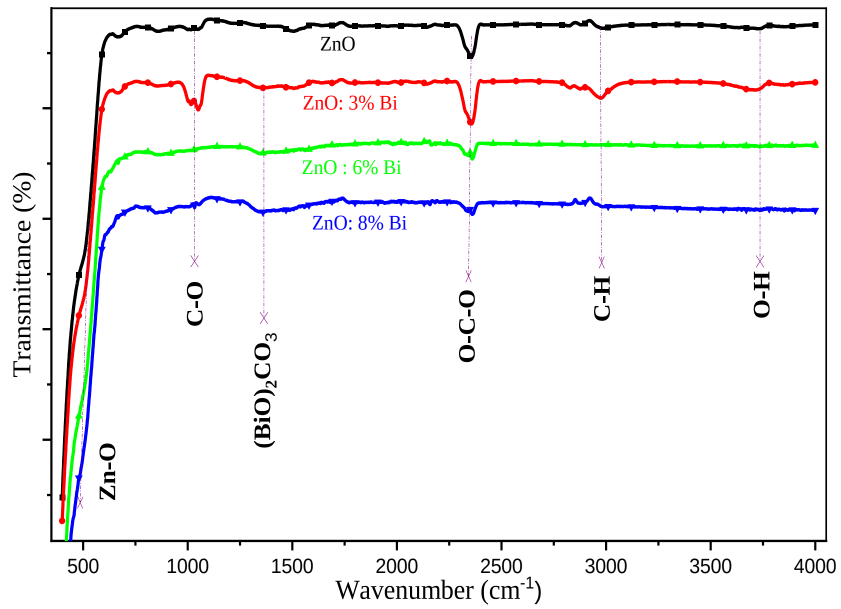

Figure III. 9: Fourier-Transform Infrared Spectroscopy (FTIR) of undoped ZnO and Bismuth-doped ZnO

III.2.2 Morphological characterization

III.2.2.1. Scanning electronic microscopy (SEM)

Scanning Electron Microscopy (SEM) is a widely used analytical tool in laboratories for assessing the physical characteristics of materials, encompassing their structure, shape, dimensions, and size distribution, particularly at micro and nanoscales. In figure III.10, SEM images of pure and Bismuth-doped Zinc oxide nanopowders with varying concentrations (0, 3, 6, and 8 %) are presented. The images reveal that the ZnO samples exhibit a granular surface morphology with spherical-shaped grains. These images demonstrate that the grain size decreases as the doping concentration rises according to its magnification, confirming that introducing bismuth as a dopant impedes the growth of ZnO grains. This trend corresponds with the alterations observed in crystallite size as determined by XRD analysis [18]. Numerous studies have corroborated the previous findings [19-21].

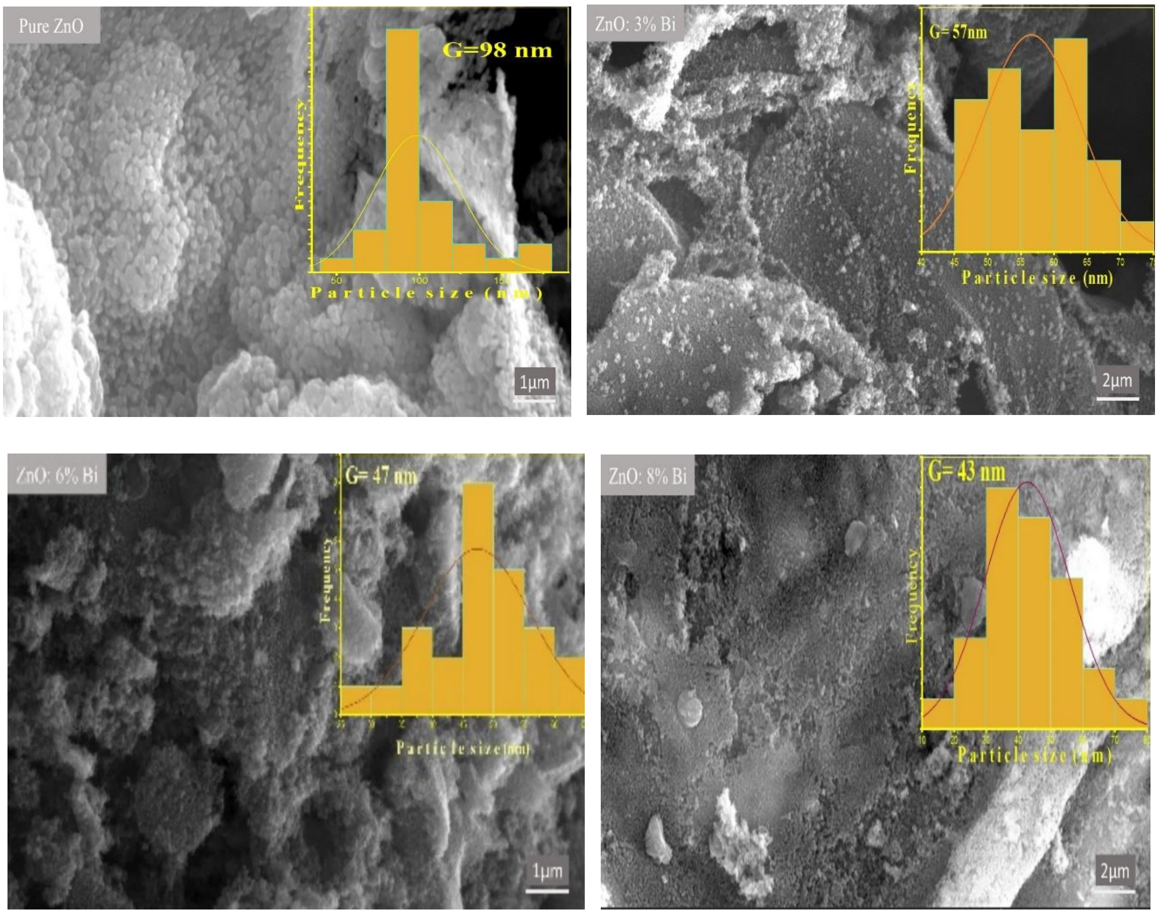

Figure III.10 : SEM images of undoped and Bismuth doped ZnO nanopowders with particle size distribution histogram.

III.2.2.2. The compositional properties

Figure III. 11 displays the energy dispersive spectrum (EDS) for undoped zinc oxide and zinc oxide doped with Bi at concentrations of 3%, 6%, and 8%. The study demonstrates that all samples contain nanoparticle compositions composed of zinc (Zn) and oxygen (O), but bismuth (Bi) is solely discovered in the doped samples. This observation verifies the effective integration of Bismuth into the ZnO nanoparticles. The weight and atomic percentage disparity between the 3 and 6 % Bi-doped samples can be ascribed to many factors affecting the EDS measurements. To begin with, particle size and shape discrepancies may impact the EDS analysis's precision. The presence of larger particles or clusters in the 3 % sample may increase the observed weight percentages. In contrast, the sample with a percentage of 6 %, which may include smaller and more evenly distributed particles, could result in lower weight percentages. Furthermore, the spatial arrangement of bismuth within the ZnO matrix may have an impact.

In the sample doped with 3 % of bismuth, the higher weight percentage suggests a more uniform dispersion of bismuth inside the nanopowder, resulting in a greater measured amount overall.

On the other hand, the sample with a percentage of 6 % may show specific areas with a reduced concentration of bismuth, leading to a decrease in the measured weight percentage [22-24]. The presence of carbon in EDS (Energy-Dispersive Spectroscopy) examination is due to the carbonaceous adhesive utilized for mounting the zinc oxide samples. In this case, the carbon in the adhesive strip can interact with the electron beam that is being used.

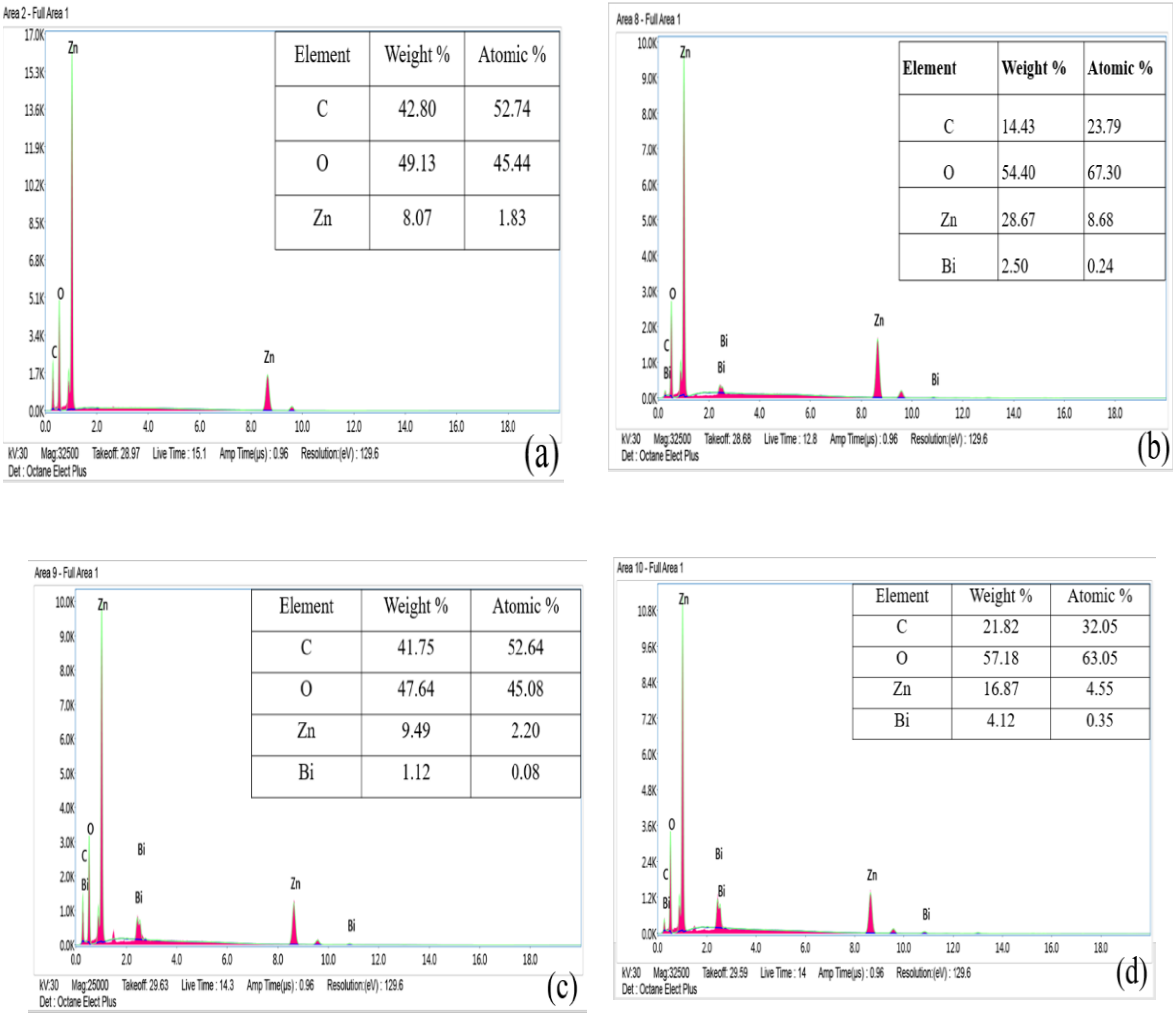

(a)

Element	Weight %	Atomic %
C	42.80	52.74
O	49.13	45.44
Zn	8.07	1.83

(b)

Element	Weight %	Atomic %
C	14.43	23.79
O	54.40	67.30
Zn	28.67	8.68
Bi	2.50	0.24

(c)

Element	Weight %	Atomic %
C	41.75	52.64
O	47.64	45.08
Zn	9.49	2.20
Bi	1.12	0.08

(d)

Element	Weight %	Atomic %
C	21.82	32.05
O	57.18	63.05
Zn	16.87	4.55
Bi	4.12	0.35

Figure III.11: EDS spectra of ZnO samples: (a) Pure ZnO, (b) ZnO: 3% Bi, (c) ZnO: 6% Bi, and (d) ZnO: 8 % Bi.

III.2.3. Optical characteristics

III.2.3.1. UV-visible absorption

UV-visible is a powerful procedure for investigating the optical properties of semiconducting nanoparticles. Figure III. 12 depicts the UV-Vis absorption spectra of undoped and different Bi concentrations of doped ZnO nanopowders. Typically, the measured absorbance is influenced by factors such as oxygen deficit, defect centers, and band gap. Within this study, we have discovered prominent absorption peaks that appear between the wavelengths of 319 to 338 nm. These peaks are specifically associated with the characteristic ZnO band gap. The introduction of Bi doping causes a little shift of the absorption edge towards higher wavelengths, resulting in a narrowing of the band gap.

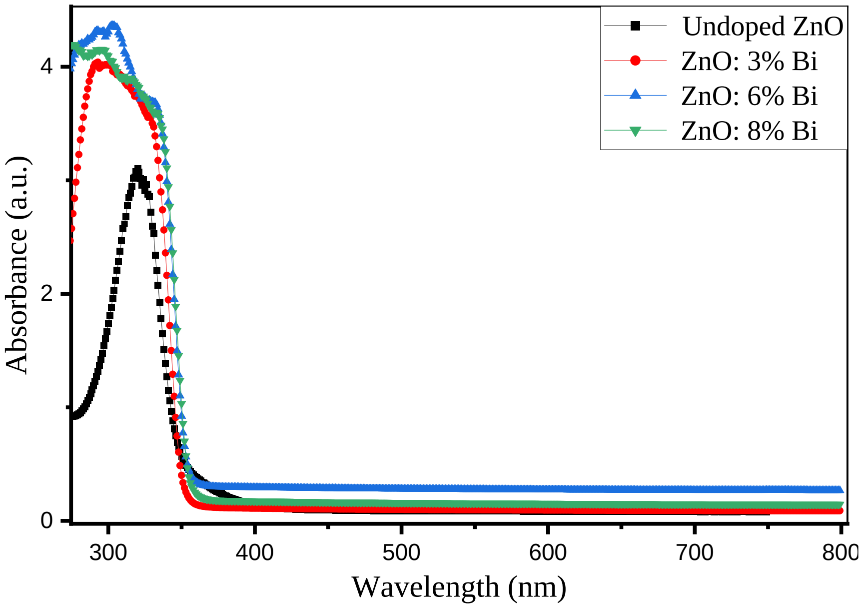

Figure III. 12: Absorption spectra of ZnO: Bi nanopowders.

- **Gap energy**

Figure III. 13 exhibits Tauc's plots for all nanopowders. The data presented in Table III. 4 clearly demonstrates that the optical band gap of undoped ZnO nanopowder was measured to be 3.63 eV. As the concentration of Bi rises (3, 6, and 8 %), there is a corresponding drop in the gap energy to lower values (3.55, 3.53, and 3.51 eV) [8]. The observed decrease in size is likely attributed to an increased concentration of structural defects, imperfections, or impurity states, as evaluated by the use of X-ray diffraction (XRD) analysis [25,26].

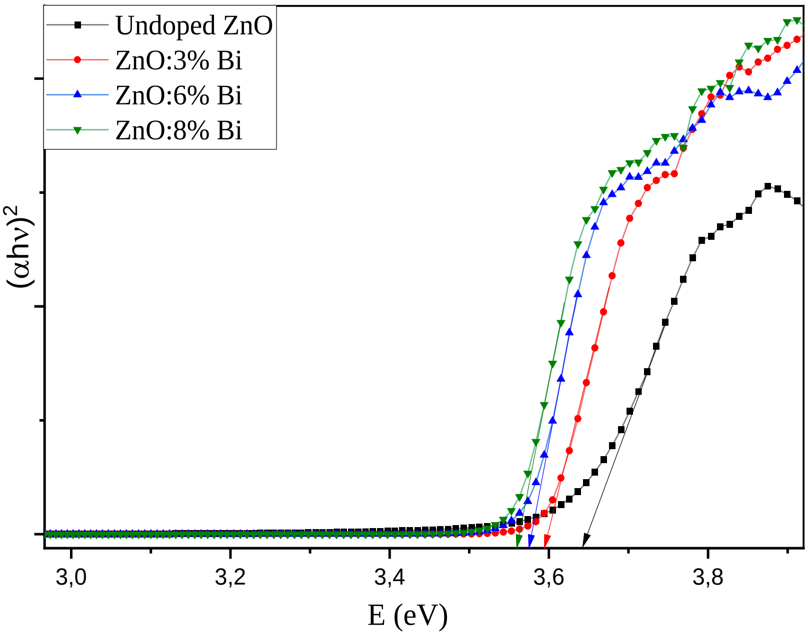

Figure III. 13: Variation of $(\alpha h\nu)^2$ with photon energy $(h\nu)$ for undoped and Bi-doped

This decrease is likely due to the Bi atoms creating new energy levels within the original gap. Researchers believe that the interaction between Bi's localized d-electrons and the nanoparticles' electrons (sp-d exchange interaction) plays a role in narrowing the band gap, especially for Bi concentrations of 3%, 6%, and 8% [27].

Table III.4. Energy band gap Data for undoped and bismuth-doped ZnO.

Bi (%)	**Eg (eV)**
0	3.63
3	3.55
6	3.53
8	3.51

Part III

Zinc oxide doped with Gallium.

Introduction

In addition to studying zinc oxide undoped and doped with bismuth atoms, we have studied the impact of gallium doping on the structural, morphological, and optical characteristics of zinc oxide powder generated using the sol-gel technique. As previously, we have utilized X-ray diffraction (XRD), scanning electron microscopy (SEM), UV-Visible spectroscopy (UV-Vis), and Fourier-transform infrared (FTIR) spectroscopy to investigate these features.

III.3.1 Structural characterization

III.3.1.1 X-ray diffraction

Figure III.14 illustrates the XRD patterns of Zinc oxide samples that have been doped with different amounts of gallium (3%, 6%, and 8%) compared to the XRD pattern of undoped ZnO. All the diffraction peaks are well matched with hexagonal wurtzite structure. Based on the JCPDS data No. 00-036-1451 [7], no further peaks related to Ga or Ga_2O_3 atoms were found.

Figure III.15 shows a variation in the intensity of the peak corresponding to the preferred orientation (101). The ZnO sample doped with 3% Ga showed the highest intensity due to the enhancement of zinc oxide crystallization by gallium atoms. ZnO samples doped with 6% and 8% Ga exhibited a decrease in peak intensity compared to the undoped sample [28]. The decrease in intensity at 6% and 8% Ga doping concentration is due to the inhibition of zinc oxide crystallization by gallium atoms, which is caused by defects in the crystal lattice structure [29]. On the other hand, a decrease in the value of the 2θ angle of the preferred orientation peak was observed with an increase in the doping concentration this can be explained by the fact that Ga^{3+} ions are successfully incorporated into the ZnO lattice and because the radius of Ga^{+3} ions (0.062 nm) is smaller than the Zn^{+2} ions radius (0.074 nm) [30].

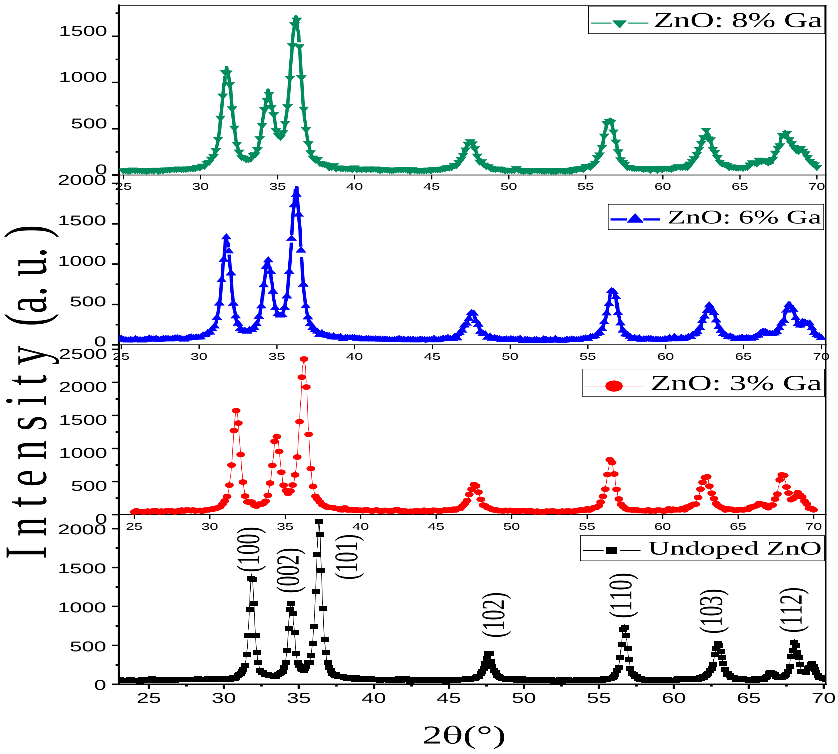

Figure III. 14: X-ray diffraction patterns of Ga-doped ZnO nanopowders.

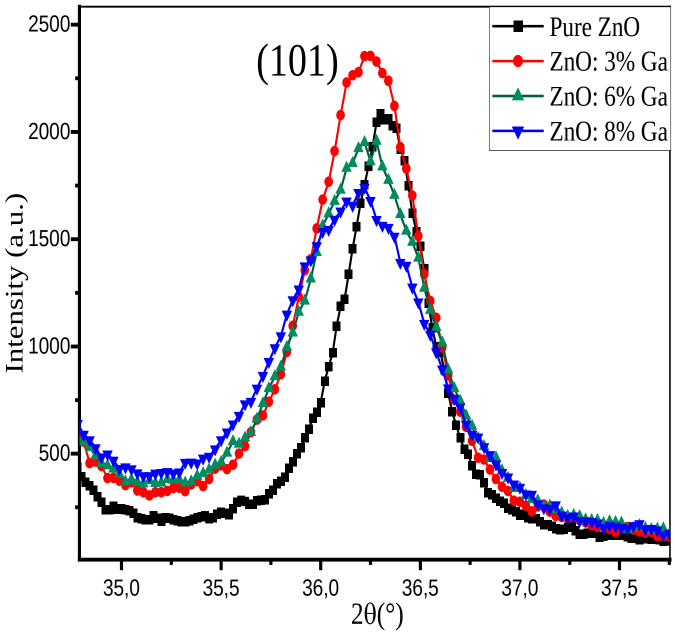

Figure III.15: Enlarged patterns view of Ga- doped ZnO nanopowders,Variation of the intensity and width of (101) peak.

The values of the structural parameter are displayed in table (III.5). The doping level has an impact on parameters ‘a’ and ‘c.’ The expansion of lattice parameters can be elucidated by including Ga^{3+} ions into the interstitial spaces [31-33].

Table III.5. Structural parameters of undoped, and Ga-doped ZnO nanopowders.

Sample	a (Å)	c (Å)	c/a	V ($Å^3$)	W-H model		
					D (nm)	$\varepsilon(\times 10^{-4})$	$\delta(\times 10^{-3}\ nm^{-2})$
Undoped ZnO	3,246	5.205	1.603	47.51	24.8	8.1983	1.6141
ZnO : 3% Ga	3.252	5.211	1.602	47.75	17.2	7.6788	3.3723
ZnO : 6% Ga	3.253	5.207	1.601	47.73	13.2	-1.8748	5.6873
ZnO : 8% Ga	3.251	5.212	1.603	47.71	9.09	-6.9157	12.089

The average crystallite sizes of Ga doped ZnO samples are variated between 9.09–24.8 nm. The average crystallite size decreases with Ga concentration increases. This phenomenon can be attributed to the Zener pinning effect, which hinders the movement of grain boundaries. Additionally, defects in the crystal matrix function as a restraining force, causing a delay in the formation of crystallites. The increase in Ga concentration in the ZnO matrix causes it to be situated in the Zn and O vacancies as well as interstitial sites, acting as defects and preventing crystallite synthesis [34]. In addition, Jia Lui and Weijia Zhang reported that the higher doping concentration results in more crystal grains that are smaller because the Ga^{3+} ion serves as the crystallization nucleus [35]. On the other hand, analysis of the relationship between strain (ε) and dislocation (δ), Table (III.5), reveals that all doped samples have lower ε values than the undoped ZnO sample. The result confirms the enhancement of crystalline quality. Figure III.16 (a) shows the W-H plot, and (b) shows the variation of average crystallite size (D), micro-strain (ε), and dislocation density (δ) as a function of dopant Ga concentration.

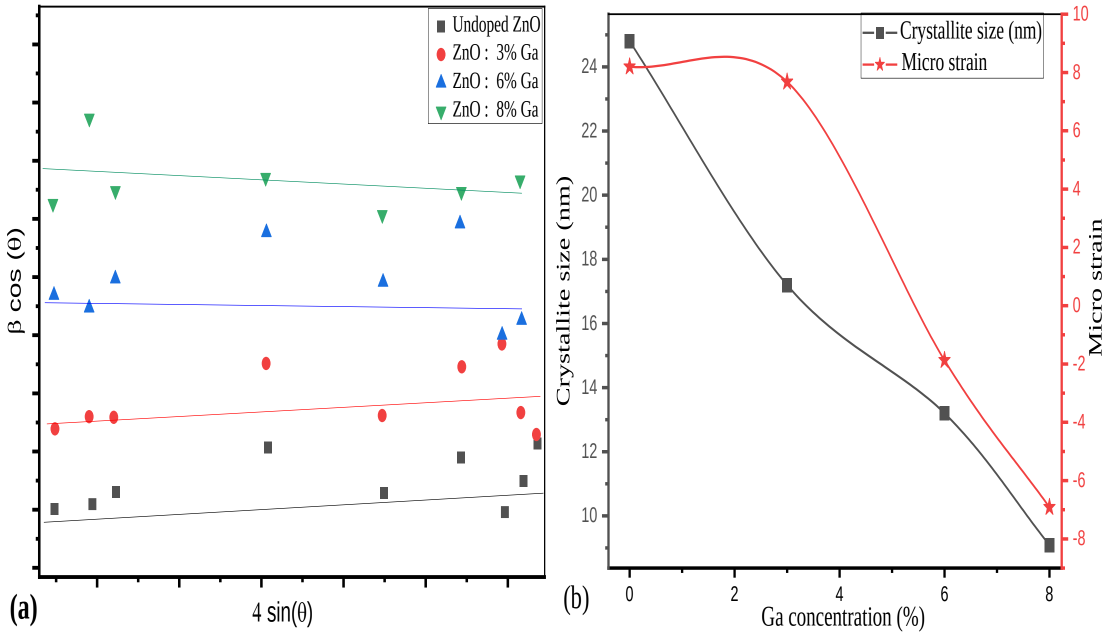

Figure III. 16: (a) plots of βcosθ versus 4sinθ of Ga doped ZnO samples, (b) Variations of average crystallite size (D), dislocation density (δ) and micro-strain (ε) as a function of Ga doped ZnO samples.

III.3.1.2. Fourier transformation infrared (FTIR-ATR) analysis

Figure III.17 illustrates the FTIR-ATR spectra of the doped ZnO nanopowder in the range 500–4000 cm^{-1} with different concentrations of Ga (0, 3, 6, and 8%). The infrared analysis confirms the formation of the ZnO nanopowders, as the DRX shows; the ZnO bond appeared in all samples, in the range of 400–537cm^{-1}. The ZnO bonds shift toward the higher wave number side in all nanopowders. This result can be explained by the incorporation of Ga ions in the ZnO host lattice, and Zn-O bonding can be perturbed, resulting in a difference in bond lengths and a change in the vibrational frequency [31-37]. In addition, the peaks observed at 1522 cm^{-1} is attributed to H-O-H - bending vibrations, which are assigned to a small quantity of H_2O in the ZnO nanocrystal [38]. On the other hand, the observed peaks around 2340 cm^{-1} are related to CO_2, which might be absorbed from the environment.

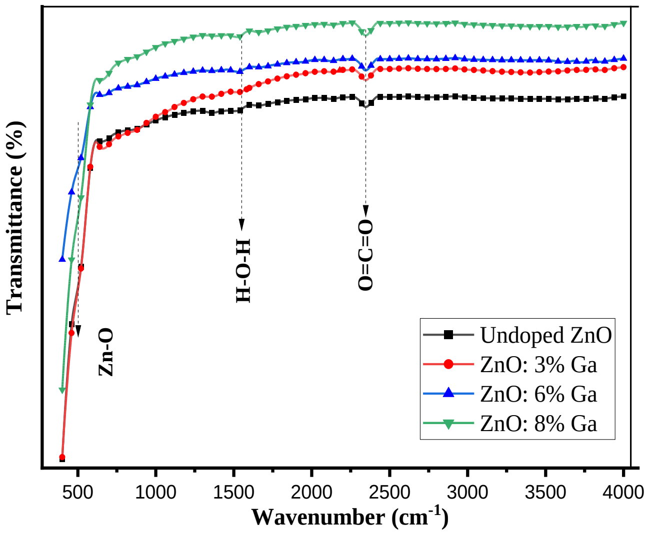

Figure III. 17: FTIR-ATR spectra of Ga-doped ZnO nanopowders.

III.3.2. Morphological characterization

III.3.2.1. Scanning electronic microscope

he morphological properties of Ga-doped ZnO nanopowders with varied concentrations (3%, 6%, and 8%) are shown in figure III. 18. These samples have a consistent spherical shape, and there is a distinct and significant reduction in grain size as the concentration of the dopant increases. The histogram results in figure III.18 confirm the decrease on particle size from undoped zinc oxide samples to those doped with 3% gallium. We couldn't utilize this measurement for zinc oxide samples doped with 6% and 8% Ga because of the small grain size (less than 50 nm) compared to the image magnification (1µm). The XRD measurements support this observation.

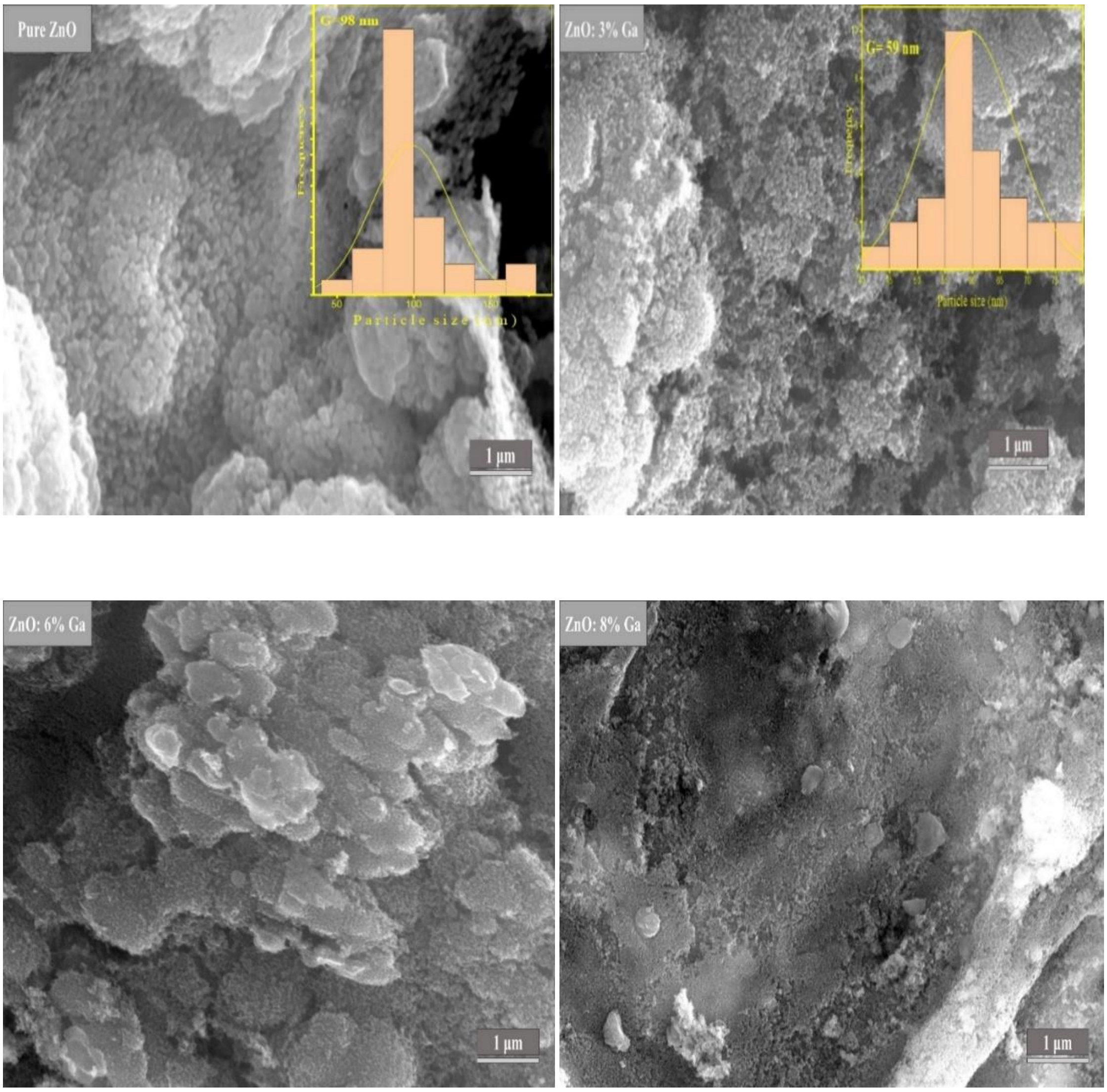

Figure III. 18: SEM images of undoped and Gallium doped ZnO nanopowders with particle size distribution histogram for both of undoped and ZnO: 3% Ga.

III.3.2.2. Compositional properties

Figure III.19 presents the energy-dispersive X-ray spectroscopy (EDS) analysis of pure and Ga doped ZnO nanopowders with different concentrations (3%, 6%, and 8%). The spectra confirm that all samples primarily comprise Zn and O, consistent with their expected nanoparticle compositions. Notably, the Ga peak is only present in the doped samples, confirming the successful incorporation of Ga into the ZnO lattice [33].

As explained in the second Axis, the variation in weight and atomic percentages can be attributed to the random distribution of dopants. Additionally, the shape and size of the particles also control this variation.

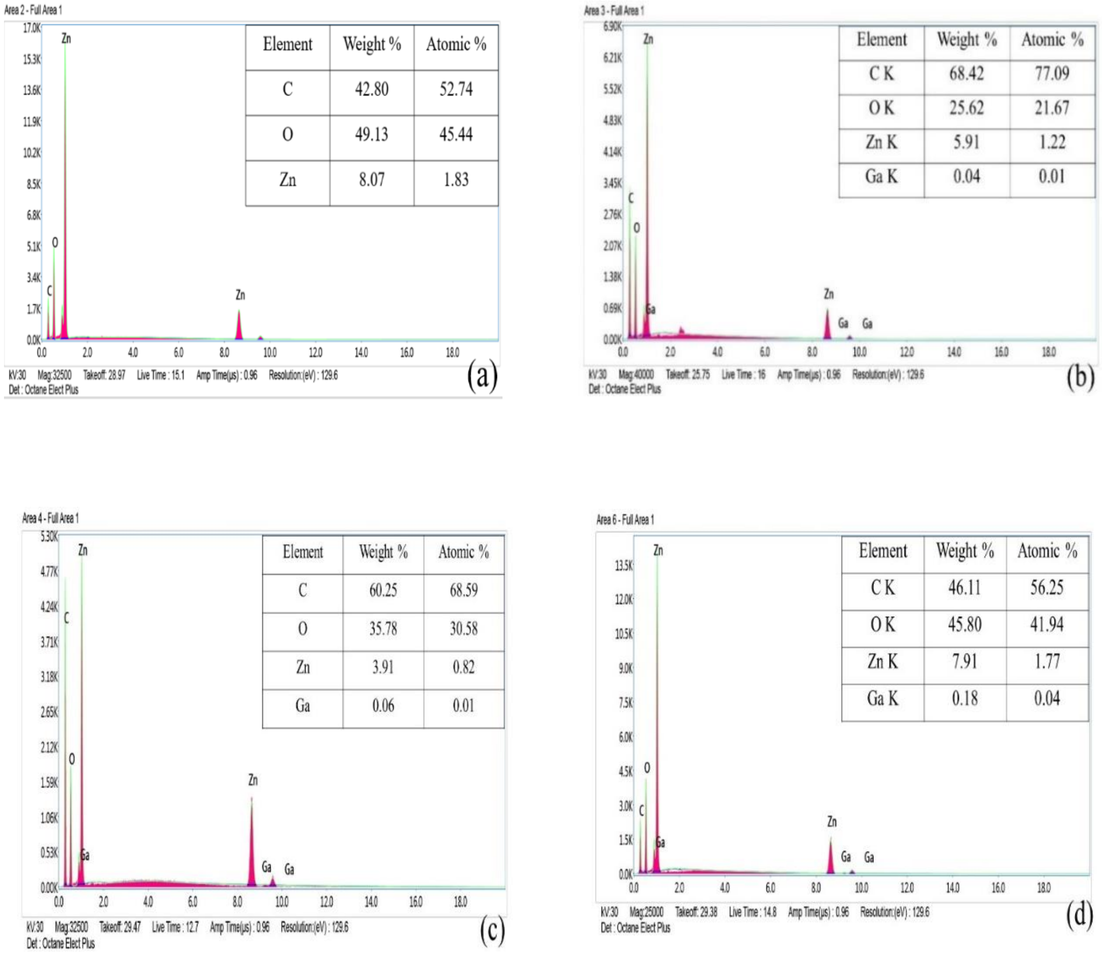

Element	Weight %	Atomic %
C	42.80	52.74
O	49.13	45.44
Zn	8.07	1.83

Element	Weight %	Atomic %
C K	68.42	77.09
O K	25.62	21.67
Zn K	5.91	1.22
Ga K	0.04	0.01

Element	Weight %	Atomic %
C	60.25	68.59
O	35.78	30.58
Zn	3.91	0.82
Ga	0.06	0.01

Element	Weight %	Atomic %
C K	46.11	56.25
O K	45.80	41.94
Zn K	7.91	1.77
Ga K	0.18	0.04

Figure III.19: EDS spectra of ZnO samples: (a) Undoped ZnO, (b) ZnO: 3% Ga, (c) ZnO: 6 % Ga, and (d) ZnO: 8 % Ga.

III.3.3. Optical characteristics

III.3.3.1. UV-visible absorption

Figure III. 20 shows the UV-Vis absorption spectra of ZnO nanopowders with various concentrations of Ga doping. Strong absorption peaks appear between 280 and 320 nm, representing the characteristic band of ZnO. Gallium doping causes a slight shift of the absorption edge towards shorter wavelengths, leading to an increase in the band gap.

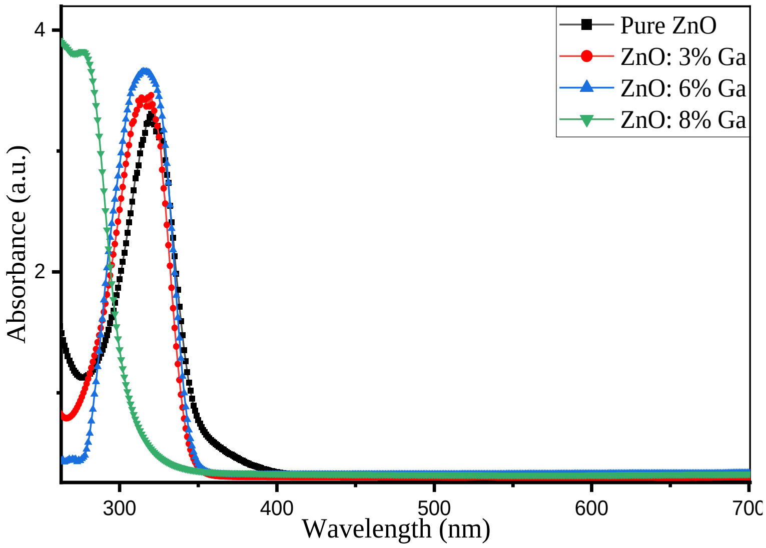

Figure III.20: UV absorbance spectra of undoped and Ga doped ZnO nanoparticles.

Figure III. 21 displays Tauc's plots for all samples. The data in table (III.6) shows that the optical band gap of undoped ZnO nanopowder is 3.63 eV. Increasing the concentration of Ga (3%, 6%, and 8 %) results in a shift in the bandgap energy to higher levels. These results may be due to the increase in the density of charge carriers, as explained by the Burstein-Moss effect,

As the Ga dopant atoms introduce additional electrons into the ZnO lattice, these electrons fill up lower-lying energy states within the conduction band. Consequentially, the energy required to excite an electron from the valence band to the conduction band increases, effectively widening the band gap [39].

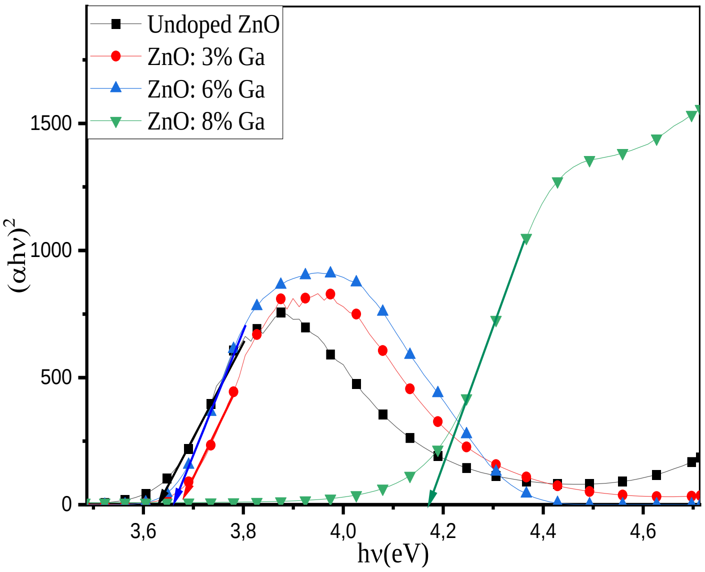

Figure III. 21: Variation of $(\alpha h\nu)^2$ with photon energy (hν) for Ga-doped ZnO nanopowders.

Table III.6. Optical gap energy of ZnO samples with different Ga concentrations.

Ga (%)	Eg (eV)
0	**3.63**
3	**3.68**
6	**3.66**
8	**4.15**

Part IV

Bi and Ga co-doping ZnO nanopowders.

Introduction

This part is dedicated to a thorough investigation of the impact of dual dopant including gallium and bismuth on zinc oxide powder's structural, morphological, and optical properties. The established formula for the chemical synthesis was: ZnO: x% Ga- y% Bi, here (x; y)= (0;0), (3; 3), (3; 5), (5; 3), and (5; 5) and for each individual systeme (pure and co-doped) the chemical formula and named samples were: ZGBO 00 (Undoped ZnO), ZGBO 33 (ZnO: 3% Ga- 3% Bi), ZGBO 35 (ZnO: 3% Ga- 5% Bi), ZGBO 53 (ZnO: 5% Ga- 3% Bi), and ZGBO 55 (ZnO: 5% Ga- 5% Bi).

III.4.1. Structural characterisation

III.4.1.1 X-ray diffraction

Compared to the data from ASTM fiche with the JCPDS data No. 00-036-1451[7], our x-ray diffraction spectra for pure and Ga; Bi co-doped ZnO nanopowders (figure III.22) show that they are always in hexagonal wurtzite structure form. Additional peaks, marked with an asterisk, appear clearly along with ZnO phase for ZGB35 sample. According to the explanation provided in the first axis. They agree with the main diffraction planes of the α-Bi_2O_3 monoclinic structure (JCPD, No. 76-1730) [8].

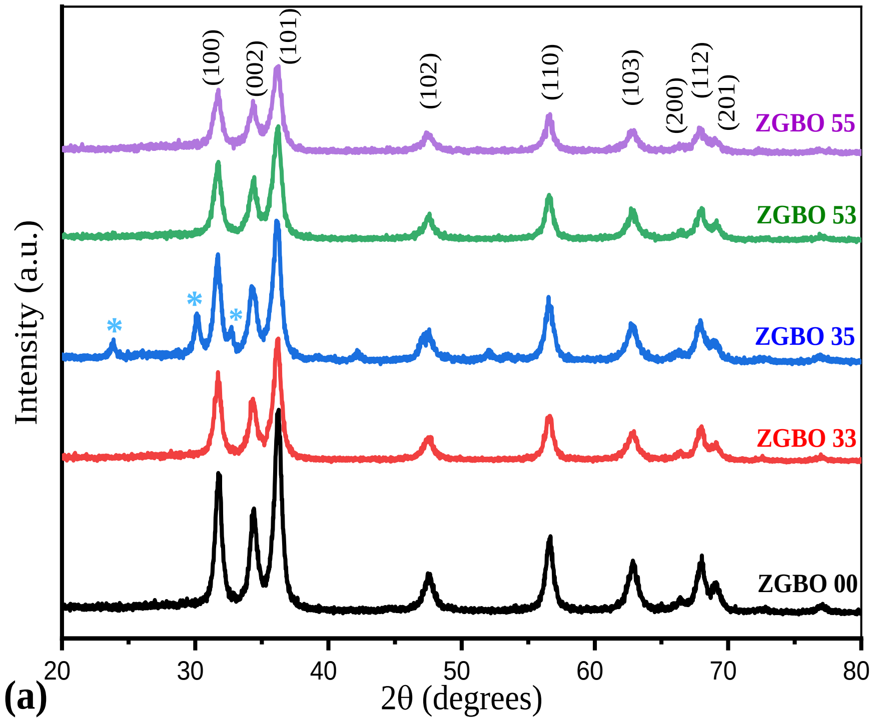

Figure III. 22: X-ray diffraction patterns of Ga and Bi co-doped ZnO nanopowders.

Through the Figure III.23. We notice that the increase in the dopant concentration leads to decrease in the intensity peak of the preferred orientation (101), suggesting that dual Bi^{+3} and Ga^{+3} co-doping inhibited the development of crystallite size.

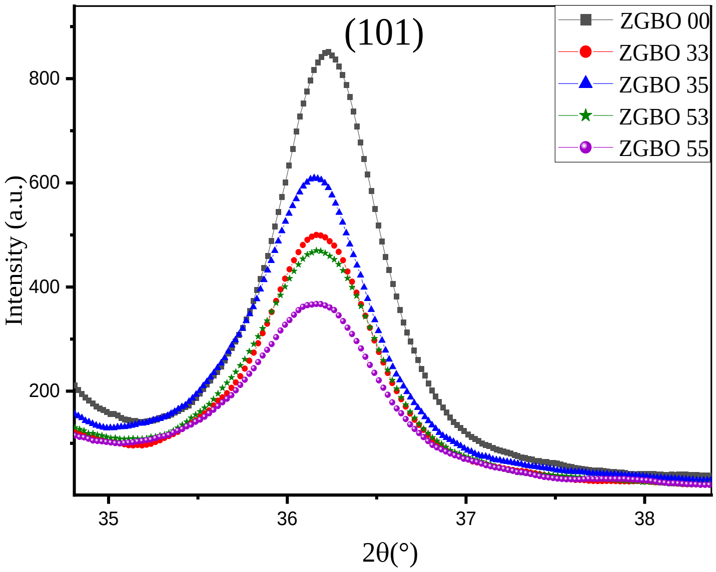

Figure III.23: Enlarged patterns view of Ga and Bi co-doped ZnO nanopowders, Variation of the intensity and width of (101) peak.

The lattice parameters a, c, and v of ZGBO powders are displayed in table III.7. The difference in the ionic radius of Bi^{+3} and Ga^{+3} concerning Zn^{+2} gives the variation of the lattice constants. For undoped ZnO nanopowders, the lattice parameters ‘a’ and ‘c’ are estimated to be 3.24 Å and 5.20 Å, respectively. The substitution of Bi^{+3} and Ga^{+3} ions in place of Zn^{+2} ions increase the lattice constants ‘a’ and ‘c’. The unit cell volume of ZnO also increases with the substitution of Ga and Bi atoms [3]. The estimated values are 47.51, 48.47, 48.23, 48.20, and 48.24 Å^3 for ZGBO 00, ZGBO 33, ZGBO 35, ZGBO 53, and ZGBO 55, respectively. This indicates that the dopant ions reside partially in tetrahedral Zn positions. The crystallite size is calculated using the W-H plot (figure III.24.a), and its results tabulated in table (III.7) initially decrease with the doping level. Varying from 24.8 nm in ZGBO 00 sample to 10.62 nm in ZGBO 53. This evolution can be due to the disorder created in the crystal lattice by incorporating the Bi ions [15]**.** Micro-strain results represent the stretching or compression in the W-H plot, and its results tabulated in table (III.7) initially decrease with the e sample during the incorporation of gallium and bismuth atoms .We observed a decrease in the crystal size from 24.8 nm in the undoped ZnO sample to 12.73 nm in the ZGBO 33 sample. This decrease is associated with a compression represented by the negative value, which changes the strain value from 8.19 to (-5.79). On the other hand, in the ZGBO 35 sample, the crystal size increased, resulting in a stretching process represented by the value 32.1 in the micro-strain result. Figure III.24.b shows the variation of average crystallite size (D), micro-strain (ε), and dislocation density (δ) as a function of dopant Ga and Bi concentration.

TableIII.7. Structural parameters of ZGBO nanopowders.

Sample	a=b (Å)	c (Å)	c/a	V ($Å^3$)	W-H model		
					D (nm)	ε (x 10^{-4})	δ (nm^{-2})
ZGBO 00	3,2465	5.2052	1.6033	47.5101	24.8	8.19	0.0016
ZGBO 33	3.2695	5.2368	1.6017	48.4796	12.73	-5.79	0.0061
ZGBO 35	3.26403	5.2276	1.6015	48.2326	24.09	32.1	0.0017
ZGBO 53	3.26455	5.22305	1.6017	48.20604	10.62	-15.8	0.0088
ZGBO 55	3.26554	5.2234	1.5995	48.23851	11.83	0.67	0.0071

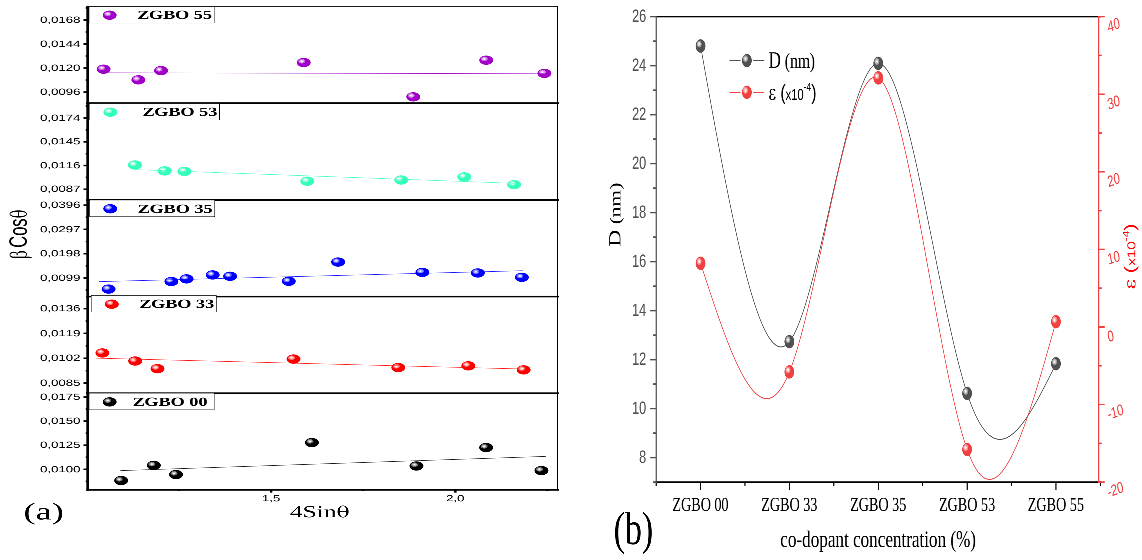

Figure III. 24: (a) plots of βcosθ versus 4sinθ of ZGBO samples, (b) Variations of average crystallite size (D), dislocation density (δ) and micro-strain (ε) as a function of ZGBO samples.

III.4.3.2 Fourier transformation infrared (FTIR) analysis

Figure III.25 represent the FTIR spectrum of the co-doped ZnO nanopowder with different concentration of Bi and Ga. The bands between 430 and 495 cm^{-1} are due to the stretching mode of ZnO vibration for all samples[36]. The peaks at 2300 cm^{-1}, and 1361 cm^{-1} correspond to, O-C-O[19], and $(BiO)_2CO_3$ [16], respectively**.** The FT-IR analysis confirms the previous DRX results, showing that the good incorporation of gallium atoms within the zinc oxide structure reduces the appearance of any molecular vibrations. On the other hand, bismuth atoms form a new phase, forming stronger detectable bonds. These results were also confirmed in the second axis.

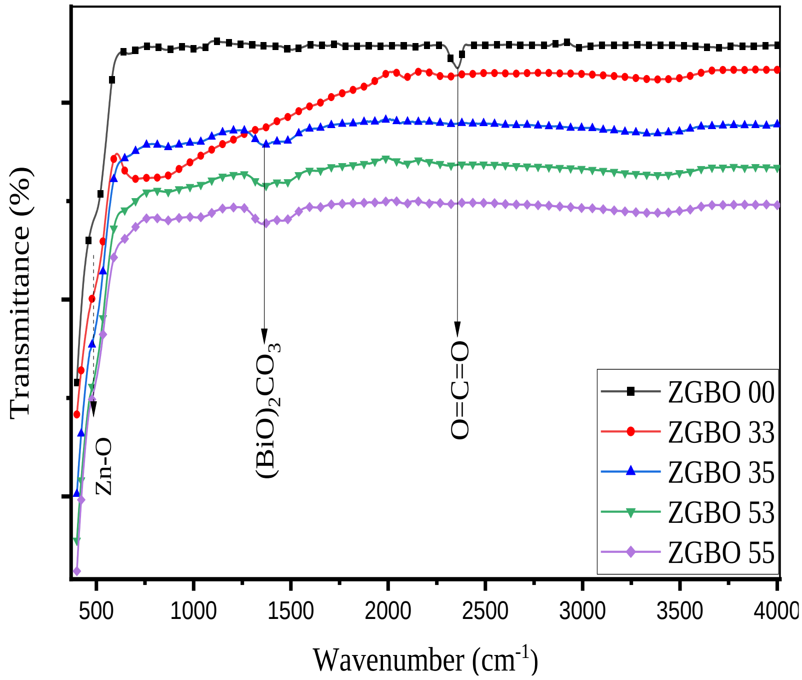

Figure III. 25: FT-IR spectra of ZGBO nanopowder.

III.4.2. Morphological characterization

III.4.2.1. Scanning electronic microscope

The morphological properties of ZnO co-doped with different concentrations of Ga and Bi were imaged using a scanning electronic microscope (SEM) at a magnification of 400 nm (figure III. 26). All samples have a consistent spherical shape. The histogram is also presented. The average grain size ranged from 72 nm for the ZGBO 00 sample to 47 nm for ZGBO 53. Ga and Bi doping led to a reduction in the size of ZnO grains While increasing the Bi concentration from 3% to 5% results in slight increase in grain size.

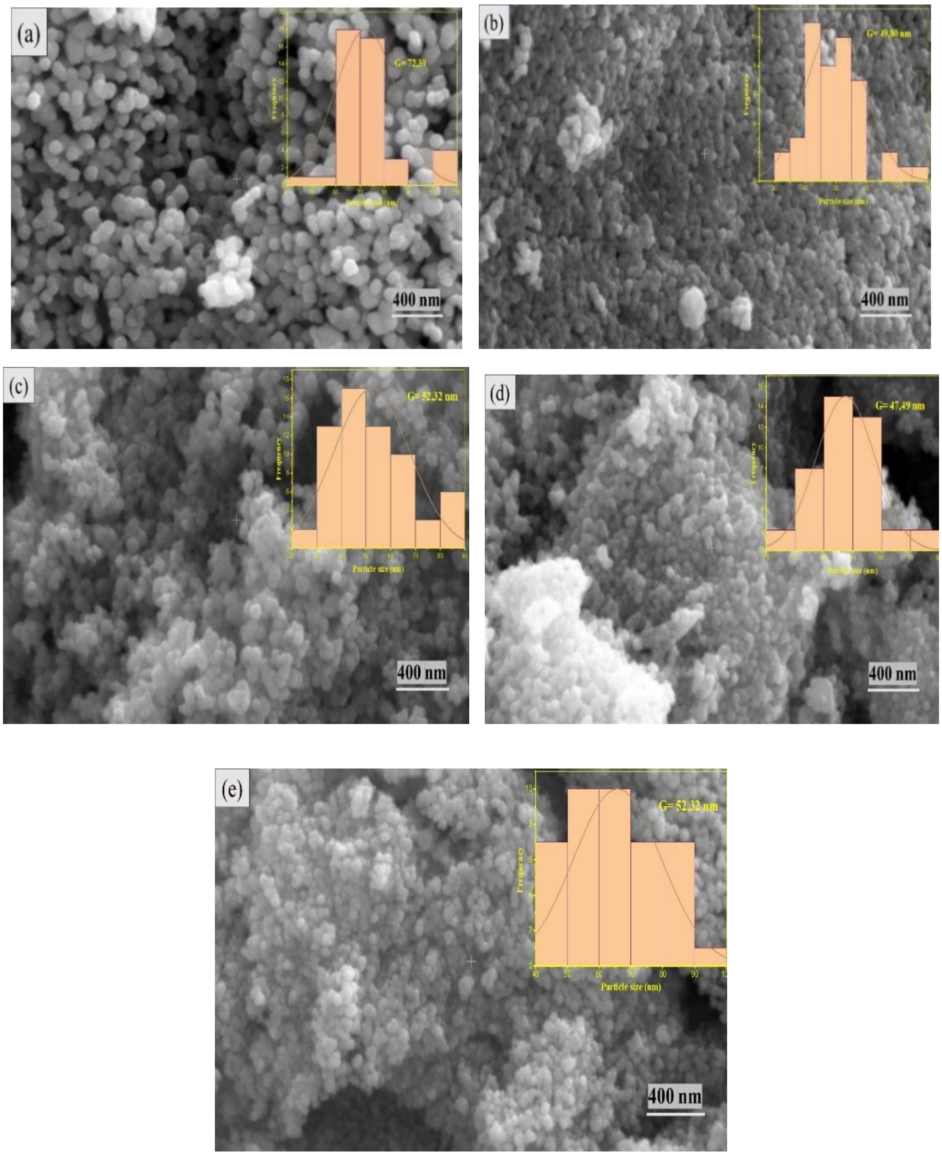

Figure III. 26: SEM images with particle size distribution histogram of ZGBO nanopowders.

III.4.2.2. Compositional properties

The EDS spectra of ZnO co-doped with Bi and Ga nanopowders are reported in figure III.27 the EDS study confirms the presence of Zn and O in all samples in high proportion, both gallium and bismuth elements were found in the co-doped samples, with their concentrations varying based on their respective amounts in the sample. The additional phase formed in X-ray diffraction results explains the higher appearance of bismuth compared to gallium. This is attributed to bismuth's higher atomic number (83) compared to gallium (31), which enhances electron interaction with bismuth atoms, resulting in stronger EDS signals.

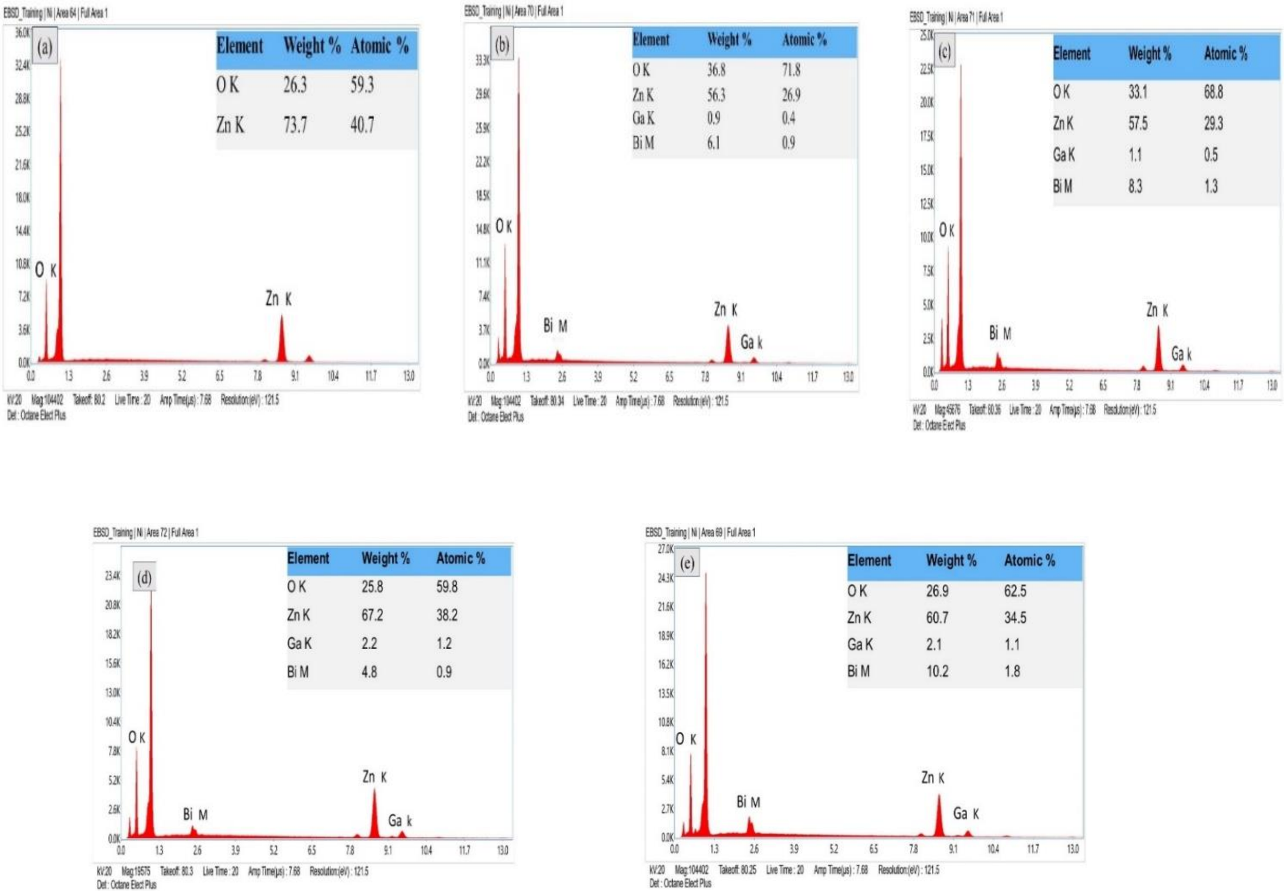

(a)

Element	Weight %	Atomic %
O K	26.3	59.3
Zn K	73.7	40.7

(b)

Element	Weight %	Atomic %
O K	36.8	71.8
Zn K	56.3	26.9
Ga K	0.9	0.4
Bi M	6.1	0.9

(c)

Element	Weight %	Atomic %
O K	33.1	68.8
Zn K	57.5	29.3
Ga K	1.1	0.5
Bi M	8.3	1.3

(d)

Element	Weight %	Atomic %
O K	25.8	59.8
Zn K	67.2	38.2
Ga K	2.2	1.2
Bi M	4.8	0.9

(e)

Element	Weight %	Atomic %
O K	26.9	62.5
Zn K	60.7	34.5
Ga K	2.1	1.1
Bi M	10.2	1.8

Figure III.27: EDS spectra of ZGBO nanopowders samples with; (a): Undoped ZnO, (b): ZGBO 33, (c): ZGBO 35, (d): ZGBO 53, (e): ZGBO 55.

III.4.3. Optical characteristics

III.4.3.1. UV-visible absorption

UV-Vis analyses were performed on zinc oxide powder doped with different amounts of gallium and bismuth. This work examines the impact of doping on the optical absorption characteristics of zinc oxide. Figure III.28 displays the UV-visible absorption data of ZGBO samples, indicating that the absorption edge for all samples ranges within the region of 320 to 345 nm. An increase in doping concentration leads to a higher absorption edge. The rise could be due to a reduction in the energy gap of zinc oxide, possibly caused by the formation of new energy levels inside it due to doping particle integration. Tauc plot confirmed the previous interpretation by demonstrating an actual reduction in the band gap energy of ZnO as the doping concentration increased, as indicated in Figure III. 29 and table (III.8) [25].

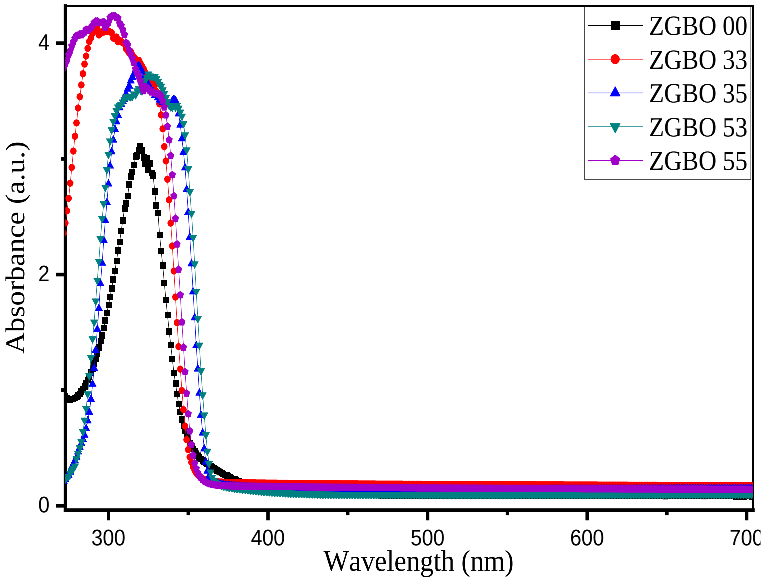

Figure III.28: UV absorbance spectra of ZGBO nanopowders.

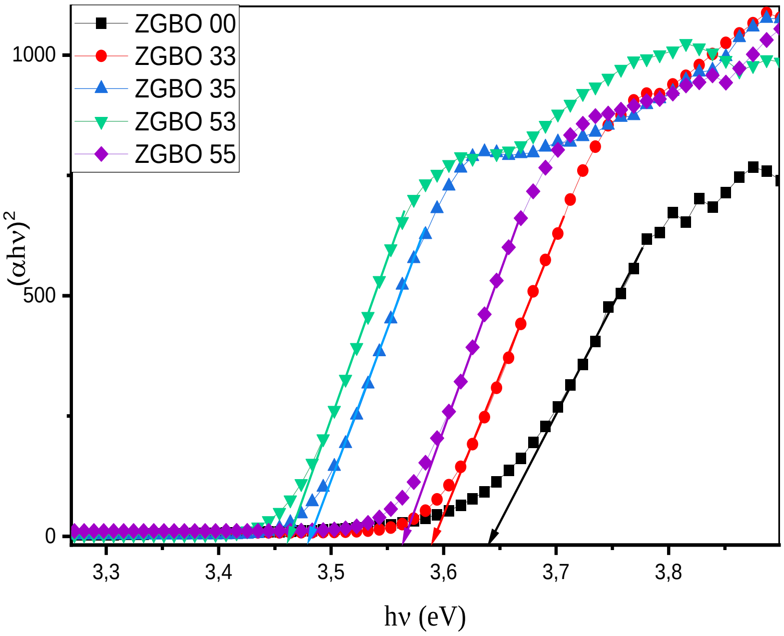

Figure III. 29: Variation of $(\alpha h\nu)^2$ with photon energy (hν) for Bi and Ga co-doped ZnO nanopowders.

Table III.8. Optical gap energy of ZnO samples with different Bi and Ga concentrations.

Sample	Eg (eV)
ZGBO 00	3.63
ZGBO 33	3.58
ZGBO 35	3.47
ZGBO 53	3.46
ZGBO 55	3.56

References

References

[1] E. A. S. Dimapilis, C. S. Hsu, R. M. O. Mendoza, and M. C. Lu, “Zinc oxide nanoparticles for water disinfection,” Sustainable Environment Research, vol. 28, no. 2, pp. 47–56, 2018, doi: 10.1016/j.serj.2017.10.001.

[2] A. Šulčiute, S. Ostachavičiute, and E. Valatka, “Synthesis, structure and photoelectrochemical behaviour of ZnO coatings on AISI 304 type steel,” Chemija, vol. 28, no. 2, pp. 85–92, 2017.

[3] G. Vijayaprasath, G. Ravi, R. Venkatesh, K. Ramachandran, A. Mani, and J. Judith Vijaya, “Structural characterization and magnetic properties of Co co-doped Ni/ZnO nanoparticles,” Appl Phys A Mater Sci Process, vol. 122, no. 2, pp. 1–11, Feb. 2016, doi: 10.1007/s00339-016-9655-0.

[4] J. Zhang, & D. P. Kamdem, “FTIR characterization of copper ethanolamine—wood interaction for wood preservation,” Holz Forschung, vol. 54, no. 2, pp. 119-122, 2000 doi: 10.1515/HF.2000.020

[5] E. M. Abdelrazek, A. M. Abdelghany, & A. E. Tarabih, “Characterization and physical properties of silver/PVA nano-composite.” Research Journal of Pharmaceutical, Biological and Chemical Sciences, 3(4), 448. 2012.

[6] N. Jayarambabu, B. S. Kumari, K. V. Rao, & Y. T. Prabhu, “Germination and growth characteristics of mungbean seeds (Vigna radiata L.) affected by synthesized zinc oxide nanoparticles.” Int. J. Curr. Eng. Technol, 4(5), 3411-3416, 2014.

[7] H. Saadi, F. I. H. Rhouma, Z. Benzarti, Z. Bougrioua, S. Guermazi, and K. Khirouni,

“Electrical conductivity improvement of Fe doped ZnO nanopowders,” Mater Res Bull, vol.

129, Sep. 2020, doi: 10.1016/j.materresbull.2020.110884.

[8] R. Mastan, A. Khorsand Zak, and R. Pilevar Shahri, “Bi-doped ZnO yellow

nanopigments: Synthesis, characterization, and antibacterial application for painting humid places," Ceram Int, vol. 46, no. 7, pp. 8582–8587, May 2020, doi: 10.1016/j.ceramint.2019.12.090.

[9] H. Nezzal, N. E. H. Redjouh, "Elaboration of pure and Bi-doped ZnO nano-powders with the sol-gel method," Master memory, 2022

[10] A. T. Ravichandran, R. Karthick, K. Ravichandran, D. Ravinder, and R. Chandramohan, "Revealing the influence of the Bi dopant on the structural, photoluminescence and antibacterial properties of ZnO nanoparticles," Journal of Materials Science: Materials in Electronics, vol. 29, no. 4, pp. 2784–2790, Feb. 2018, doi: 10.1007/s10854-017-8206-6.

[11] S. Gharbi et R. Dhahri, M. Rasheed, E. Dhahri, R. Barille, M. Rguiti, "Effect of Bi substitution on nanostructural, morphologic, and electrical behavior of nanocrystalline La1-xBixNi0.5Ti0.5O3 (x = 0 and x = 0.2) for the electrical devices," Materials Science and Engineering: B, vol. 270, Aug. 2021, doi: 10.1016/j.mseb.2021.115191.

[12] C. Belkhaoui, N. Mzabi, H. Smaoui, and P. Daniel, "Enhancing the structural, optical and electrical properties of ZnO nanopowders through (Al + Mn) doping," Results Phys, vol. 12, pp. 1686–1696, Mar. 2019, doi: 10.1016/j.rinp.2019.01.085.

[13] K. Karthika and K. Ravichandran, "Tuning the Microstructural and Magnetic Properties of ZnO Nanopowders through the Simultaneous Doping of Mn and Ni for Biomedical Applications," J Mater Sci Technol, vol. 31, no. 11, pp. 1111–1117, Nov. 2015, doi: 10.1016/j.jmst.2015.09.001.

[14] V. Pazhanivelu, A. Paul Blessington Selvadurai, R. Kannan, and R. Murugaraj, "Room temperature ferromagnetism in Ist group elements codoped ZnO:Fe nanoparticles by coprecipitation method," Physica B Condens Matter, vol. 487, pp. 102–108, Apr. 2016, doi: 10.1016/j.physb.2016.02.001.

[15] M. B. Nayan, K. Jagadish, M. R. Abhilash, K. Namratha, and S. Srikantaswamy,"Comparative Study on the Effects of Surface Area, Conduction Band and Valence Band Positions on the Photocatalytic Activity of ZnO Heterostructures," J Water Resour Prot, vol. 11, no. 03, pp. 357–370, 2019, doi: 10.4236/jwarp.2019.113021.

[16] J. L. Ortiz-Quiñonez, I. Zumeta-Dubé, D. Díaz, N. Nava-Etzana, E. Cruz-Zaragoza, and P. Santiago-Jacinto, "Bismuth Oxide Nanoparticles Partially Substituted with EuIII, MnIV, and SiIV: Structural, Spectroscopic, and Optical Findings," Inorg Chem, vol. 56, no. 6, pp. 3394–3403, Mar. 2017, doi: 10.1021/acs.inorgchem.6b02923.

[17] J. Yang, T. Xie, C. Liu, and L. Xu, "Facile fabrication of dumbbell-like β-Bi2O3/ graphene nanocomposites and their highly efficient photocatalytic activity," Materials, vol. 11, no. 8, Aug. 2018, doi: 10.3390/ma11081359.

[18] D. Bouras and M. Rasheed, "Comparison between CrZO and AlZO thin layers and the effect of doping on the lattice properties of zinc oxide," Opt Quantum Electron, vol. 54, no. 12, Dec. 2022, doi: 10.1007/s11082-022-04161-1.

[19] A. Boumezoued, K. Guergouri, R. Barille, D. Rechem, M. Zaabat, and M. Rasheed,"ZnO nanopowders doped with bismuth oxide, from synthesis to electrical application," J Alloys Compd, vol. 791, pp. 550–558, Jun. 2019, doi: 10.1016/j.jallcom.2019.03.251.

[20] M. Mohamed, A. Sedky, A. S. Alshammari, Z. R. Khan, M. Bouzidi, and M. Gandouzi, "Structural, morphological, optical, photocatalytic activity investigations of Bi doped ZnO nanoparticles," Opt Mater (Amst), vol. 136, Feb. 2023, doi: 10.1016/j.optmat.2022.113347.

[21] T. K. Pathak, H. C. Swart, and R. E. Kroon, "Influence of Bi doping on the structure and photoluminescence of ZnO phosphor synthesized by the combustion method," Spectrochim Acta A Mol Biomol Spectrosc, vol. 190, pp. 164–171, Feb. 2018, doi: 10.1016/j.saa.2017.09.026.

[22] T. Prakash, G. Neri, A. Bonavita, E. Ranjith Kumar, and K. Gnanamoorthi, "Structural, morphological and optical properties of Bi-doped ZnO nanoparticles synthesized by a microwave irradiation method," Journal of Materials Science: Materials in Electronics, vol. 26, no. 7, pp. 4913–4921, Jul. 2015, doi: 10.1007/s10854-015-3002-7.

[23] J. Kazmi , P. C. Ooi, B. T. Goh, M. K. Lee, M. M. R. Wee, S. S. A. Karim, & M. A.

Mohamed, "Bi-doping improves the magnetic properties of zinc oxide nanowires," RSC Adv, vol. 10, no. 39, pp. 23297–23311, Jun. 2020, doi: 10.1039/d0ra03816d.

[24] B. Alemán, P. Hidalgo, P. Fernández, & J. Piqueras, "Thermal growth and cathodoluminescence of Bi doped ZnO nanowires and rods." Journal of Physics D: Applied Physics, 42(22), 225101. 2009, doi: 10.1088/0022-3727/42/22/225101

[25] D. Bouras, M. Rasheed, R. Barille, and M. N. Aldaraji, "Efficiency of adding DD3+(Li/Mg) composite to plants and their fibers during the process of filtering solutions of toxic organic dyes," Opt Mater (Amst), vol. 131, Sep. 2022, doi: 10.1016/j.optmat.2022.112725.

[26] S. W. Xue, X. T. Zu, W. L. Zhou, H. X. Deng, X. Xiang, L. Zhang, & H. Deng, "Effects of post-thermal annealing on the optical constants of ZnO thin film," J Alloys Compd, vol. 448, no. 1–2, pp. 21–26, Jan. 2008, doi: 10.1016/j.jallcom.2006.10.076.

[27] S. Senthilkumaar, K. Rajendran, S. Banerjee, T. K. Chini, and V. Sengodan, "Influence of Mn doping on the microstructure and optical property of ZnO," Mater Sci Semicond Process, vol. 11, no. 1, pp. 6–12, Feb. 2008, doi: 10.1016/j.mssp.2008.04.005.

[28] I. Ghiloufi, J. El Ghoul, A. Modwi, and L. El Mir, "Ga-doped ZnO for adsorption of heavy metals from aqueous solution," Mater Sci Semicond Process, vol. 42, pp. 102–106, Feb. 2016, doi: 10.1016/j.mssp.2015.08.047.

[29] C. Y. Tsay, K. S. Fan, and C. M. Lei, "Synthesis and characterization of sol-gel derived gallium-doped zinc oxide thin films," J Alloys Compd, vol. 512, no. 1, pp. 216–222, Jan. 2012, doi: 10.1016/j.jallcom.2011.09.066.

[30] A. K. Srivastava and J. Kumar, "Effect of zinc addition and vacuum annealing time on the properties of spin-coated low-cost transparent conducting 1 at% Ga-ZnO thin films," Sci Technol Adv Mater, vol. 14, no. 6, Dec. 2013, doi: 10.1088/1468-6996/14/6/065002.

[31] S. D. Senol, O. Ozturk, & C. Terzioğlu, "Effect of boron doping on the structural, optical and electrical properties of ZnO nanoparticles produced by the hydrothermal method." Ceramics International, 41(9), 11194-11201, (2015), doi :10.1016/j.ceramint.2015.05.069

[32] W. D. Callister Jr and D. G. Rethwisch, Characteristics, Application, and Processing of Polymers. 2018.

[33] A. Latif, L. Arab, A. Amri, H. Arab, N. Sengouga, and T. Tibermacine, “Effect of Ga doping on the structural, optical, and electrical properties of ZnO nanopowders elaborated by sol-gel method,” Mater Res Bull, vol. 178, Oct. 2024, doi: 10.1016/j.materresbull.2024.112886.

[34] K. Karthika and K. Ravichandran, “Tuning the Microstructural and Magnetic Properties of ZnO Nanopowders through the Simultaneous Doping of Mn and Ni for Biomedical Applications,” J Mater Sci Technol, vol. 31, no. 11, pp. 1111–1117, 2015, doi: 10.1016/j.jmst.2015.09.001.

[35] J. Liu ,W. Zhang, D. Song, Q. Ma, L. Zhang, H. Zhang, & H. Song, “Gallium-doped zinc oxide targets fabricated by sintering: Impact of target quality on sputtered thin film properties,” Mater Sci Semicond Process, vol. 27, no. 1, pp. 1–11, 2014, doi: 10.1016/j.mssp.2014.06.005.

[36] D. Guruvammal, S. Selvaraj, and S. Meenakshi Sundar, “Effect of Ni-doping on thestructural, optical and magnetic properties of ZnO nanoparticles by solvothermal method,” J Alloys Compd, vol. 682, pp. 850–855, 2016, doi: 10.1016/j.jallcom.2016.05.038.

[37] L. Umaralikhan, & M. J. M, “Green synthesis of ZnO and Mg doped ZnO nanoparticles, and its optical properties.” Journal of Materials Science: Materials in Electronics, 28, 7677- 7685. 2017, doi: 10.1007/s10854-017-6461-1

[38] A. J. Reddy , M. K. Kokila, H. Nagabhushana, R. P. S. Chakradhar, C. Shivakumara, J. L. Rao, & B. M. Nagabhushana, “Structural, optical and EPR studies on ZnO:Cu nanopowders prepared via low temperature solution combustion synthesis,” J Alloys Compd, vol. 509, no. 17, pp. 5349–5355, 2011, doi: 10.1016/j.jallcom.2011.02.043.

[39] M. L. da Silva-Neto, M. C. de Oliveira, C. T. Dominguez, R. E. Lins, N. Rakov, C. B. de Araújo, & A. S. Gomes, “UV random laser emission from flexible ZnO-Ag-enriched electrospun cellulose acetate fiber matrix,” Sci Rep, vol. 9, no. 1, Dec. 2019, doi: 10.1038/s41598-019-48056-w.

Chapter IV

Applications of the Zinc oxide elaborated

Introduction

Zinc oxide exhibits tremendous potential for diverse applications in biology and electronics. In this research, we investigate the effect of bismuth and gallium doping on ZnO antibacterial properties and its importance in the field of varistors. We aim to enhance the effectiveness of zinc oxide in combating bacteria, understand its properties as a fundamental element in modern electronic devices, and evaluate the impact of doping on variable resistance properties. We expect our results to lead to a better understanding of the effect of doping on zinc oxide and to open new avenues for its applications in various fields, contributing to the development of new materials with antibacterial properties and improving the efficiency of semiconductor devices.

In this chapter, we outline the methodology of our study, as depicted in figure IV.1. We fabricated samples for both antibacterial and varistor applications through the sintering of ZnO powder samples prepared using the sol-gel method.

Each application is based on a distinct study protocol, detailed in parts A and B. Part A investigates the antibacterial efficacy of pure ZnO samples and those doped with bismuth and gallium against various bacteria strains. Part B examines the performance of ZnO powder in varistor applications, comparing the impact of doping on the I-V characteristics under high voltage conditions.

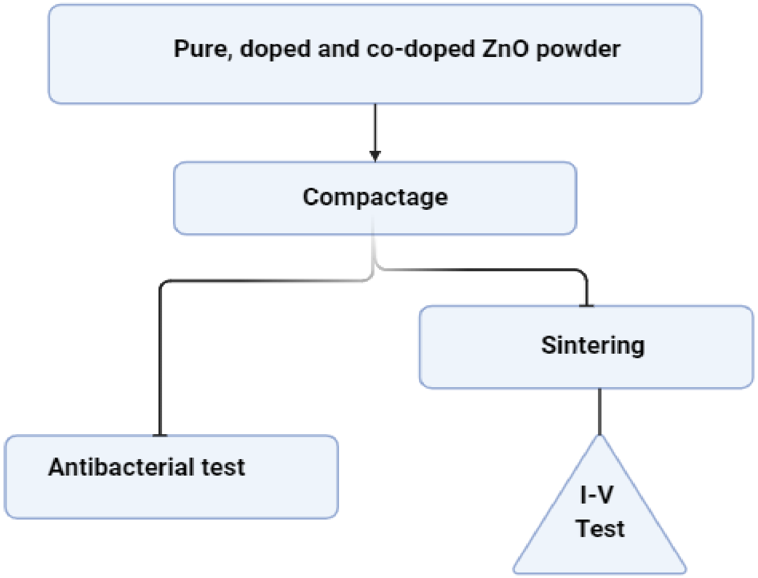

Figure IV.1: Applied studies on zinc oxide powder prepared by the sol-gel method.

Part A: Antibacterial activity

IV .A.1. Antibacterial Properties of Zinc Oxide Nanoparticles

IV .A.1.1. Preparation method

The undoped, doped, and co-doped ZnO nanopowders with different Bi and Ga concentrations were evaluated for their antibacterial efficacy against both Gram-positive and Gram-negative bacteria derived from 24-hour cultures. The bacterial suspensions, adjusted to concentrations of approximately 108 CFU/mL relative to the 0.5 McFarland standard, were composed of Escherichia coli ATCC 25922, Klebsiella pneumoniae ATCC 13883, Enterobacter aerogenes ATCC 13048, and Listeria monocytogenes ATCC 19114 [1]. To conduct the tests, 20 ml of sterile Mueller-Hinton agar (containing 2% beef extract, 17.5% acid hydrolysate of casein, 1.5% starch, and 1.5% agar) were used to prepare the plates. The plates were inoculated with a sterile swab soaked in the bacterial suspension, allowed to dry, and subsequently treated with materials of varying concentrations [2]. Following incubation at 37ºC for 24 hours, clear inhibition zones surrounding the disks were observed and measured using a caliper. Figure IV.2 shows a pictorial representation of the antibacterial test procedure.

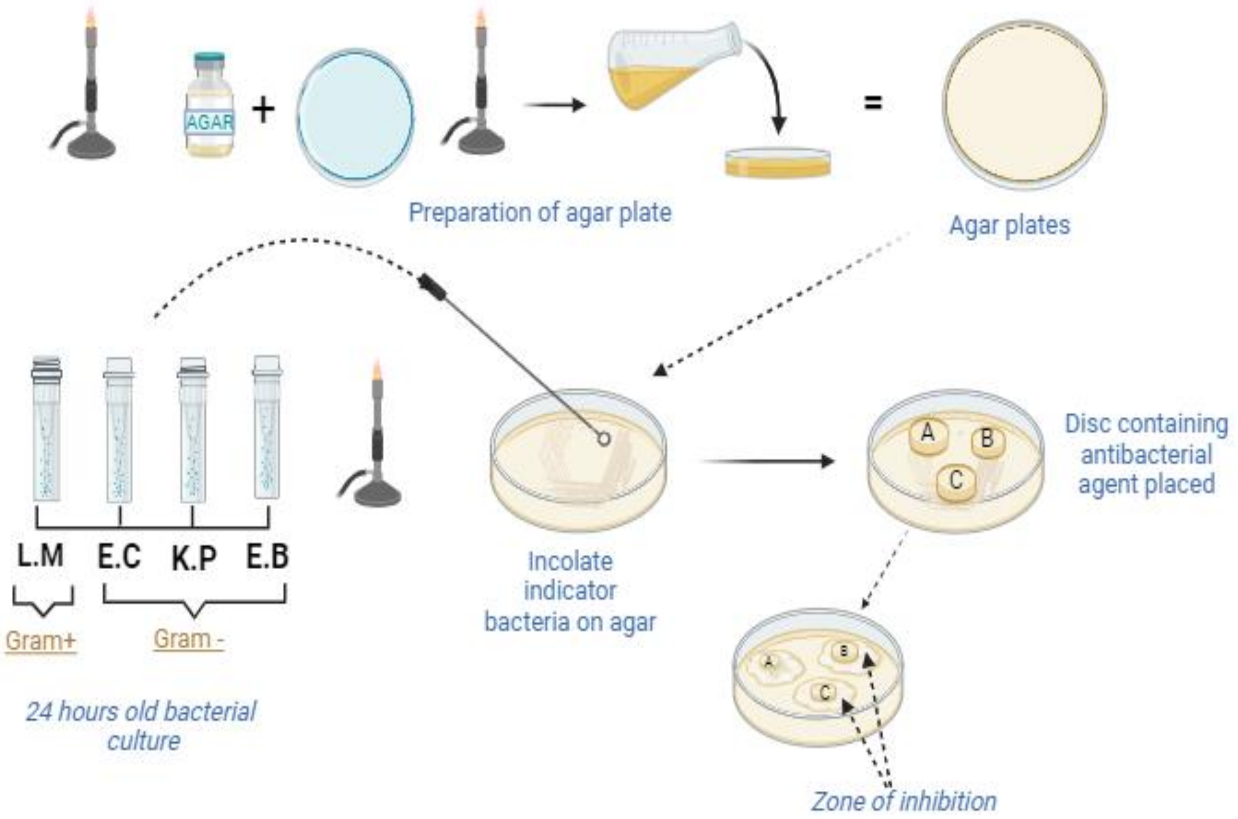

Figure IV. 2: **Pictorial representation of the antibacterial test procedure.**

IV .A.1.2. Antibacterial activity

IV .A.1.2.1. Bi doped ZnO nanopowder

Figure IV. 3 illustrates the antibacterial activity as indicated by the size of the distinct inhibition zones. Indeed, the results showed varying degrees of inhibition against the tested microorganisms at different concentrations of Bi doped ZnO (Table IV. 1, and Figure IV. 4). In comparing the synthesized compounds, A (ZnO: 0% Bi), B (ZnO: 3% Bi), C (ZnO: 6% Bi), and D (ZnO: 8%Bi), distinct trends emerge regarding their inhibitory effects against the tested bacterial strains. Compound A (ZnO: 0% Bi) consistently demonstrates superior antibacterial activity, exhibiting larger inhibition zones compared to B (ZnO: 3% Bi), C (ZnO: 6%Bi), and D (ZnO 8% Bi), across Escherichia coli ATCC 25922, Klebsiella pneumoniae ATCC 13883, Enterobacter aerogenes ATCC 13048, and Listeria monocytogenes ATCC 19114. Notably, compound A (ZnO:

0% Bi) surpasses others in inhibitory potency against E. coli and E. aerogenes. Compound B (ZnO: 3% Bi) generally falls intermediate in terms of effectiveness, showcasing larger inhibition zones than C (ZnO: 6% Bi) and D (ZnO: 8% Bi) against K. pneumoniae and L. monocytogenes. Compound C (ZnO: 6% Bi), while demonstrating competitive inhibitory effects, particularly against E. aerogenes and L. monocytogenes, tends to exhibit smaller inhibition zones compared to A (ZnO: 0% Bi) and B (ZnO: 3% Bi). Lastly, compound D (ZnO: 8% Bi), although generally less potent than A and B, displays notable inhibitory activity against K. pneumoniae and E. aerogenes. These comparative insights underscore the nuanced and concentration-dependent nature of the synthesized compounds' antibacterial efficacy against the specific bacterial strains tested [3]

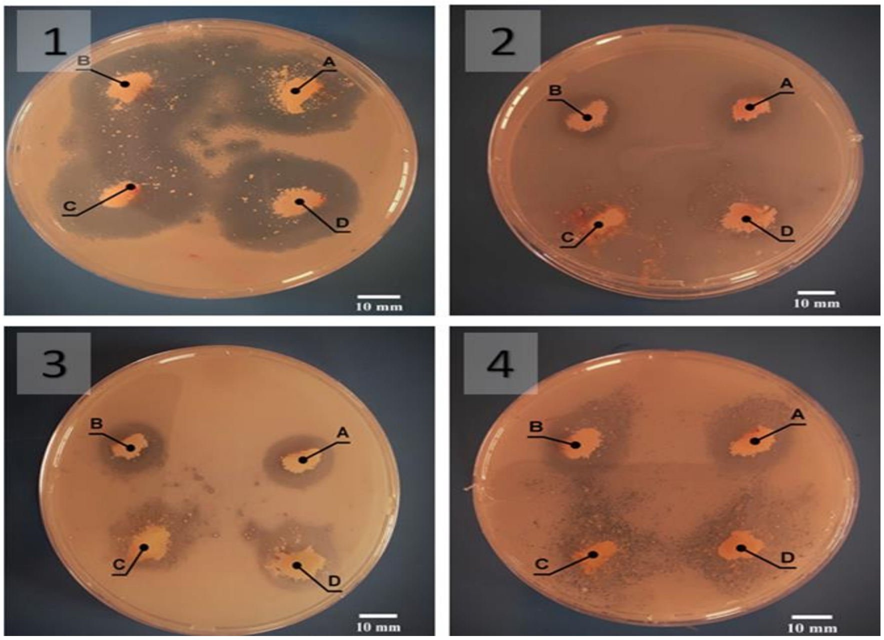

Figure IV.3: Antimicrobial activity of synthesized products at different concentrations (A: ZnO: 0% Bi; B: ZnO: 3% Bi, C: ZnO: 6% Bi, and D: ZnO: 8% Bi) against (1) Escherichia coli ATCC 25922, (2) Klebsiella pneumoniae ATCC 13883, (3) Enterobacter aerogenes ATCC 13048, and (4) Listeria monocytogenes ATCC 19114.

Table IV.1: Comparative Analysis of Inhibition Zones (mm) for Synthesized products Against Tested Microorganism Strains

Synthesized products at different concentrations	***Escherichia coli ATCC 25922***	***Klebsiella pneumoniae ATCC 13883***	***Enterobacter aerogenes ATCC 13048***	***Listeria monocytogenes ATCC 19114***
A (**ZnO: 0% Bi**)	37.17±2.23	19.08±2.19	18.50±0.59	24.83±3.39
B (**ZnO: 3% Bi**)	34.20±2.47	16.12±1.26	17.49±1.09	24.83±3.39
C (**ZnO: 6% Bi**)	31.73±1.65	17.7±0.37	24.70±1.42	25.04±3.89
D (**ZnO: 8% Bi**)	32.85±3.66	12.455±2.00	26.22±1.99	28.38±5.44

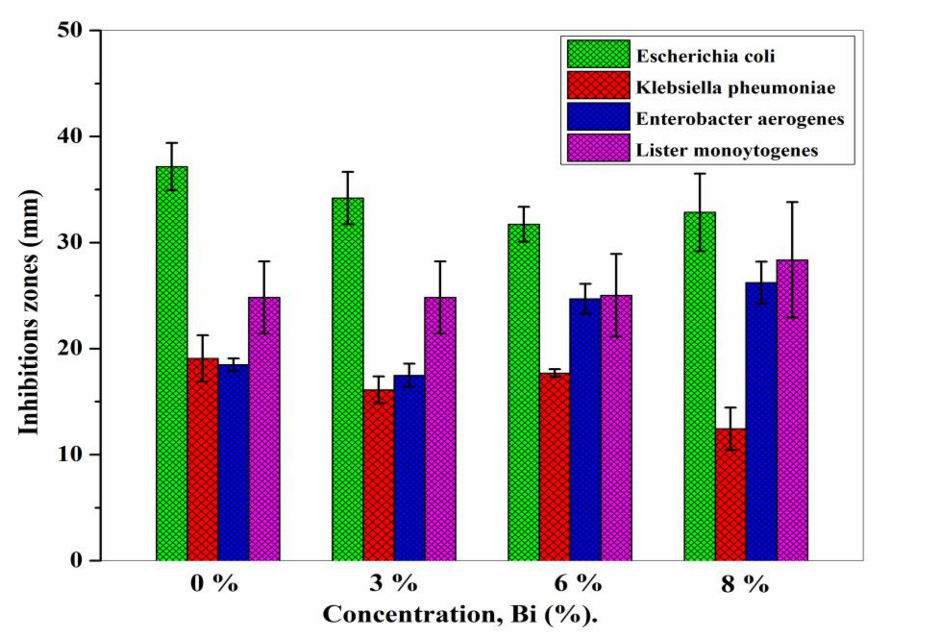

Figure IV.4: **Antimicrobial activity results of synthesized products expressed in millimeters of inhibition zone. Data are expressed as means ± SE (n = 3).**

The variable degrees of inhibition seen at various concentrations of Bi dopant are due to the intricate interaction between the material's characteristics and the tested bacterial strains. Inhibition's dependence on concentration can be affected by characteristics including surface area, surface charge, and the presence of active detects for bacterium interaction. Increasing the concentration of Bi dopant can lead to modifications in the material's structure and characteristics, which can impact its interaction with bacterial cells. [4] . The antibacterial activity could be affected by the intrinsic characteristics of the bacterial strains, namely their cell wall structure and membrane permeability [5].

Under antibacterial conditions, the stability and longevity of the material are influenced by the band gap. The material's susceptibility to degradation may be increased due to smaller band gaps; therefore, it is crucial to comprehend the compromise between improved antibacterial activity and material stability to develop practical applications, particularly those that require sustained antibacterial performance. The correlation between the band gap and doping concentrations underscores the possibility of manipulating the antibacterial characteristics of the ZnO nanopowders that were synthesized [6- 9].

IV .A.1.2.2. Ga doped ZnO nanopowder

The bacterial activity of gallium-doped zinc oxide samples takes a different trajectory, as observed from the table IV.2 and (Figure IV.5 and IV.6). For Escherichia coli, ZnO exhibited a zone of 16.28±1.17 mm, while ZnO 3% Ga, ZnO 6% Ga, and ZnO 8% Ga demonstrated increased inhibitory effects at 17.41±0.54 mm, 17.84±0.36 mm, and 18.18±1.36 mm, respectively. Klebsiella pneumoniae showed a similar trend, with ZnO displaying a zone of 20.39±0.59 mm, ZnO 3% Ga, ZnO 6% Ga, and ZnO 8% Ga exhibiting larger zones at 26.98±0.04 mm, 25.40±1.04 mm, and 21.84±0.06 mm, respectively. Notably, Listeria monocytogenes demonstrated substantial susceptibility, with ZnO, ZnO 3% Ga, ZnO 6% Ga, and ZnO 8% Ga displaying zones of 26.48±0.37 mm, 26.84±1.47 mm, 26.46±0.41 mm, and 29.58±0.89 mm, respectively.

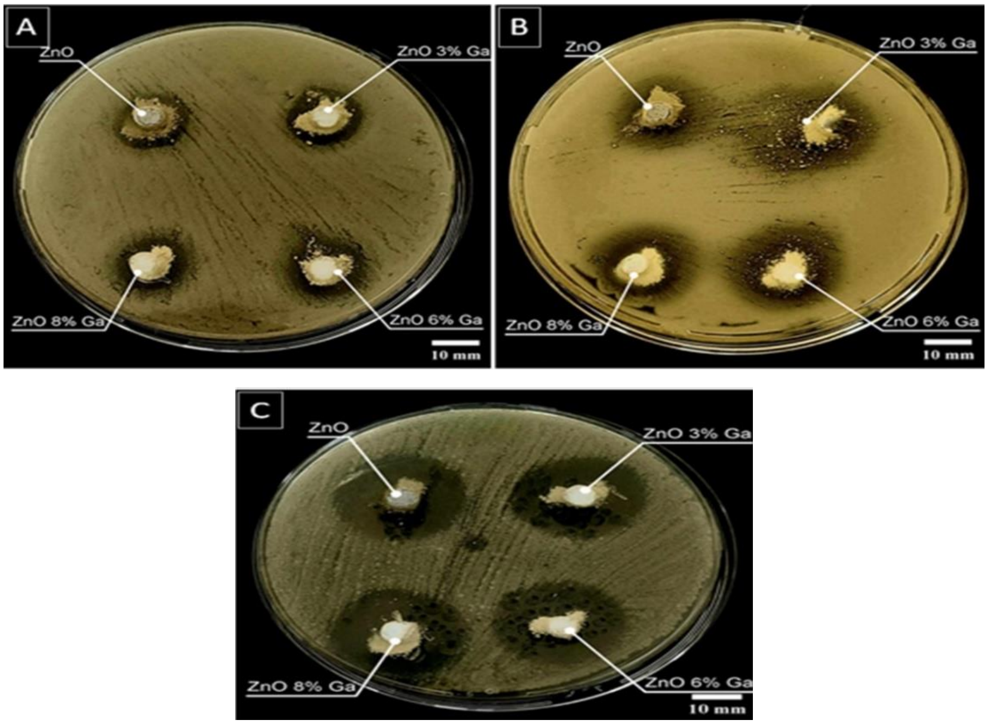

Figure IV.5: Antimicrobial activity of synthesized products at different concentrations (ZnO, ZnO 3% Ga, ZnO 6% Ga, ZnO 8% Ga), against (A) Escherichia coli ATCC 25922, (B) Klebsiella pneumoniae ATCC 13883, (C) Listeria monocytogenes ATCC 19114.

Table IV.2: Comparative analysis of the zones of inhibition (mm) of the product synthesized at different concentrations against the microorganism strains tested.

synthesized Products at different concentrations	***Escherichia coli* *ATCC 25922***	***Klebsiella pneumoniae* *ATCC 13883***	***Listeria monocytogenes ATCC 19114***
ZnO: 0% Ga	16.28±1.17	20.39±0.59	26.48±0.37
ZnO : 3% Ga	17.41±0.54	26.98±0.04	26.84±1.47
ZnO : 6% Ga	17.84±0.36	25.40±1.04	26.46±0.41
ZnO : 8% Ga	18.18±1.36	21.84±0.06	29.58±0.89

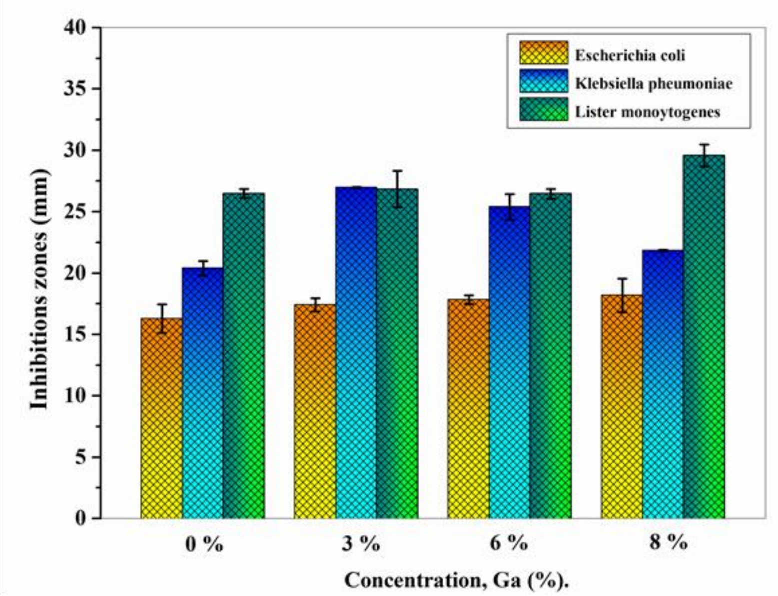

Figure IV.6: Antimicrobial activity results of synthesized Ga doped ZnO nanopowdrs expressed in millimetres of inhibition zone. Data are expressed as means ± SE (n = 3).

In the current work, the antibacterial activity of the synthesized nanoparticles can be elucidated as follows: after the addition of Ga with ZnO, the proper replacement of Ga^{3+} in the position of Zn^{2+} takes place in ZnO molecular structure as the ionic radii of Ga^{3+} (0.062 nm) is comparably lower than the ionic radii of Zn^{2+} (0.074 nm). This replacement causes more number of Zn^{2+} interstitials in the ZnO matrix. The Zn^{2+} existence is affirmed by using structural studies. As interstitial Zn^{2+} ions can be freely liberated from ZnO lattice compared with Zn^{2+} regular position, Ga doped ZnO nanoparticles have more capability to work as a superior antimicrobial mediator. The produced Zn^{2+} ions result in cell wall damage due to the direct diffusion into the cell membrane causing the consequent leakage of cell contents. Here, ZnO with Ga doping (8 %) has high antibacterial activity against E. coli and listeria monocytogenes while Ga doping with 3 % has high antibacterial activity against Klebsiella pneumoniae [10].

IV .A.1.2.3. Bi-Ga co-doped

Both table IV.3 and figure IV.8 illustrate the antibacterial efficacy of zinc oxide samples co-doped with different concentrations of gallium and bismuth as extorted from the antibacterial test results in figure IV.7, with measurements expressed as the mean diameter (millimeter) of the zone of inhibition. Analysis of the results reveals distinct patterns for each bacterial strain. Firstly, the diameters of the zone of inhibition of Escherichia coli fluctuate between around 22.71 and 33.01 mm across the entire concentration spectrum. In particular, concentration B stands out as having the highest inhibitory effect. For Klebsiella pneumoniae, the observed diameters ranged from 18.78 to 25.87 mm. This variability indicates a potential concentration-dependent impact on inhibitory efficacy against this bacterial strain. Enterobacter aerogenes showed a narrower range of inhibition zone diameters, varying from around 16.80 to 19.52 mm. The comparatively limited variability suggests a potentially less concentration-sensitive response in this case. Finally, Listeria monocytogenes showed relatively consistent inhibition zone diameters, ranging from around 20.47 to 22.97 mm for the different concentrations. This suggests a more stable antimicrobial effect on this bacterial strain.

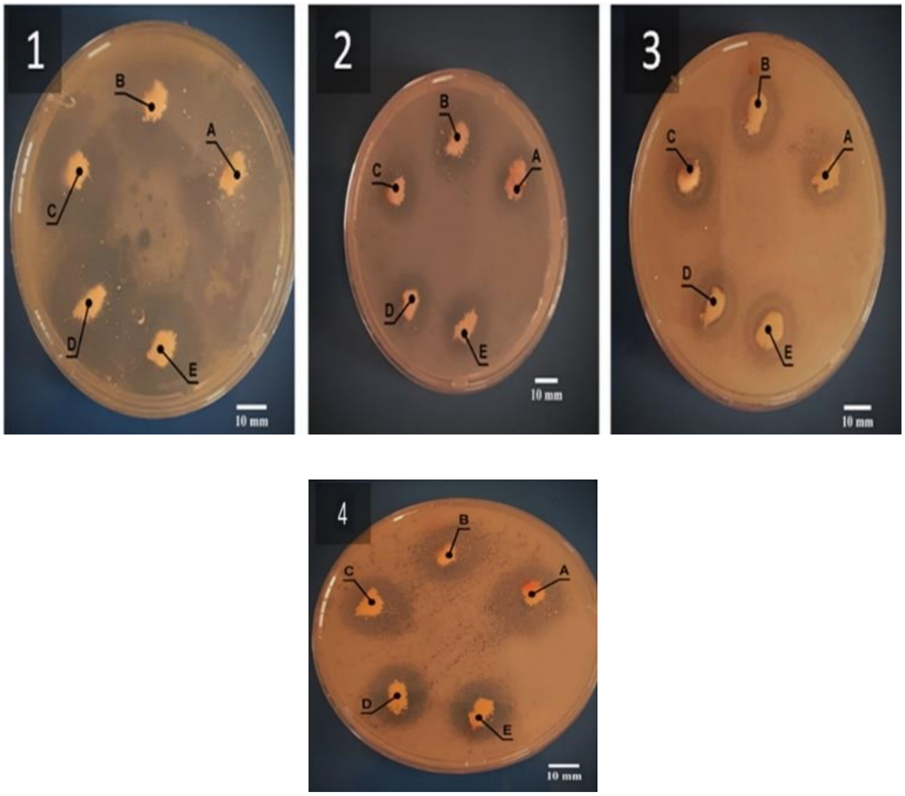

Figure IV.7: Antimicrobial activity of Bi and Ga co doped ZnO with different concentrations (A: ZGBO 00, B: ZGBO 33, C: ZGBO 35, D: ZGBO 53, and E: ZGBO 55) against (1) Escherichia coli ATCC 25922, (2) Klebsiella pneumoniae ATCC 13883, (3) Enterobacter aerogenes ATCC 13048, and (4) Listeria monocytogenes ATCC 19114.

Table IV.3: Comparative analysis of the zones of inhibition (mm) of the product synthesized at different concentrations against the microorganism strains tested.

synthesized Products at different concentrations	*Escherichia coli ATCC 25922*	*Klebsiella pneumoniae ATCC 13883*	*Enterobacter aerogenes ATCC 13048*	*Listeria monocytogenes ATCC 19114*
A	31.94±0.16	25.87±5.15	19.52±2.82	20.47±0.07
B	33.01±6.37	19.38±0.47	19.32±1.46	21.46±1.22
C	29.21±3.49	18.78±1.00	17.26±1.92	20.61±2.72
D	30.23±1.13	21.07±1.57	19.07±0.04	20.76±0.83
E	22.71±7.79	19.53±2.04	16.80±1.12	22.97±0.15

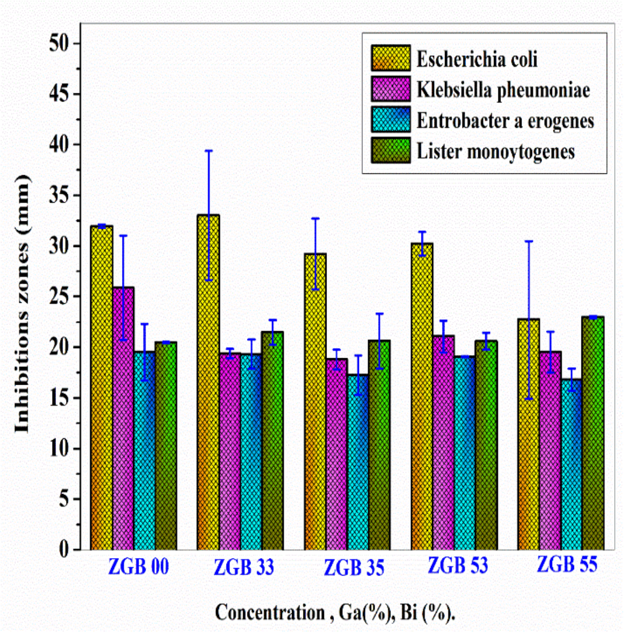

Figure IV.8: Antimicrobial activity results of synthesized Ga and Bi co-doped ZnOnanopowders expressed in millimeters of inhibition zone.Data are expressed as means ± SE (n = 3).

Zinc oxide, whether pure or doped with different concentrations of gallium and bismuth, shows good antibacterial activity. The observed improvement in antibacterial activity against different bacterial species can be attributed to variations in bacterial strains, such as the chemical composition of the cell wall and the defense mechanisms employed. It is observed that higher antibacterial activity of synthesized nanoparticles is happened due to two important factors, such as (1) reduced size of the grains, (2) highly reactive oxygen spices (ROS) generated, including hydroxyl groups (OH), superoxide anions (O^2), and hydrogen peroxide (H_2O_2) [11]. In our work, the generation of ROS due to the free electrons caused by the incorporation of Bi^{3+} and Ga^{+3} ions into the ZnO lattice plays a crucial role. This could be the reason is ROS has the ability to destroy the bacteria. The generation of ROS can be represented as follows [12]:

$$\boldsymbol{ZnO + h\nu \rightarrow h^+ + e^-}$$

$$\boldsymbol{h^+ + H_2O \rightarrow OH^\bullet + H^+}$$

$$\boldsymbol{O_2 + e^- \rightarrow O_2^{\bullet-}}$$

$$\boldsymbol{O_2^{\bullet-} + H^+ \rightarrow HO_2^\bullet}$$

$$\boldsymbol{H^+ + HO_2^\bullet + e^- \rightarrow H_2O_2}$$

$$\boldsymbol{H_2O_2 + O_2^{\bullet-} \rightarrow OH^\bullet + O_2 + OH^-}$$

From these reactions, it is seen that the electron-hole pairs play a vital role in the generation of ROS. In comparing investigations (a, b, and c), the reference pure zinc oxide sample's ability to inhibit bacterial growth differed. The analyzed bacteria's genetic variances may be the cause of this divergence, which could impact on how the bacteria interact with ZnO. Furthermore, bacterial behavior and overall results may have been impacted by contamination resulting from incorrect storage of the ZnO sample and variations in environmental parameters like temperature and humidity.

Part B: Electrical behaviour

IV.B.1. Electrical Properties of Zinc Oxide Nanoparticles

IV.B.1.1. Samples preparation

Undoped, doped, and co-doped zinc oxide nanoparticles powders with different concentrations of Bi and Ga, were weighted (1.5 g) and pressed with a little bit of polyvinyl alcohol powder (PVA) into 10 mm diameter and 5 mm height disc by 150 MPa using a hydraulic press, the samples were sintered at 1100 °C for 1 h. After that, we used a silver coating to form electrodes on the surfaces of the sintered samples. Then, the samples were placed in a furnace for heat treatment from room temperature to 700°C for 15 minutes at a heating rate of 10°C/min to obtain the best adhesion with the surfaces of the sintered sample. Fabricated samples' electrical properties (nonlinear coefficient and breakdown voltage) were investigated by traditional method (I-V) curves. Figure IV.9 shows a pictorial representation of the I-V test procedure.

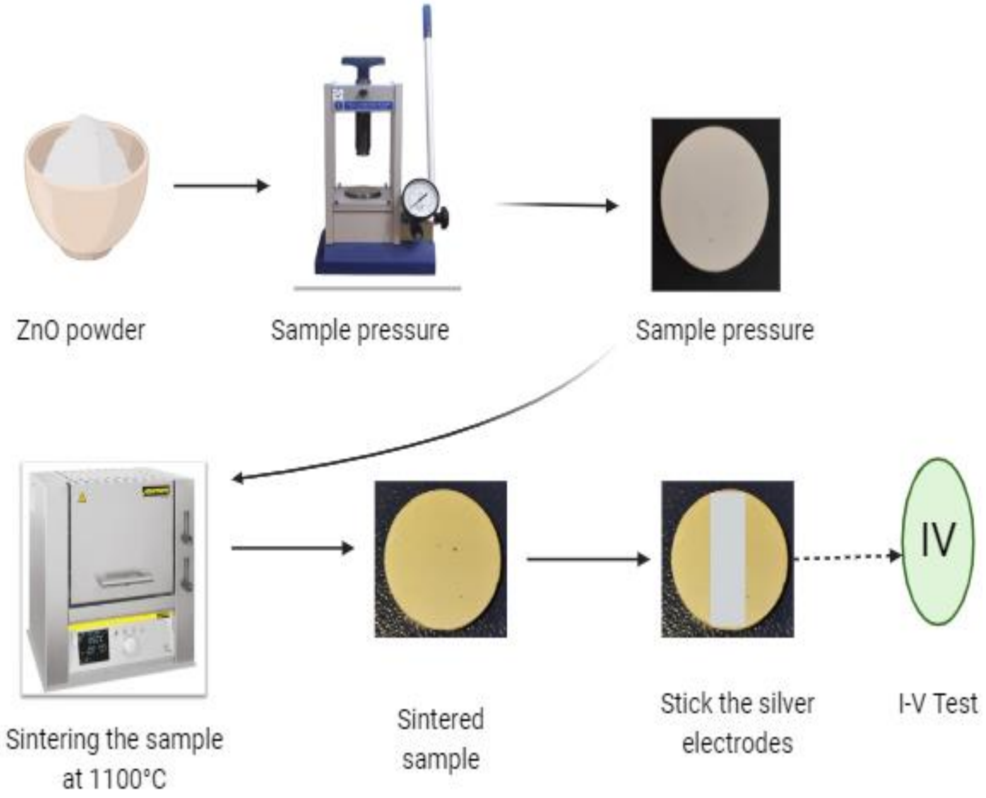

Figure IV. 9: Pictorial representation of the I-V test procedure.

IV.B.1.2. Electrical properties

Polycrystalline zinc oxide (ZnO) with additional components exhibits non-linear current-voltage characteristics (I-V). Barriers to electrical flow exist at the borders where the small crystals meet, known as grain boundaries [13, 14]. The most important feature of a varistor is this non-linear region. In this region, the material conducts electricity very differently. The current increases much faster than the voltage, causing a sharp rise in the I-V curve. This upward bend represents a voltage drop within the grains themselves, which limits the application of ZnO varistors [15].

Adding donor impurities (doping) can reduce the resistance within the grains. This slows down the voltage increase and pushes the sharp rise in the I-V curve to higher currents. The nonohmic character of the I(V) characterization is clearly indicate with the following equation:

$$\boldsymbol{I = KV^{\alpha}} \qquad \textbf{(IV.1)}$$

With, K is the material constant, and α the degree of non-linearity caused by solid-state reactions and the development of potential barriers between grains, it can be calculated from the formula (2):

$$\boldsymbol{\alpha = \frac{\log(I_2/I_1)}{\log(v_2/v_1)}} \qquad \textbf{(IV.2)}$$

Where V_1 and V_2 are voltages at currents I_1 and I_2, respectively.

IV.B.1.2.1. Bi doped ZnO

Analyzed the electrical characteristics of pure and Bi doped ZnO samples. Figure IV.9 displays the current (I, in amperes) vs voltage (V) curves on a logarithmic scale. This logarithmic scale is utilized for calculating the coefficient of nonlinearity (α). The graphic clearly illustrates that the behavior of pure ZnO may be divided into two various zones. At lower voltages, the material displays ohmic behavior, characterized by a proportionate increase in current with voltage. The behavior shifts to non-ohmic at higher voltages, suggesting a more intricate correlation between current and voltage.

A zinc oxide sample exhibited a breakdown voltage of 32.97 volts and a leakage current of 0.06 microamperes. The nonlinearity coefficient was calculated using equation 1 and found to be 1.9.

Zinc oxide samples doped with bismuth show a different response compared to pure ZnO. Instead of the non-linear behavior seen in pure ZnO, these doped samples exhibit a linear relationship between voltage and current, known as ohmic behavior. This lack of breakdown might be due to the applied voltage range of 0 to 100 volts being insufficient to trigger it, as suggested by previous studies [16- 18]. Additionally, the resistance of these doped samples is very high.

However, to gain a deeper understanding of how bismuth doping affects ZnO under varying voltage and current conditions, we can refer to Figure IV.10. This figure shows a magnified view, where we can observe an increase in the breakdown voltage for bismuth doped ZnO compared to pure ZnO. Furthermore, the leakage current also decreases with doping. These results suggest that bismuth doping increases the resistance within the ZnO grains, leading to improved varistor properties.

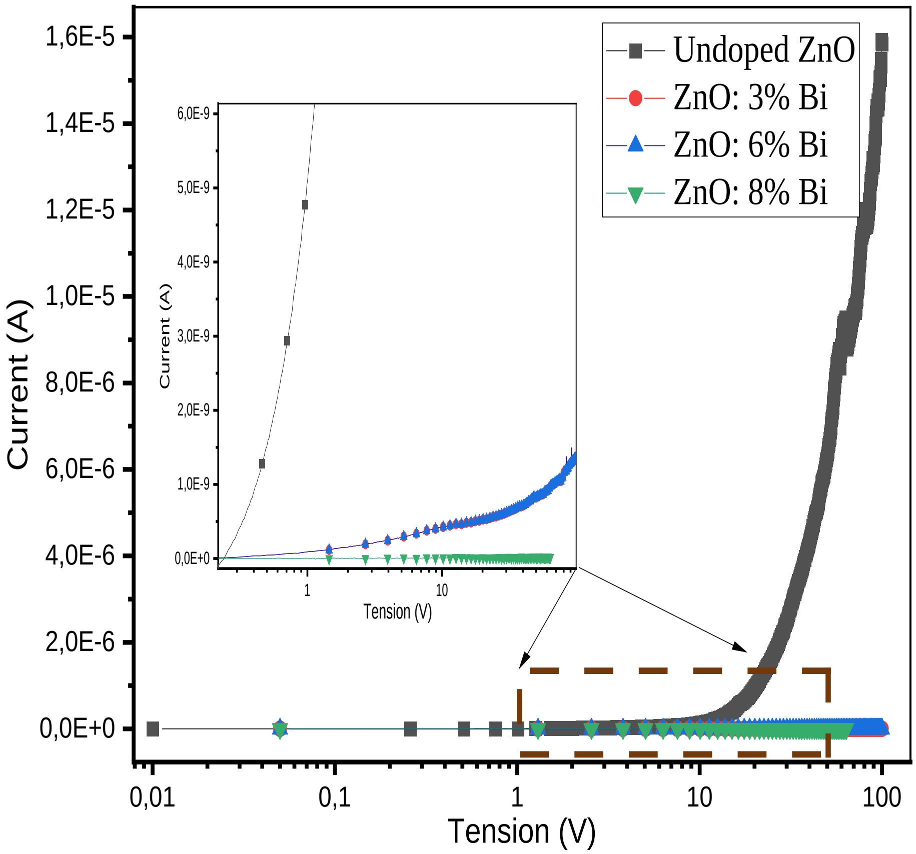

Figure IV.10: (I-V) characteristic of pure and doped ZnO with different concentration of Bi prepared by 1100 °C.

IV.B.1.2.2. Ga doping ZnO

Figure IV.11. represents pure and Ga-doped zinc oxide samples' I-V characteristics. The increase in the rhythm of the I-V is noticeable as a common feature between all the samples and can be divided into two regions, starting with a high resistance region also known as the "Ohmic region'. Followed by a low resistance region, which is considered a non-ohmic region. The second region describes the varistor's characteristics. On the other hand, the current increases strongly with the Ga concentration in the nonlinear region. According to H. Zhao et al. [19], the residual voltage decreases under a strong current in the upturn zone as the doping gallium concentration increases. As a result, the non-linear region is expanded, and the ability to discharge impulsive currents is greatly enhanced.

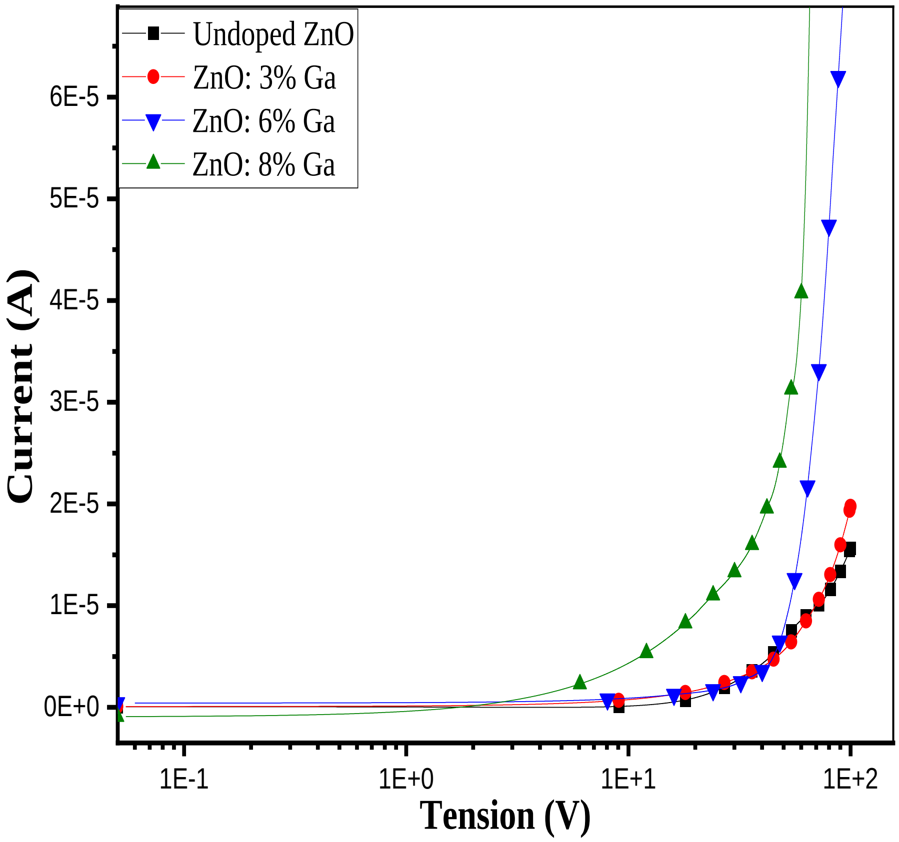

Figure IV. 11: I-V characteristics of pure and Ga-doped ZnO nanopowders.

Figure IV.11 illustrates that as the gallium concentration in zinc oxide samples, the nonlinear region becomes more pronounced due to the leakage current rate. This clarity begins to appear at a gallium concentration of 6% and higher, which allows for easy determination of both breakdown voltage and leakage current. The breakdown coefficient can also be calculated from this doping ratio. Table IV.4 gives a summary of the electrical characteristics. It shows that when the content of Ga dopants increases, the break-down voltage E_b decreases from 59.25 to 50.57 (V) upon the gallium doping increasing for both samples (ZnO: 6% Ga) and (ZnO: 8% Ga). This is due to the increase in the potential barrier and the number of grain boundaries, which contribute to the decrease in the ZnO grain size [20]. α increases with Ga concentration; this is obviously due to the decrease in average grain size [21], which is attributed to the increase in the number of grains and particle sizes.

Table IV.4 Electrical parameters of the ZnO samples with different Ga concentrations.

Ga ion additives	E_b (V)	I_L (μA)	α
6 %	**59.25**	**1.21**	**2.96**
8 %	**50.57**	**1.11**	**8.29**

IV.B.1.2.3. Bi and Ga co-doped ZnO

The nonlinear I-V curves of ZGBO samples are shown in figure IV.12. As a varistor, the current has no noticeable change in the pre-breakdown region, and it shows a surge increase in the breakdown region.

Figure IV.12 provides a comprehensive examination of the impact of gallium and bismuth co-doping on the leakage current and breakdown voltage of ZnO samples, facilitated by the magnification employed. The breakdown voltage of ZGBO 33 decreases significantly from 65 (V) to 59.99 (V) in the ZGBO 53 sample. The reduction can be ascribed to the creation of defects in the ZnO structure due to the existence of dopant atoms. In general, the co-doping of gallium and bismuth has a notable influence on the inductively valence (I-V) properties of zinc oxide (ZnO).

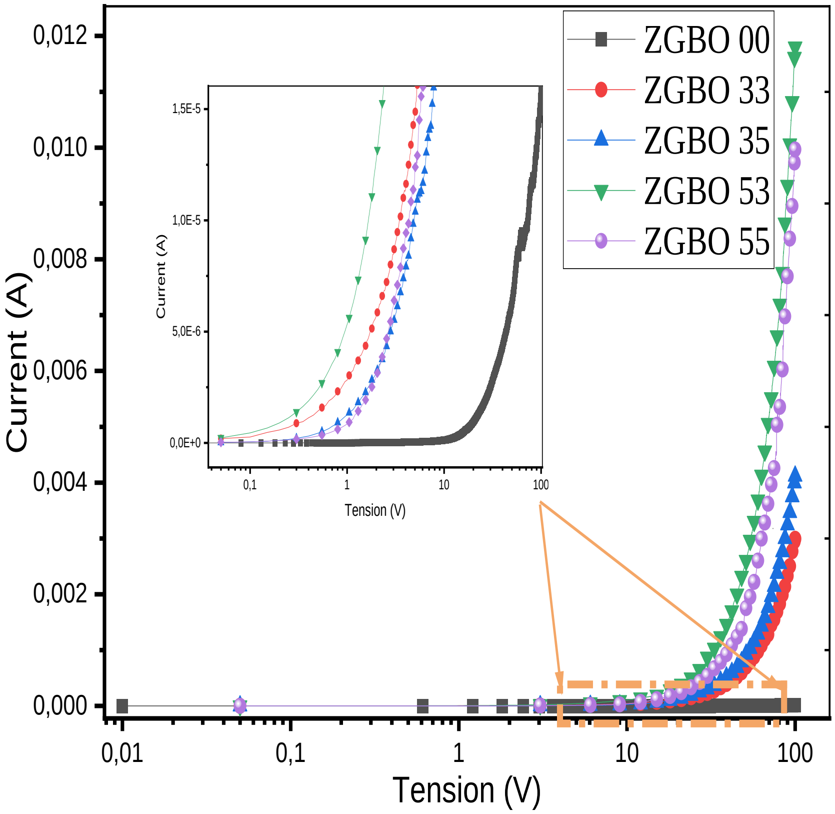

Figure IV. 12: I-V characteristics of pure and Bi,Ga co-doped ZnO nanopowders.

A sharper transition between the prebreak-down and break-down regions results in a higher non-linear coefficient ‘α’ value, leading to quicker time response and more efficient equipment protection [22, 23]. The current-voltage characteristics of the ZGBO samples sintered at 1100°c are shown on table IV. 5. It should be noted that the ZnO sample containing 3% Bi and 5% Ga indicate the sharped knee, corresponds to the highest nonlinear coefficient 7.42. At the same time, a higher leakage current I_L= 0.328 mA

Table IV.5 Electrical parameters of the co-doped ZnO with different concentrations of Bi and Ga.

Samples	**E_b (V)**	**I_L (µA)**	**α**
ZGBO 33	65.05	0.255	1.974
ZGBO 35	63.31	0.168	2.37
ZGBO 53	59.99	0.328	7.42
ZGBO 55	62.97	0.101	2.38

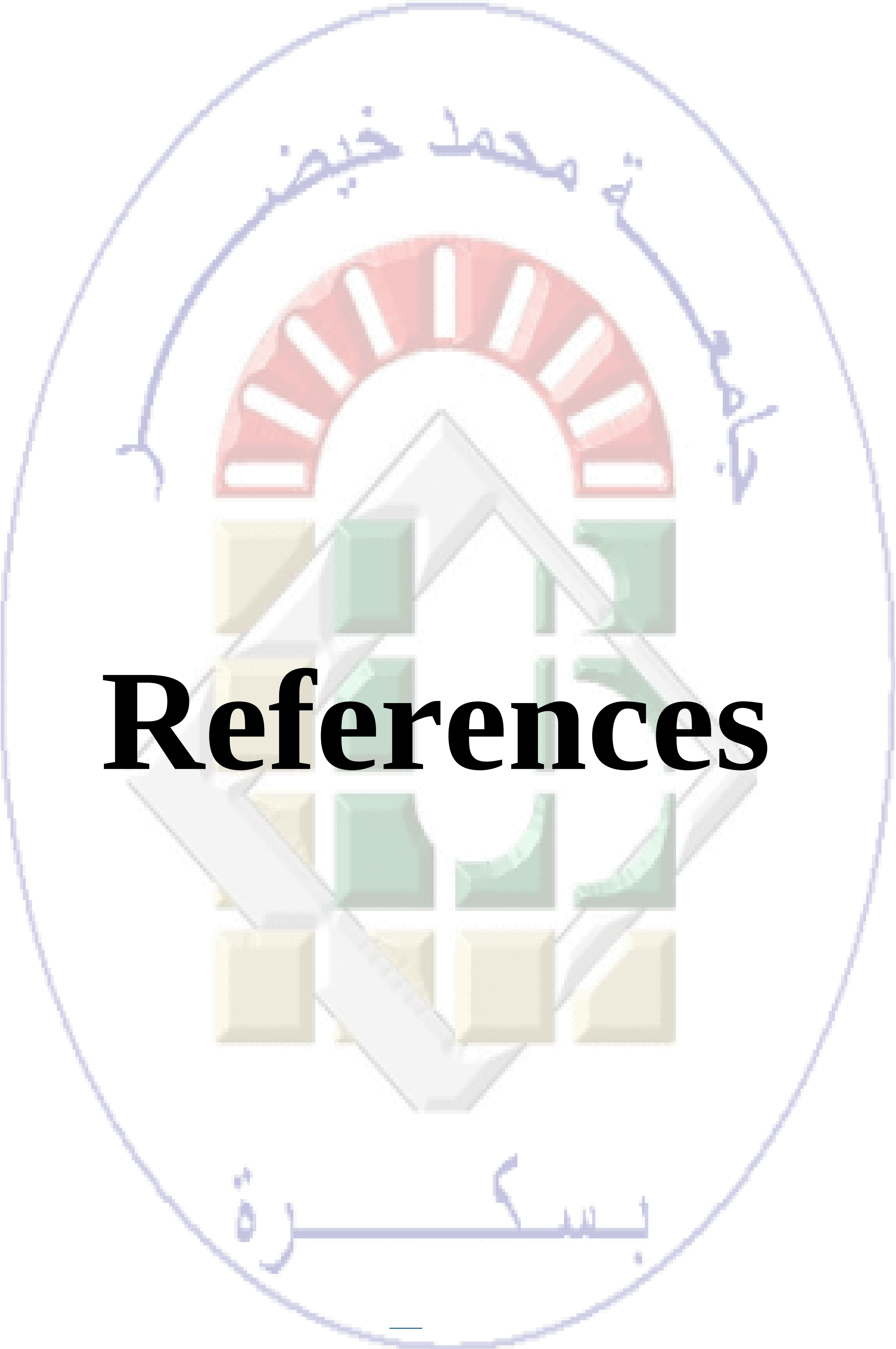

References

References

[1] Y. Hu, F. Zhu, G. Zhang, J. Bi, H. Hou, S. Yan, & H. Hao, “Construction of BiFeO3/BiVO4 nanofiber composites with pyroelectric and photocatalytic synergy for enhanced photocatalytic and antibacterial activity,” Colloids Surf A Physicochem Eng Asp, vol. 671, Aug. 2023, doi: 10.1016/j.colsurfa.2023.131641.

[2] M. L. Vică, I. Glevitzky, M. Glevitzky, C. V. Siserman, H. V. Matei, and C. A. Teodoru, “Antibacterial activity of propolis extracts from the central region of romania against neisseria gonorrhoeae,” Antibiotics, vol. 10, no. 6, Jun. 2021, doi: 10.3390/antibiotics10060689.

[3] A. T. Ravichandran, R. Karthick, K. Ravichandran, D. Ravinder, and R. Chandramohan, “Revealing the influence of the Bi dopant on the structural, photoluminescence and antibacterial properties of ZnO nanoparticles,” Journal of Materials Science: Materials in Electronics, vol. 29, no. 4, pp. 2784–2790, Feb. 2018, doi: 10.1007/s10854-017-8206-6.

[4] G. H. G. Ahmed, G. A. El-Naggar, F. Nasr, and E. A. Matter, “N-doped and N, Si-doped carbon dots for enhanced corrosion inhibition of mild steel in acidic environment,” Diam Relat Mater, vol. 136, Jun. 2023, doi: 10.1016/j.diamond.2023.109979.

[5] F. L. Orosco, “Recent advances in peptide-based nanovaccines for re-emerging and emerging infectious diseases,” Journal of Advanced Biotechnology and Experimental Therapeutics, vol. 7, no. 1. Bangladesh Society for Microbiology, Immunology and Advanced Biotechnology, pp. 106–117, 2024. doi: 10.5455/jabet.2024.d10.

[6] R. Mastan, A. Khorsand Zak, and R. Pilevar Shahri, “Bi-doped ZnO yellow nanopigments: Synthesis, characterization, and antibacterial application for painting humid places,” Ceram Int, vol. 46, no. 7, pp. 8582–8587, May 2020, doi: 10.1016/j.ceramint.2019.12.090.

[7] S. H. Khan, B. Pathak, and M. H. Fulekar, “A study on the influence of metal (Fe, Bi, and Ag) doping on structural, optical, and antimicrobial activity of ZnO nanostructures,” Adv Compos Hybrid Mater, vol. 3, no. 4, pp. 551–569, Dec. 2020, doi: 10.1007/s42114-020-00174-0.

[8] J. Liu, Y. Wang, J. Ma, Y. Peng, and A. Wang, “A review on bidirectional analogies between the photocatalysis and antibacterial properties of ZnO,” Journal of Alloys and Compounds, vol. 783. Elsevier Ltd, pp. 898–918, Apr. 30, 2019. doi: 10.1016/j.jallcom.2018.12.330.

[9] K. Qi, B. Cheng, J. Yu, and W. Ho, “Review on the improvement of the photocatalytic and antibacterial activities of ZnO,” Journal of Alloys and Compounds, vol. 727. Elsevier Ltd, pp. 792–820, Dec. 15, 2017. doi: 10.1016/j.jallcom.2017.08.142.

[10] P. Sathish, N. Dineshbabu, K. Ravichandran, T. Arun, P. Karuppasamy, M. SenthilPandian, & P. Ramasamy, “Combustion synthesis, characterization and antibacterial properties of pristine ZnO and Ga doped ZnO nanoparticles,” Ceram Int, vol. 47, no. 19, pp. 27934–27941, Oct. 2021, doi: 10.1016/j.ceramint.2021.06.224.

[11] G. Appierot , A. Lipovsky, R. Dror, N. Perkas, Y. Nitzan, R. Lubart, & A. Gedanken, “Enhanced antibacterial actiwity of nanocrystalline ZnO due to increased ROS-mediated cell injury,” Adv Funct Mater, vol. 19, no. 6, pp. 842–852, Mar. 2009, doi: 10.1002/adfm.200801081.

[12] A. S. Manikandan, K. B. Renukadevi, K. Ravichandran, P. V. Rajkumar, and K. Boubaker, “Enhanced photocatalytic, antibacterial and magnetic properties of ZnO nanopowders through lattice compatible cobalt doping,” Journal of Materials Science: Materials in Electronics, vol. 27, no. 11, pp. 11890–11901, Nov. 2016, doi: 10.1007/s10854-016-5334-3.

[13] G. E. Pike and C. H. Seager, “The dc voltage dependence of semiconductor grain-boundary resistance,” J Appl Phys, vol. 50, no. 5, pp. 3414–3422, 1979, doi: 10.1063/1.326334.

[14] Y. Sato, T. Tanaka, F. Oba, T. Yamamoto, Y. Ikuhara, and T. Sakuma, “Non-linear current-voltage characteristics related to native defects in $SrTiO_3$ and ZnO bicrystals,” Sci Technol Adv Mater, vol. 4, no. 6, pp. 605–611, Nov. 2003, doi: 10.1016/j.stam.2003.10.031.

[15] A. Sedky and E. El-Suheel, “Structural and electronic characteristics of pure and doped ZnO varistors,” Chinese Physics B, vol. 21, no. 11, Nov. 2012, doi: 10.1088/1674-1056/21/11/116103.

[16] A. Boumezoued, K. Guergouri, R. Barille, D. Rechem, M. Zaabat, and M. Rasheed, “ZnO nanopowders doped with bismuth oxide, from synthesis to electrical application,” J Alloys Compd, vol. 791, pp. 550–558, Jun. 2019, doi: 10.1016/j.jallcom.2019.03.251.

[17] L. Zhang, W. Liu, J. Gao, F. Kong, Y. Li, and S. Li, “Effects of the Er_2O_3 doping on the microstructure and electrical properties of ZnO–Bi_2O_3 based varistor ceramics,” Ceram Int, vol. 47, no. 22, pp. 32349–32356, Nov. 2021, doi: 10.1016/j.ceramint.2021.08.132.

[18] K. Hembram, T. N. Rao, M. Ramakrishana, R. S. Srinivasa, and A. R. Kulkarni, “Influence of CaO doping on phase, microstructure, electrical and dielectric properties of ZnO varistors,” J Alloys Compd, vol. 817, Mar. 2020, doi: 10.1016/j.jallcom.2019.152700.

[19] H. Zhao, J. Hu, S. Chen, Q. Xie, and J. He, “Improving age stability and energy absorption capabilities of ZnO varistors ceramics,” Ceram Int, vol. 42, no. 15, pp. 17880–17883, Nov. 2016, doi: 10.1016/j.ceramint.2016.08.057.

[20] H. Zhao, J. Hu, S. Chen, Q. Xie, and J. He, “Tailoring the high-impulse current discharge capability of ZnO varistor ceramics by doping with Ga_2O_3,” Ceram Int, vol. 42, no. 4, pp. 5582–5586, Mar. 2016, doi: 10.1016/j.ceramint.2015.12.049.

[21] A. Aljaafari and A. Sedky, “Influence of fine crystal percentage on the electrical properties of ZnO ceramic-based varistors,” Crystals (Basel), vol. 10, no. 8, pp. 1–12, Aug. 2020, doi: 10.3390/cryst10080681.

[22] S. Wan, W. Lu, and X. Wang, “Low-temperature sintering and electrical properties of ZnO-Bi_2O_3- TiO_2-Co_2O_3-MnCO 3-based varistor with Bi_2O_3-B_2O_3 frit for multilayer chip varistor applications,” Journal of the American Ceramic Society, vol. 93, no. 10, pp. 3319–3323, Oct. 2010, doi: 10.1111/j.1551-2916.2010.03866.x.

[23] W. Liu, L. Zhang, F. Kong, K. Wu, S. Li, and J. Li, “Enhanced voltage gradient and energy absorption capability in ZnO varistor ceramics by using nano-sized ZnO powders,” J Alloys Compd, vol. 828, Jul. 2020, doi: 10.1016/j.jallcom.2020.154252.

General Conclusion

General Conclusion

This research focuses on $A^{II}B^{VI}$ wide bandgap binary semiconductor materials, specifically zinc oxide (ZnO). The main objective was to investigate the effect of co-doping with different elements on the properties of ZnO nanopowder prepared by the sol-gel method. This included studying co-doped ZnO nanopowder's structural, morphological, optical, antibacterial, and electrical properties.

To achieve this, we prepared a panoply of samples using the sol-gel chemical method, an inexpensive and easy-to-implement method, and this is based on several parameters: the chemical nature of the precursors and their concentrations, the gelation time and temperature, and the doping rate with Bismuth, Gallium are chosen as the dopant in this study.

- Thermal analysis of pure ZnO powder revealed numerous exothermic and endothermic transitions. The overall formation temperature of ZnO was determined to be 546°C. The activation energy (Ea) was calculated using the Boswell, Kissinger, and Ozawa methods at three different heating rates, and the values were found to be relatively constant within the studied range.
- The X-ray diffraction analysis revealed the impact of varying concentrations of bismuth doping on the microstructure of zinc oxide. It confirmed that the powders exhibit a wurtzite structure with the appearance of a new phase at high doping concentrations, which is attributed α-Bi_2O_3 monoclinic. The lattice parameters are increased with the increase of Bi concentration, while the crystallite size decreases at the resing of Bi concentration. The SEM images of undoped and Bi doped ZnO nanopowders showed a clear grain size reduction at the resing of Bi concentration. The EDS spectra revealed the presence of Zn, O, and Bi elements for doped samples. UV-Vis results revealed a slight increase in the absorption edge, indicating a decrease in bandgap energy with increasing bismuth doping concentration. The FTIR spectra confirmed the presence of Zn-O and Bi-O-Bi bands.
- Doping ZnO nanoparticles with Gallium (Ga) significantly impacts their structural properties. XRD analysis confirms the presence of the hexagonal

wurtzite structure in all samples. However, Ga doping leads to an increase in lattice parameters while decreasing the crystallite size. Scanning electron microscopy (SEM) images reveal a clear reduction in grain size with increasing Ga concentration. Energy-dispersive X-ray spectroscopy EDS confirms the presence of Zn, O, and Ga elements in doped samples. Interestingly, UV-Vis spectroscopy shows a decreased absorption edge with increasing Ga concentration, indicating increased bandgap energy. Finally, Fourier-transform infrared spectroscopy (FTIR) confirms the presence of the Zn-O bond in all samples.

- Co-doping ZnO nanoparticles with Bismuth (Bi) and Gallium (Ga) significantly affects their structural properties**.** (XRD) analysis confirms the presence of the hexagonal wurtzite structure in all samples. However, for samples with high Bi concentration, an additional α- Bi_2O_3 phase was also detected compared to pure ZnO, co-doping with Bi and Ga leads to an increase in lattice parameters and a decrease in crystallite size.Scanning electron microscopy (SEM) images reveal a clear reduction in grain size with increasing Biconcentration in the co-doped samples. Energy-dispersive X-ray spectroscopy (EDS) confirms the presence of Zn, O, Bi, and Ga elements in the co- doped samples.UV-Vis spectroscopy shows a slight increase in the absorption edge with varying co-doping concentrations compared to the pure sample, indicating a decrease in bandgap energy.Fourier-transform infrared spectroscopy (FTIR) confirms the presence of the Zn-O bond in all samples. Additionally, samples with high Bi concentration exhibit an O-Bi-O bond, further supporting the presence of the α-Bi_2O_3 phase detected by XRD.
- The evaluation of the antibacterial effect of nanoparticles synthesized by the sol-gel technique for both pure and bismuth- and gallium-doped zinc oxide powders demonstrated an antibacterial effect against both Gram-positive (Listeria monocytogenes) and Gram-negative (Escherichia coli, Klebsiella pneumoniae, Enterobacter aerogenes) bacterial strains. Bismuth-doped and (Bi, Ga) co-doped zinc oxide exhibited superior antibacterial activity against Escherichia coli compared to gallium-doped zinc oxide, which showed greater efficacy against Gram-positive Listeria bacteria.
- The I-V characteristics of the pure doped and co-doped ZnO nanopowders with Bi and Ga indicate a decrease in the breakdown voltage and an increase in the

leakage current and the non-linear coefficient with Ga doping. While the breakdown voltage threshold increases with increasing bismuth doping concentration.

Future Directions:

This research could be extended in several directions.

- Evaluate the photocatalytic activity of Bismuth—and Gallium-doped ZnO nanoparticles and investigate their ability to degrade organic pollutants under light irradiation.
- Evaluate the potential applications of these nanoparticles in biomedical fields, such as drug delivery and tissue engineering.
- Develop methods for integrating Bi- and Ga-doped ZnO nanoparticles into existing varistor fabrication processes.
- Investigate the potential applications of these nanoparticles in solar cells, light-emitting diodes, and other optoelectronic devices.

ANNEXES

ANNEX

Name and formula

Reference code: 1451-036-00

Mineral name: Zincite, syn
Compound name: Zinc Oxide
Common name: zinc white
PDF index name: Zinc Oxide

Empirical formula: OZn
Chemical formula: ZnO

Crystallographic parameters

Crystal system: Hexagonal
Space group: P63mc
Space group number: 186

a:)?(3,2498
b (?): 3,2498
c (?): 5,2066
Alpha (°): 90,0000
Beta (°): 90,0000
Gamma (°): 120,0000

Volume of cell (10^6 pm^3): 47,62
Z: 2,00

RIR: -

Subfiles and quality

Subfiles: Alloy, metal or intermetalic
Common Phase
Corrosion
Educational pattern
Forensic
Inorganic
Mineral
NBS pattern
Pharmaceutical
Pigment/Dye
Quality: Star (S)

Comments

Color:	Colorless
Creation Date:	1970/01/01
Modification Date:	1970/01/01
Sample Source or Locality:	The sample was obtained from the New Jersey Zinc Co., Bethlehem, Pennsylvania, USA
Powder Data:	References to other early patterns may be found in reference)5(
Optical Data:	B=2.013, Q=2.029, Sign +=
Color:	Colorless. The structure was determined by Bragg (1) and refined by Abrahams, Bernstein (2). A high pressure cubic NaCl-type of ZnO is reported by Bates et al. (3) and a cubic, sphalerite type is reported by Radczewski, Schicht)4(
Temperature of Data Collection:	The approximate temperature of data collection was 26 C
Additional Patterns:	To replace 00-005-0664)5(
Additional Patterns:	See ICSD 31052 (PDF 01-075-1526) .

References

Primary reference:	McMurdie, H., Morris, M., Evans, E., Paretzkin, B., Wong-Ng, W., Ettlinger, L., Hubbard, C ,.Powder Diffraction)1986(,76 ,**1** ,
Structure:	.2Abrahams, S., Bernstein, J ,.Acta Crystallogr., Sec. B ,1233 ,**25** ,)1969(
Optical data:	Dana's System of Mineralogy, 7th Ed ,.**I**504 ,
Other:	.5Swanson, H ,.Fuyat, R ,.Natl. Bur. Stand. (U.S.), Circ. 539 ,25 ,**2** ,)1953(

Peak list

No.	h	k	l	d [A]	2Theta[deg]	I]%[
57,0	31,770	2,81430	0	0	1	1
44,0	34,422	2,60332	2	0	0	2
100,0	36,253	2,47592	1	0	1	3
23,0	47,539	1,91114	2	0	1	4
32,0	56,603	1,62472	0	1	1	5
29,0	62,864	1,47712	3	0	1	6
4,0	66,380	1,40715	0	0	2	7
23,0	67,963	1,37818	2	1	1	8
11,0	69,100	1,35825	1	0	2	9
2,0	72,562	1,30174	4	0	0	10
4,0	76,955	1,23801	2	0	2	11
1,0	81,370	1,18162	4	0	1	12
7,0	89,607	1,09312	3	0	2	13
3,0	92,784	1,06384	0	1	2	14
6,0	95,304	1,04226	1	1	2	15
4,0	98,613	1,01595	4	1	1	16
2,0	102,946	0,98464	2	1	2	17
5,0	104,134	0,97663	5	0	1	18
1,0	107,430	0,95561	4	0	2	19
3,0	110,392	0,93812	0	0	3	20
8,0	116,279	0,90694	3	1	2	21
4,0	121,572	0,88256	2	0	3	22

1,0	125,188	0,86768	6	0	0	23
3,0	133,932	0,83703	5	0	2	24
1,0	136,521	0,82928	6	0	1	25
2,0	138,513	0,82370	4	1	2	26
3,0	142,918	0,81247	0	2	2	27

Stick Pattern

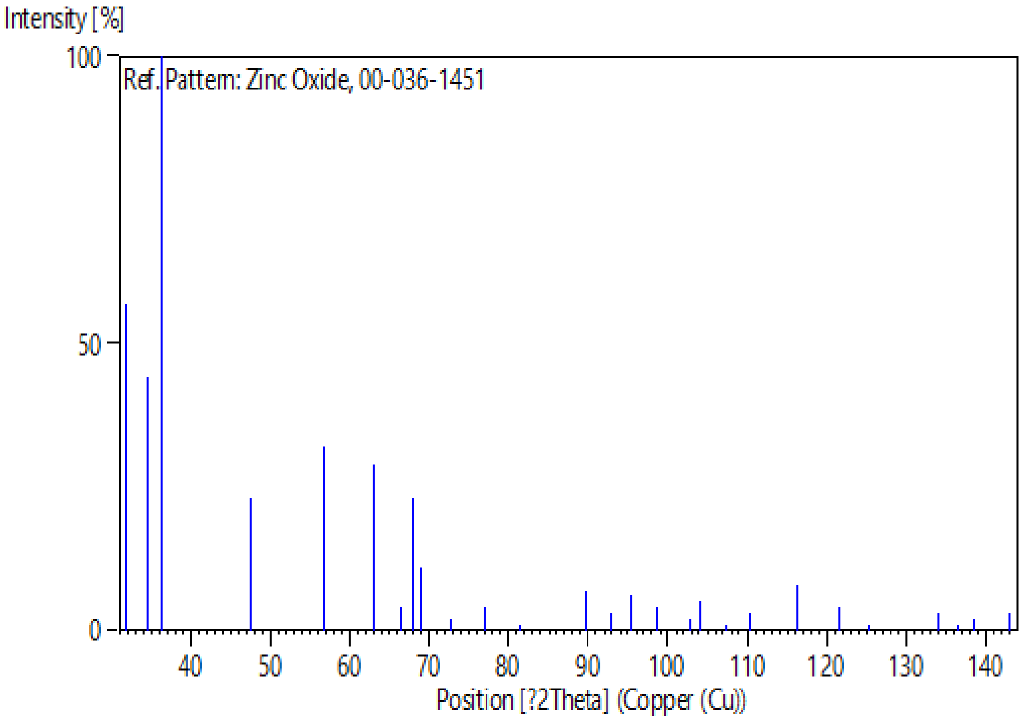

Name and formula

Reference code:	01-076-1730
Compound name:	Bismuth Oxide
Common name:	Bismuth oxide - alpha
ICSD name:	Bismuth Oxide
Empirical formula:	Bi_2O_3
Chemical formula:	Bi_2O_3

Crystallographic parameters

Crystal system:	Monoclinic
Space group:	P21/c
Space group number:	14
a (Å):	5,8300
b (Å):	8,1400
c (Å):	7,4800
Alpha (°):	90,0000
Beta (°):	67,0700
Gamma (°):	90,0000
Calculated density (g/cm^3):	9,47
Volume of cell (10^6 pm^3):	326,92
Z:	4,00
RIR:	7,59

Subfiles and quality

Subfiles:	Alloy, metal or intermetalic ICSD Pattern Inorganic
Quality:	Calculated (C)

Comments

ICSD collection code:	036160
Creation Date:	01/01/1970
Modification Date:	01/01/1970

ICSD Collection Code:	036160
Test from ICSD:	No R value given
Test from ICSD:	At least one TF missing. On the crystal structure of monoclinic Bi2 O3-alpha. e5 (P121/C1). A2X3.

References

Primary reference:	Calculated from ICSD using POWD-12++, (1997)
Structure:	Sillen, L.G., Z. Kristallogr., Kristallgeom., Kristallphys., Kristallchem., **103**, 274, (1941)

Peak list

No.	h	k	l	d [A]	2Theta[deg]	I [%]
1	1	0	0	5,36932	16,497	0,2
2	0	1	1	5,25853	16,847	1,1
3	1	1	0	4,48207	19,792	0,9
4	0	2	0	4,07000	21,820	1,0
5	1	0	2	3,60749	24,658	6,6
6	0	0	2	3,44447	25,845	17,5
7	-1	1	1	3,29811	27,013	26,6
8	1	2	0	3,24349	27,477	100,0
9	0	1	2	3,17216	28,107	22,2
10	2	1	1	2,74434	32,602	6,6
11	-1	2	1	2,69982	33,155	31,1
12	2	0	0	2,68466	33,348	43,8
13	0	2	2	2,62926	34,072	5,8
14	2	1	0	2,54940	35,174	10,1
15	0	3	1	2,52457	35,531	7,5
16	-1	0	2	2,49141	36,020	3,7
17	1	3	0	2,42165	37,095	4,1
18	-1	1	2	2,38233	37,730	9,8
19	2	2	0	2,24091	40,210	4,0
20	0	1	3	2,21006	40,796	0,5
21	-1	3	1	2,16852	41,614	2,6
22	-2	1	1	2,14627	42,066	1,0
23	-1	2	2	2,12490	42,509	5,2
24	0	4	0	2,03500	44,485	1,0
25	0	2	3	1,99995	45,307	3,6
26	2	3	1	1,98609	45,641	0,2
27	2	2	3	1,95163	46,494	18,7
28	3	0	2	1,92426	47,195	0,4
29	2	3	0	1,90832	47,614	1,4
30	1	4	0	1,90291	47,757	1,3
31	3	1	1	1,87264	48,579	4,9
32	1	0	4	1,86480	48,796	9,8
33	-1	3	2	1,83506	49,640	4,3
34	-1	1	3	1,81782	50,143	4,2
35	-2	0	2	1,80394	50,556	0,6
36	3	0	0	1,78977	50,985	0,1
37	-1	4	1	1,77244	51,520	1,0
38	-2	1	2	1,76121	51,872	5,8

39	0	3	3	1,75284	52,139	5,3
40	3	1	0	1,74802	52,293	3,2
41	3	2	1	1,73967	52,563	7,4
42	-2	3	1	1,72061	53,191	8,1
43	-1	2	3	1,69532	54,049	0,2
44	0	1	4	1,68494	54,409	0,4
45	2	4	1	1,66861	54,986	9,1
46	-2	2	2	1,64906	55,694	7,8
47	3	2	0	1,63836	56,090	5,4
48	2	4	0	1,62170	56,718	1,2
49	3	0	4	1,58804	58,033	5,4
50	0	2	4	1,58608	58,112	5,9
51	-1	4	2	1,57601	58,519	4,7
52	3	3	1	1,56964	58,780	1,4
53	-3	1	1	1,55881	59,229	4,1
54	-1	3	3	1,53683	60,162	0,5
55	0	4	3	1,52301	60,766	0,1
56	-2	4	1	1,50172	61,720	3,8
57	3	3	0	1,49394	62,077	3,5
58	-1	5	1	1,48392	62,544	1,8
59	-1	0	4	1,48072	62,694	3,7
60	4	0	2	1,45750	63,809	1,8
61	0	3	4	1,45406	63,978	1,3
62	4	1	2	1,43468	64,948	0,6
63	2	5	1	1,42135	65,633	0,3
64	4	1	1	1,40458	66,517	2,4
65	3	4	1	1,39817	66,862	0,6
66	2	2	5	1,39314	67,136	3,3
67	-3	0	2	1,38295	67,697	0,4
68	-1	4	3	1,37490	68,147	2,6
69	-3	3	1	1,37066	68,387	1,5
70	-1	5	2	1,36284	68,835	2,3
71	0	1	5	1,35847	69,087	1,5
72	-2	4	2	1,34983	69,593	0,4
73	4	2	1	1,34571	69,837	0,9
74	3	4	0	1,34388	69,946	1,9
75	4	0	0	1,34233	70,039	1,8
76	0	6	1	1,33110	70,718	0,3
77	0	5	3	1,32809	70,902	0,7
78	4	1	0	1,32444	71,127	1,2
79	1	6	1	1,31532	71,696	3,8
80	0	2	5	1,30504	72,350	1,3
81	-2	3	3	1,30121	72,596	2,0
82	-1	3	4	1,29972	72,693	1,3
83	4	3	2	1,28398	73,730	0,7
84	4	2	0	1,27470	74,357	2,0
85	-1	6	1	1,26986	74,688	2,2
86	4	3	1	1,26222	75,219	0,5
87	-3	4	1	1,25195	75,945	0,2
88	-2	0	4	1,24571	76,393	0,1
89	3	5	1	1,24288	76,599	0,1
90	-3	3	2	1,23214	77,390	1,1
91	2	6	1	1,22998	77,551	0,6
92	-1	5	3	1,22643	77,818	0,9
93	1	0	6	1,22456	77,959	0,9
94	-4	1	1	1,21679	78,552	0,2

95	1	1	6	1,21094	79,006	1,4
96	-2	5	2	1,20860	79,189	0,8
97	3	5	0	1,20427	79,530	1,2
98	4	3	4	1,20250	79,670	1,5
99	-1	4	4	1,19727	80,089	2,7
100	-2	2	4	1,19107	80,591	2,3
101	-3	1	3	1,18971	80,702	1,7
102	0	5	4	1,18308	81,249	0,2
103	-4	2	1	1,17784	81,687	1,1
104	-1	2	5	1,17264	82,127	0,2
105	4	4	1	1,16780	82,541	2,7
106	-2	6	1	1,15833	83,366	1,2
107	-3	2	3	1,15333	83,809	0,3
108	5	1	2	1,15020	84,089	0,7
109	0	7	1	1,14664	84,411	0,4
110	-3	4	2	1,14374	84,674	2,4
111	0	4	5	1,14089	84,935	1,3
112	-3	5	1	1,13684	85,310	1,1
113	-2	3	4	1,13210	85,752	0,5
114	5	0	4	1,13012	85,939	0,7
115	-4	3	1	1,12073	86,837	1,5
116	5	1	1	1,11938	86,967	1,2
117	5	2	2	1,11723	87,177	1,3

Stick Pattern

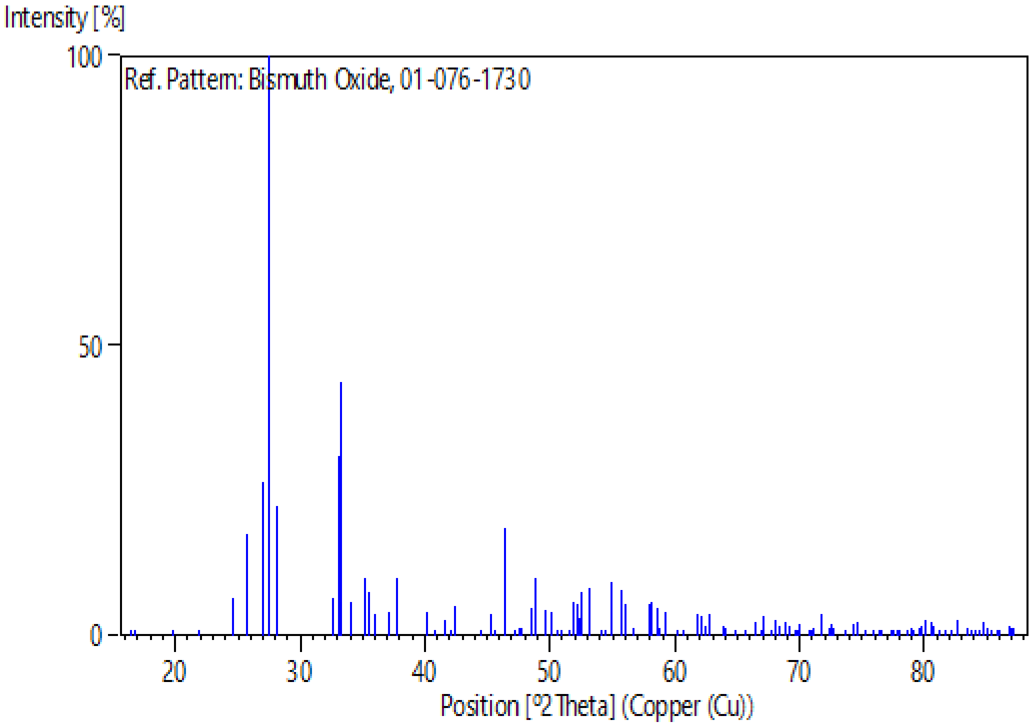

List Of Scientific publications

- LATIF. AYA, Arab. Louiza, Amri. Abdelhak, Arab. Louiza., Sengouga. Noureddine, & Tibermacine. Toufk. Effect of Ga doping on the structural, optical, and electrical properties of ZnO nanopowders elaborated by sol-gel method. *Materials Research Bulletin*, 112886. 2024
  doi: 10.1016/j.materresbull.2024.112886.
- Amri. Abdelhak, Arab. Louiza, Meftah. Afak, LATIF. AYA, "Effect of aluminum doping on the structural, optical and electrical properties of ZnO thin films processed under thermal shock conditions." *Results in Optics*, *11*, 100426. 2023. doi:10.1016/j.rio.2023.100426
- Keziz. Ahcen, Rasheed. Mohammed, Heraiz. Meand, Sahnoune. Foudil, & LATIF. AYA "Structural, morphological, dielectric properties, impedance spectroscopy and electrical modulus of sintered Al6Si2O13–Mg2Al4Si5O18 composite for electronic applications." *Ceramics International*, *49*(23), 37423-37434. (2023). doi : 10.1016/j.ceramint.2023.09.068
- Arab. Louiza, Amri. Abdelhak, Meftah. Afak, LATIF. AYA, Tibermacine. Toufik, & Sengouga, Noureddine. "Effect of the annealing process on the properties of ZnO thin films prepared by the sol-gel method." *Chemical Physics Impact*, *7*, 100266. (2023). doi : 0.1016/j.chphi.2023.100266